UNIVERSITÀ
DEGLI STUDI
DI PADOVA

Head Office: Università degli Studi di Padova

Department: Geoscienze

Ph.D. COURSE IN: Geosciences

SERIES: XXXV

CONSTRAINING EARTHQUAKE SOURCES BY SEISMIC TIME REVERSAL

Coordinator: Prof. Claudia Agnini

Supervisor: Prof. Lapo Boschi

Co-Supervisor: Dr. Irene Molinari, Dr. Simone Cesca

Ph.D. student: Apsara Sharma Dhakal

ACKNOWLEDGEMENT

I would like to take this opportunity to express my sincere gratitude to the following people and organizations, who have supported and assisted me throughout my doctoral journey:

First and foremost, I am deeply grateful to my supervisor Prof. Lapo Boschi, who provided me with invaluable mentorship, encouragement, and feedback throughout my research process. I am also grateful to my co-supervisors, Dr. Irene Molinari, who expertly guided me through the time reversal method and Dr. Simone Cesca, providing me the opportunity to spend one month abroad in GFZ, Germany and for his suggestions to improve my work. Their valuable remarks and helpful feedback have played a significant role in molding my research and writing.

I would also like to thank Prof. Abdlekrim Aoudia, who have been my constant source of support, inspiration, and encouragement. I am also deeply grateful to my husband Hari Ram Thapa, whose unwavering love, support, and understanding have sustained me through the high and lows of my doctoral journey. His patience and encouragement have been valuable in helping me balance my academic and personal life.

I would like to acknowledge the contribution of my family members, father, mother and brother who have always believed in me and supported me throughout my academic journey. Their love, care, and encouragement have been a source of strength and inspiration.

Lastly, I would like to extend my sincere appreciation to the faculty and staff of Department of Geoscience, University of Padova, who created a vibrant and intellectually stimulating environment that fostered my personal and academic growth.

Thank you all for your invaluable contributions and unwavering support. Without your help, this thesis would not have been possible.

CONTENTS

List of Figures

ABSTRACT

Earthquake rupture is a complex phenomenon of which we understand comparatively little. In mapping the rupture of a seismic event in both space and time, different techniques and datasets have been used, which often led to incoherent results for the same event. Most of these methods rely on seismic recordings neglecting the information carried by the surface waves, and focus on the arrivals of P- and S-waves. The central idea of our project is to implement surface-wave time reversal, to study the focusing of the time-reversed field at the source location and to better constrain the details of rupture processes at the source of seismic events. Our method combines the seismic time reversal approach with a ray-tracing algorithm, relying on the generalized harmonic parameterization to trace surface-wave ray paths in the presence of laterally varying azimuthal anisotropy.

We validated our time-reversal method, and quantified its limitations, through a number of synthetic tests at the global scale. In our experiments, a prominent maximum of the time-reversed wave filed is systematically obtained at or very close to the original location and time of the source. The uncertainties in the original source location and time are governed by the distribution of stations, and velocity model used. We next applied our method to narrow-frequency-band-filtered surface-wave data from the great 26 December 2004 Sumatra-Andaman earthquake. We reproduce the results of earlier studies, including the reconstruction of the source location, direction of rupture propagation, its spatial extent, its duration, and identify the region where most seismic energy is released.

Further, we applied our method to a volcanic setting, i.e., to recordings of very long period events that occurred in Mayotte, Comoro Islands. Our results are found to be in good agreement with the centroid locations obtained by moment tensor inversion. A precise location of this type of events helps in constraining the depth, size, and the geometry of the seismogenic volume, and hence to shed light on deep processes associated with volcanism. Moreover, we applied our methodology to one of the recent earthquake, February 6, 2023, M_w 7.8 Turkey earthquake and analyse its rupture propagation and compared our results with the most recently published results.

Keywords: *Earthquake source*, *Surface wave*, *Time reversal*, *Ray tracing*, *Sumatra Earthquake*, *Mayotte Island*.

CHAPTER 1

Introduction and state of the art

With rare exceptions, fault planes are not accessible to direct observation, and their properties can only be reconstructed by the analysis of seismic and geodetic data. To better understand earthquake dynamics, the earthquake cycle, and eventually for seismic hazard assessment, it is crucial to understand where the earthquake rupture of large earthquakes nucleates and how it propagates. Most often, arrivals of P- and S- wave are used to image the rupture history of an earthquake in terms of slip map, source time function and local slip-rate. In the past decades, many works have been conducted to formulate and solve the inverse problems either by linear inversion (Olson and Apsel, 1982) or nonlinear inversion (Hartzell et al., 1996; Monelli and Mai, 2008), and so to constrain the space-time distribution of the slip along a fault plane, based on availability of seismic data. One of the main outcomes of those efforts is that the distribution of the slip associated with a large earthquake tends to be very heterogeneous.

Many authors used different inversion schemes which led to discrepancies among the slip models for an earthquake (Beresnev, 2003; Mai et al., 2016). These discrepancies may be ascribed to different data selection and processing, to the methods used in the computation of Green's functions, and/or to the parameterization used for inversion itself. Due to our imperfect knowledge of the Earth's structure and of fault geometry, and to the fact that data coverage is systematically insufficient, the solution of the source inversion problem is very non-unique. In other words, different source-imaging methods, applied to the same data, result in different models of the source, and eventually lead to different ideas of an earthquake's nature. Therefore, we adopted the surface wave time-reversal technique to mitigate this uncertainty, at least in the case of large earthquakes, by taking a section of seismograms that are not generally included in source inversion problem: the surface waves.

The main aim of this project is to provide a method for interpreting regional and teleseismic seismograms in terms of properties of the seismic rupture, or, in other words, to map seismic slip as a function of position on the fault, and time, for a given earthquake. We first investigate the influence of station distribution, and/or errors in the velocity model, on the focusing of the time-reversed wave field using synthetic data, and then apply the same method to real data. Our method is in particularly effective when applied to regional and teleseismic data of large earthquakes; we have also applied it successfully on seismic recordings of very long period events in a volcanic region. In particular, observation of these kinds of events could improve our understanding of volcanic activity (Carbone et al., 2006, 2008).

1.1 Seismic fault imaging

Based on the magnitude and depth of the earthquake, and on the station coverage, different approaches are implemented to estimate the spatial and temporal behavior of seismic slip for a given earthquake. Several different types of data are used. For instance, dense networks of strong-motion accelerometers, GPS networks and satellite geodesy are used to constrain the seismic slip associated with an earthquake: they provide a good resolution of the surface expression of the event, but have relatively limited sensitivity to the fault geometry. Regional and/or global seismic networks at teleseismic distance are used in case near-field instrumental coverage is insufficient. Thus, seismic data along with geodetic data and field geology observation (if needed) could be used to constrain the fault geometry.

Based on availability of seismic datasets, one could map slip on the fault via (a) least-squares inversions, (b) the back-projection method, or (c) the seismic time-reversal method.

1.1.1 Least-squares inversion

This method is based on the representation theorem, which provides a linear relationship between the observed displacement and the slip rate distribution on the fault plane. However, real-world least-squares imaging poses more challenges due to the elastic effect in the wave propagation and due to the complexity in spatiotemporal evolution of seismic ruptures, their solutions tends to be non-unique (Mai et al., 2016). Moreover, it can be very expensive in terms of computational cost. The time reversal method whereas can effectively handle complex wave propagation phenomena, such as multiple reflections and scattering, which can pose challenges for least square inversion. The time reversal method is able to capture and utilize the full complexity of wave propagation, resulting in more accurate imaging and source location.

1.1.2 Back-projection method

This method is robust and requires a limited number of assumptions with no inversion involved. It consists of reconstructing oscillations backward in time by transforming available receivers into sources of spherical waves (Ishii et al., 2005). The recordings from an array of nearby stations are stacked, and the location where the stack has maximum value are interpreted as sources of the originally recorded wave field. However, the physical nature of such back-projected wave field that focuses on source remains undefined, i.e., it is not clear how the back-projected field is related quantitatively to slip and/or slip rate (Fukahata et al., 2014).

1.1.3 Time reversal (TR) method

This method was largely developed and "popularized" by Mahtias Fink and co-workers, in the framework of theoretical and experimental acoustics. TR first emerged in underwater acoustics (Parvulescu and Clay, 1965; Edelmann et al., 2002), and from there it spread to various other fields such as medical imaging (Fink, 1997; Fink and Tanter, 2010) and non-destructive testing (Chakroun et al., 1995; Sutin et al., 2004). TR source imaging was first introduced by (McMechan, 1982), where the time-reversed wave equation was used to image earthquake sources instead of subsurface structures. This is in some ways similar to the back-projection method; however, it requires the back propagated wave field to be modeled numerically, solving the 3-D displacement equation instead stacking the signal; receivers act as dipole rather than monopole sources and the time-reversed wave field can be interpreted as displacement (or velocity), within the method's resolution limits. TR is the most reliable available technique, from the theoretical viewpoint, to reconstruct the seismic source; on the other hand, early applications to seismic data have suggested it to be computationally too heavy for systematic practical application.

The advantage of our method is that it does not requires any prior assumptions generally used in alternative location techniques or source mechanism inversion to obtain the source location, extent and duration simultaneously (Lokmer et al., 2007). Further, time reversal method being based on wave equations instead of travel time, it starts from wave equations, decomposes the wave field and prevents the traditional use of the travel time. The success of our method, however, depends on the distribution of the station over the globe, large dimension of the earthquake and on the quality of the velocity model used for backward wave propagation. Its application to the smaller event is also discussed in chapter 3.

In this thesis, the TR concept is applied to the surface-wave portion of the seismogram, neglecting body waves. The advantages of using surface waves over body waves are explained below in section 1.2. This significantly reduces the computational costs of full-waveform time-reversal. To model the propagation of surface waves, the 2-D Helmholtz equation is used, in a laterally smooth, lossless half space. The theory behind surface wave time-reversal is summarized in section 2.2.2. The method involves recording the surface waves generated by an earthquake and using mathematical algorithms to reverse the propagation of the waves back in time. This technique is based on the principle of spatial reciprocity and time invariance.

The basic steps of the surface-wave time reversal method consist of taking the recordings of seismic events, identifying the time window during which the surface waves were generated and reverse the propagation of the waves back in time, mathematically flipping the waveforms so that they travel back to the source of the earthquake. Then, we determine the location and characteristics of the seismic source by analyzing the reversed waveforms.

Surface waves carry a lot of information, that, in previous efforts to reconstruct seismic sources, has often been neglected. Our contribution helps to fill this methodological gap, and will ultimately help us to better understand the nature of earthquakes. In the long run, it is our hope that efforts such as our could lead to improve earthquake forecasting and hazard mitigation strategies.

1.2 Surface waves

Surface waves are seismic waves that travel along the surface of the earth and are studied widely for the characterization of the Earth's interior such as determination of regional crust, upper mantle and transition zone, determination of the elastic/anelastic properties of shallow subsurface and survey of loose sediments. They are classified into two types: (a) Rayleigh waves and (b) Love waves. The former consists of an elliptical retrograde motion along a plane parallel to the direction of propagation and perpendicular to the surface of the earth; the latter consist of a horizontal motion that is transversal to the direction of propagation, and therefore parallel to the surface of the earth (Fig. 1.1).

In the framework of our research, surface waves carry several advantages in comparison to body waves. Surface waves are efficiently generated by shallow sources. This also applies, e.g., at regional distances, where surface waves have much larger amplitudes for shallow earthquakes, than for deeper ones. Moreover, they are dispersive, i.e., different frequencies travel with different velocities and sample the Earth at different depths (the longer the period, the larger the depth of sensitivity).

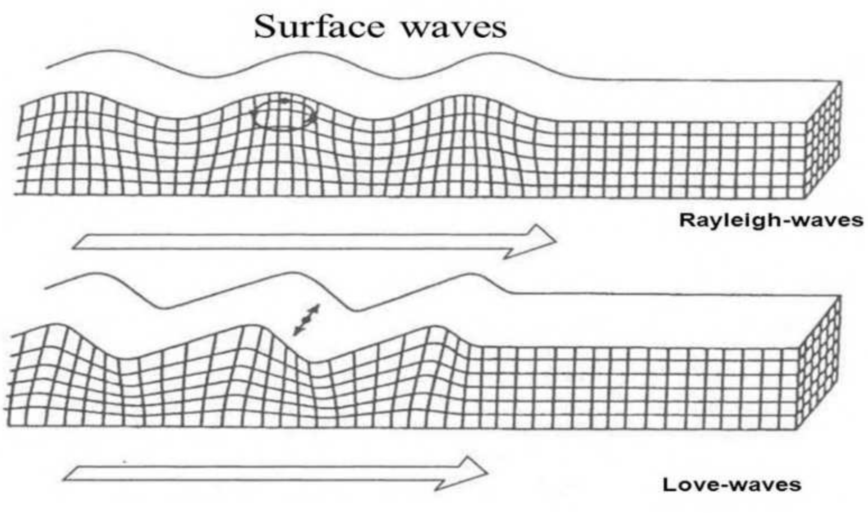

Fig. 1.1 Particle motion associated with the propagation of seismic waves, from Inder Singh Gupta, 2014.

In our method, we time-reverse the entire surface-wave window of seismograms, neglecting the body-wave one. The information carried by these waves are important for following reasons:
(a) Due to its dispersive nature, the time-reversed back-propagated surface-wave field focuses sharply on the source location, which can enhance the robustness and resolution of mapped seismic slip.

(b) Propagation of the surface wave can be studied separately for each a set of narrow-frequency bands, thus reducing the modeling problem from 3-D to 2-D (e.g., Ekström et al., 1997). This lowers the computational costs drastically.

(c) Knowledge of the 3-D structure of the Earth's interior, necessary to back propagate the time-reversed signal, is limited; but surface waves propagate within the crust and shallow mantle, whose structure is relatively well understood i.e., global phase velocity maps of Rayleigh wave velocities are available in the frequency band relevant to our study, at both regional and global scale, thus improving the accuracy of the time-reversal method.

Considering these advantages, our method contributes significantly to efforts towards reconstructing the location of earthquakes and mapping the related ruptures in both space and time. We anticipate that our method works well for a wide range of epicentral distances. Unlike body waves, surface waves carry more energy at an epicentral distance greater than 30° and can be easily identified and isolated in seismograms. Even at shorter distance, though obscured by the body-wave coda, surface waves can still emerge in a time-reversal experiment (Boschi et al., 2018).

1.3 Surface Wave Ray tracing

We use an existing surface-wave ray tracing algorithm, based on a generalized spherical-harmonic parameterization of surface wave phase velocity (Boschi and Woodhouse, 2006), to model surface-wave propagation by ray tracing. The algorithm accounts for laterally varying azimuthal anisotropy of surface-wave velocity. The generalized spherical harmonic parameterization is theoretically complex; it is, however, more effective than, e.g., a pixel or spline parameterization, when tracing rays through an azimuthally anisotropic phase velocity map (Boschi and Woodhouse, 2006). The expansion of azimuthal anisotropy is done by using generalized spherical harmonics, which allows path-averaged phase velocities to be calculated with great ease. This parameterization makes the inverse problem invariant with respect to rotations of the co-ordinate frame and eliminates singularities associated with the indeterminacy of azimuths at the poles.

The basic idea behind this algorithm is to trace a ray from the source towards all points in the grid, to calculate at what time the narrow-band surface-wave wavelet will reach a certain point in the grid. Based on that and actual recordings, we built a time-reversed wave field. Thus, the total time-reversed wave field is the sum of all time-reversed wave-fields obtained from all the individual stations. Boschi and Woodhouse (2006) introduce several innovative ideas to improve the accuracy and efficiency of the ray tracing method. The details of the ray tracing algorithm are given in Chapter 2, Section 2.2.1, where we also describe some improvement that were introduced in the framework of this thesis. Here, Fig. 1.2 shows the ray path traced using this algorithm for arbitrarily chosen source and receiver.

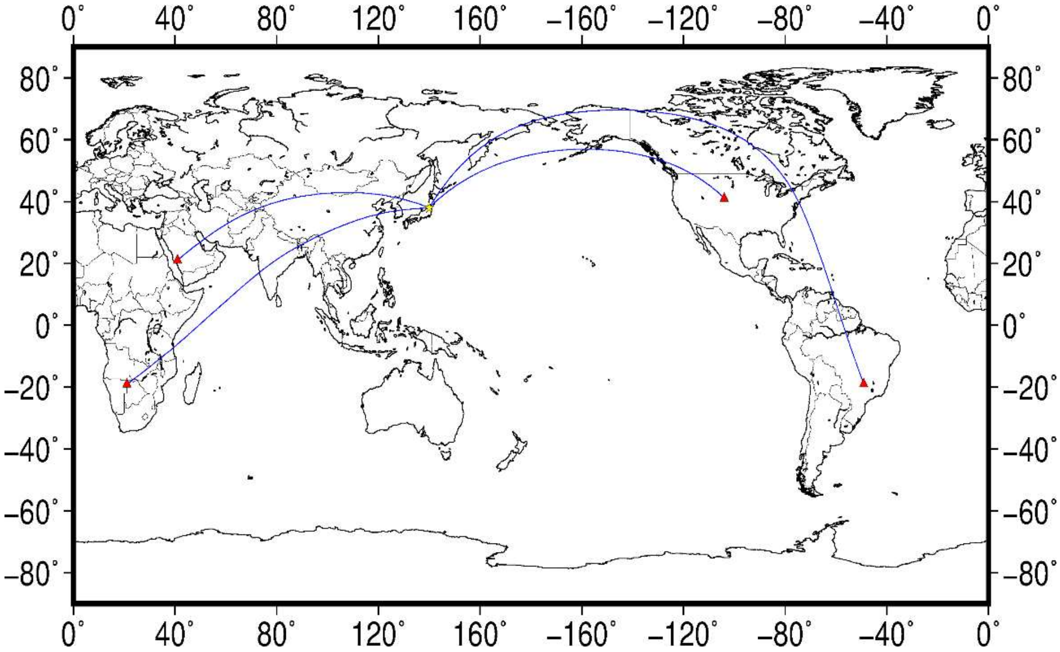

Fig. 1.2 100 s Rayleigh wave ray paths traced using surface wave ray tracing algorithm for an arbitrarily chosen source-receiver geometry.

1.4 Study Area

1.4.1 Sumatra-Andaman Island

The subduction zone offshore Sumatra received relatively little attention in comparison with the subduction zones in Japan and United States prior to the 2004 earthquake and tsunami (McCaffrey, 2009). The subduction zone, which is also known as Sunda subduction zone, is a long convergent belt that extends southward from the Himalayan Frontal Thrust through Myanmar. This trench further continues towards the south and passes through Andaman and Nicobar Islands and Sumatra, south of Java and the Sunda Islands (See Fig. 1.3). In a broad sense, the simple interaction of the Indo-Australian and Eurasian plates explains the plate kinematics of Sumatra region. Generally, the tectonics of Sunda subduction zone is divided into western and eastern settings. To the east of Sumba, the lighter continental Australian lithosphere is thrusting beneath the Oceanic lithosphere, while to the west of Sumba, the dense Indian Ocean Lithosphere subducts beneath the continental Sunda plate. Relative to Sunda Plate, the Australian plate is moving northward with convergence rate of ∼67 mm/year, while the Indian Ocean is

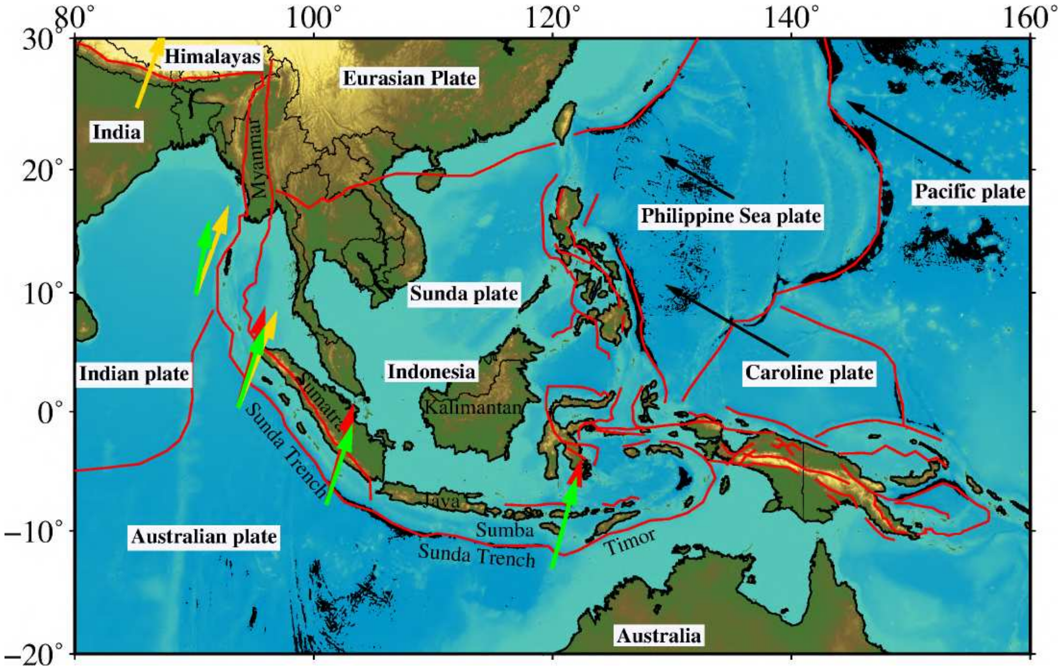

Fig. 1.3 Plate tectonic setting of Sumatra. Here, green, golden and red arrows represent direction of Australian-Sunda plate motion, Indian-Eurasian plate motion and Australian-Eurasian plate motion while thick red line is for fault.

subducting beneath Sunda plate with speed of ~52 mm/year (DeMets et al., 1994). The northward motion of Australian plate is accommodating by the Sunda subduction zone. Sunda subduction zone is also called Sunda megathrust. Generally, megathrust faults occur at locations where subducting oceanic crust thrust beneath the continental crust and islands arcs.

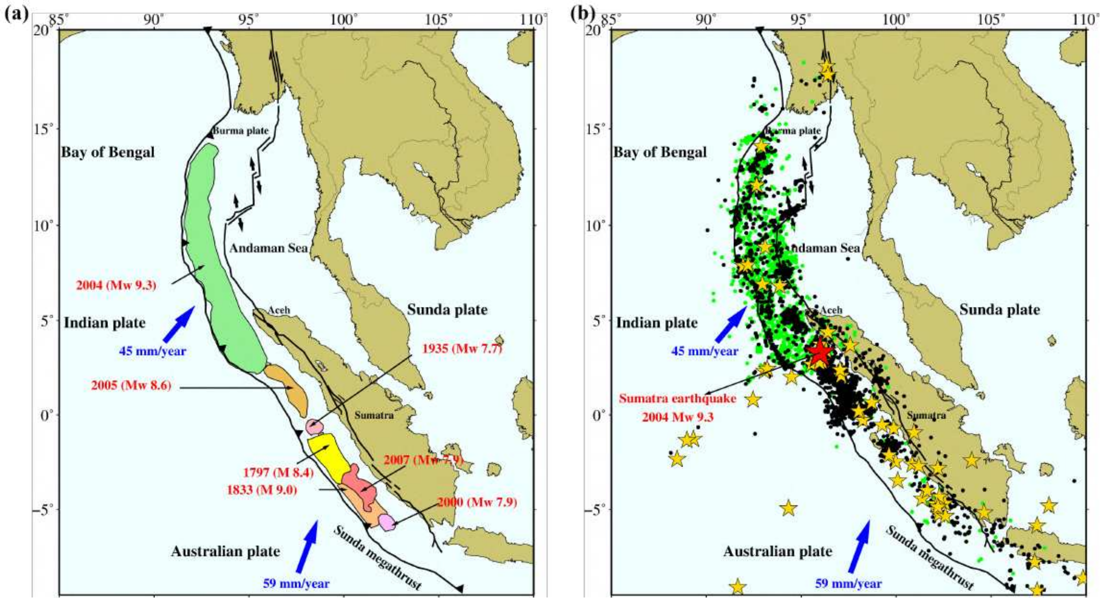

Fig. 1.4 (a) Tectonic context and earthquake history of the Sunda subduction zone. The subducting Indian and Australian plates are separated from the Sunda plate to the northeast by a forearc sliver known as the Burma microplate. Blue arrows on the figure indicate the orientation and speed of plate motions with respect to the Sunda plate. The black lines represent major fault zones that mark the boundaries of the plates in the region. The colored outlines highlight the extent of large historical and recent ruptures that occurred on the megathrust. The figure has been adapted from (Briggs et al., 2006) and incorporates data from (Bilham, 2005), (Natawidjaja et al., 2006), (Konca et al., 2008). (b) Aftershock sequence of 2004 Sumatra-Andaman earthquake, M_w 9.3 (green dots) and 2005, M_w 8.6 (black dots). Golden star shows the location of events ($M_w >$ 7.0) after 1900, along the Sunda subduction zone (from USGS catalog).

Sumatra is located at the southern edge of Sunda shelf (Bird, 2003), which is moving with speed of few millimeters per year to few centimeters per year towards east of Eurasia Plate (Chamot-Rooke and Le Pichon, 1999; Bock et al., 2003). Further, Sumatra sits at the boundary between two tectonic plates. To the south-west of Sumatra, there is ocean floor, which is part of Indian/Australian plate, while the Sumatra and other islands in Indonesia are part of the Eurasian plate. The two tectonic plates meet at the ocean floor at the plate boundary, known as sunda subduction zone, which is 5500 km long boundary between the Indo-Australian and Eurasian plates. The nature of convergence is oceanic type in the Andaman-Sunda arc (Kayal, 2008). The Andaman-Sunda arc is considered as seismically very active and categorized as highest seismic hazard zone because in Sumatran region, the oceanic plate is subducting beneath the continental plate. The two plates become locked or stuck. As the subducting plate slowly descends, it pulls the upper plate down with it, which cause the deformation in the overriding plate, resulting the stress build up.

The Andaman-Sumatra section of the subduction zone already had hosted several damaging large and great earthquakes in the past, out of which some generated also destructive tsunami (Bilham, 2005). The historical large and great earthquakes ruptured only $\sim$200-300 km of the plate boundary, while the 2004 M_w 9.3 Sumatra-Andaman earthquake and its large aftershocks series ruptured more than 1300 km of the plate boundary. The tsunamigenic 2004 earthquake ruptured the affected regions by past earthquakes as well as intervening unbroken patches (Bilham, 2005).

The giant 2004 Sumatra-Andaman earthquake of M_w 9.3 is the third largest instrumentally recorded seismic event in the world. It triggered a massive tsunami with waves up to 30 m run-up, causing an estimated loss of 283,000 lives in fourteen countries (Jaiswal et al., 2011). Rather than tearing the land apart all at once, the rupture started beneath the epicenter (marker in Fig. 1.4(a)) and propagated to the north along the fault with an average rupture velocity 2 km/s (Ishii et al., 2005). The duration of rupture in Sumatra earthquake was 10 minutes. During this process, the fault ruptured at depth of 50 km below the ocean floor, where the two tectonic plates stuck together. The upper plate slid back upward and to the west by $\sim$15 m along the plate boundary near Banda-Aceh, Sumatra (Jaiswal et al., 2011). However, the slip was much smaller to the north of the Nicobar Island. Another great earthquake occurred just four months after the giant Sumatra earthquake of M_w 8.6 on March 28, 2005 (hereafter, 2005 Sumatra earthquake). The mainshock of 2004 Sumatra earthquake caused a total of 3460 aftershocks with magnitude ranging 3.5-7.5, while total of 1835 aftershocks of magnitude range 3.6-6.9 caused by mainshock of 2005 Sumatra earthquake. The aftershock sequences of these two events are shown in Fig. 1.4(b).

1.4.2 Mayotte Island

Mayotte Island, the oldest and easternmost cluster of complex volcanic edifies in the Comoros archipelago, located in the northern part of Mozambique Channel, between Northwest of Madagascar and Northeast of Mozambique (Fig. 1.5). It has total land area of 374 square kilometers and consists of two main volcanic islands: Petite-Terre (11 square kilometers) and Grande-Terre (363 square kilometers). Magmatic activity has been estimated to be onset between 10-20 Ma (Emerick and Duncan, 1982; Pelleter et al., 2014; Michon, 2016). The most recent eruption was reported to be about 7 Ma ago (Zinke et al., 2003, 2005).

Mayotte was affected by a number of tectonic events, including an episode of NE-SW trend rifting through Permo-Triassic, associated with fragmentation of Gondwana (Geiger et al., 2004; Reeves, 2014). The historical seismicity of Mayotte has incomplete view. However, based on the ancient information, four earthquakes has been recorded during 17th century that caused damage to many mosques. The location and magnitude of these events remains unverifiable (Hachim, 2004). Very few historical earthquakes of $M_w > 4$ hit the island, including the destructive events 23 April 1993 Mb 5.2, located 40 km south of island, causing a damage of around 1.7 M Euros and the 2011 Mb 4.9 event (Audru et al., 2010).

A seismic crisis started in the east of Mayotte Island 2018 May, which was widely felt by people, mainly during the first month of crisis. The largest event recorded during this sequence was on May 15, 2018, of magnitude M_w = 5.9 (Cesca et al., 2020; Lemoine et al., 2020). Over the course of a year, about 407 very long period signals and 7000 volcanic-tectonic earthquakes were recorded (Cesca et al., 2020). The origin

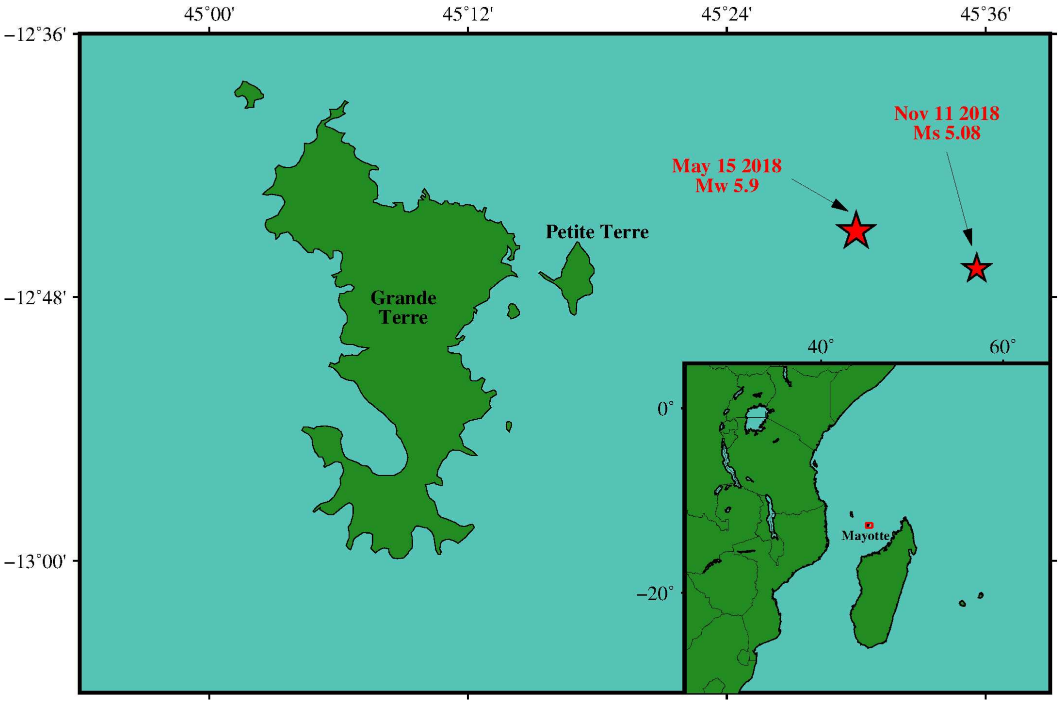

Fig. 1.5 Location of Mayotte Island. Red star is location of the largest earthquake and largest very long period event recorded during the seismic sequence over a period of one year from 2018. Red square in the inset map represents our study area.

of this earthquake activity has been attributed to the drainage and resonance of a deep magma reservoir (Cesca et al., 2020; Lemoine et al., 2020). At least 1.3 cubic kilometers of magma drained from the reservoir of about 10-15 kilometers diameter at a depth of 30±5 kilometers (Cesca et al., 2020). Since May 2018, repeated seismic activity has been associated with deformation of the surface of Mayotte, resulting in land subsidence. Our study focuses only on different, very low-frequency, signals recorded during this crisis, including a long-lasting event detected on November 11, 2018, with dominant frequency of $\sim$16s. in response to the depletion of the deep reservoir, a massive magmatic intrusion took place, reaching the seafloor in a submarine eruption, and finally leading to the birth of a new seafloor volcano. It was almost 1 km high in the bathymetric survey done a few months afterwards (Feuillet et al., 2021).

1.5 Thesis outline

In this section we report the outline of the thesis. This thesis is about implementing a time-reversal algorithm to investigate spatio-temporal characteristics of different earthquakes (Fig. 1.6) with the important differences that includes use of only surface waves rather than entire seismograms and their backward propagation is modeled using membrane-wave approach.

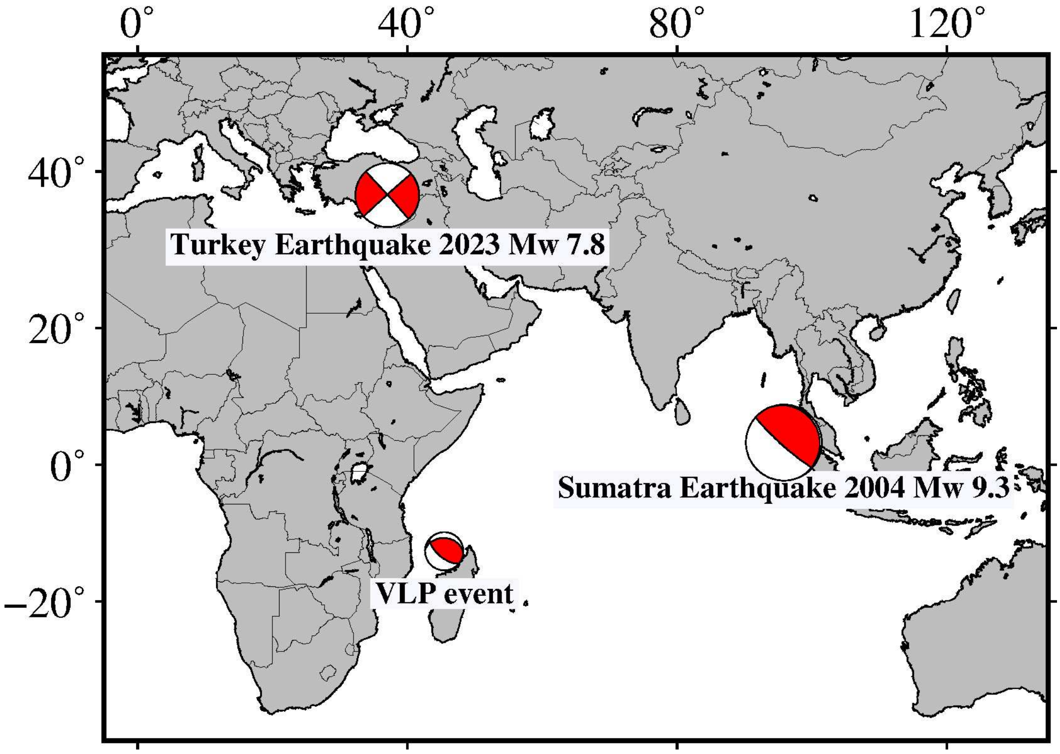

Fig. 1.6 Focal mechanism of earthquakes studied in this thesis.

Chapter 1 includes the motivation behind this thesis and some details about the study area and past earthquakes. The following chapter 2 describes the method of seismic time-reversal and ray-tracing algorithm, relying on the generalized spherical harmonic parameterization. Here, we validate our method through number of synthetic tests and apply it to one of the largest earthquakes, the great 26 December 2004 Sumatra-Andaman earthquake and reproduce the results which are in good agreement with the previous findings. In chapter 2, we use the same manuscript published on ”Geophysical Journal International”. Chapter 3 is about the investigation of a sequence of anomalous events (very low-frequency signals) associated with volcanism at Mayotte Island. This chapter contains the same structure of a manuscript to be submitted on ”Geophysical Journal International”. Chapter 4 is dedicated to the study of recent earthquake i.e., 6 February 2023, M_w = 7.8 Turkey earthquake. We analyze the rupture process of this event by combining surface wave time-reversal approach with ray-tracing algorithm using teleseismic and regional data.

Finally, in the last chapter, we provide the summary of this thesis and recommend future research directions. Our ultimate goal of this work is to bring some clarity to various aspects of the rupture evolution for better understanding kinematics of various earthquakes.

References

Audru, J.-C., Bitri, A., Desprats, J.-F., Dominique, P., Eucher, G., Hachim, S., Jossot, O., Mathon, C., Nédellec, J.-L., Sabourault, P. et al. (2010), 'Major natural hazards in a tropical volcanic island: A review for mayotte island, comoros archipelago, indian ocean', *Engineering geology* **114**(3-4), 364–381.

Beresnev, I. A. (2003), 'Uncertainties in finite-fault slip inversions: to what extent to believe?(a critical review)', *Bulletin of the Seismological Society of America* **93**(6), 2445–2458.

Bilham, R. (2005), 'A flying start, then a slow slip', *Science* **308**(5725), 1126–1127.

Bird, P. (2003), 'An updated digital model of plate boundaries', *Geochemistry, Geophysics, Geosystems* **4**(3).

Bock, Y., Prawirodirdjo, L., Genrich, J., Stevens, C., McCaffrey, R., Subarya, C., Puntodewo, S. and Calais, E. (2003), 'Crustal motion in indonesia from global positioning system measurements', *Journal of Geophysical Research: Solid Earth* **108**(B8).

Boschi, L., Molinari, I. and Reinwald, M. (2018), 'A simple method for earthquake location by surface-wave time reversal', *Geophysical Journal International* **215**(1), 1–21.

Boschi, L. and Woodhouse, J. H. (2006), 'Surface wave ray tracing and azimuthal anisotropy: a generalized spherical harmonic approach', *Geophysical Journal International* **164**(3), 569–578.

Briggs, R. W., Sieh, K., Meltzner, A. J., Natawidjaja, D., Galetzka, J., Suwargadi, B., Hsu, Y.-j., Simons, M., Hananto, N., Suprihanto, I. et al. (2006), 'Deformation and slip along the sunda megathrust in the great 2005 nias-simeulue earthquake', *Science* **311**(5769), 1897–1901.

Carbone, D., Zuccarello, L. and Saccorotti, G. (2008), 'Geophysical indications of magma uprising at mt etna during the december 2005 to january 2006 non-eruptive period', *Geophysical Research Letters* **35**(6).

Carbone, D., Zuccarello, L., Saccorotti, G. and Greco, F. (2006), 'Analysis of simultaneous gravity and tremor anomalies observed during the 2002–2003 etna eruption', *Earth and Planetary Science Letters* **245**(3-4), 616–629.

Cesca, S., Letort, J., Razafindrakoto, H. N., Heimann, S., Rivalta, E., Isken, M. P., Nikkhoo, M., Passarelli, L., Petersen, G. M., Cotton, F. et al. (2020), 'Drainage of a deep magma reservoir near mayotte inferred from seismicity and deformation', *Nature geoscience* **13**(1), 87–93.

Chakroun, N., Fink, M. A. and Wu, F. (1995), 'Time reversal processing in ultrasonic nondestructive testing', *IEEE transactions on ultrasonics, ferroelectrics, and frequency control* **42**(6), 1087–1098.

Chamot-Rooke, N. and Le Pichon, X. (1999), 'Gps determined eastward sundaland motion with respect to eurasia confirmed by earthquakes slip vectors at sunda and philippine trenches', *Earth and Planetary Science Letters* **173**(4), 439–455.

DeMets, C., Gordon, R. G., Argus, D. F. and Stein, S. (1994), 'Effect of recent revisions to the geomagnetic reversal time scale on estimates of current plate motions', *Geophysical research letters* **21**(20), 2191–2194.

Edelmann, G. F., Akal, T., Hodgkiss, W. S., Kim, S., Kuperman, W. A. and Song, H. C. (2002), 'An initial demonstration of underwater acoustic communication using time reversal', *IEEE journal of oceanic engineering* **27**(3), 602–609.

Ekström, G., Tromp, J. and Larson, E. W. (1997), 'Measurements and global models of surface wave propagation', *Journal of Geophysical Research: Solid Earth* **102**(B4), 8137–8157.

Emerick, C. and Duncan, R. (1982), 'Age progressive volcanism in the comores archipelago, western indian ocean and implications for somali plate tectonics', *Earth and Planetary Science Letters* **60**(3), 415–428.

Feuillet, N., Jorry, S., Crawford, W. C., Deplus, C., Thinon, I., Jacques, E., Saurel, J. M., Lemoine, A., Paquet, F., Satriano, C. et al. (2021), 'Birth of a large volcanic edifice offshore mayotte via lithosphere-scale dyke intrusion', *Nature Geoscience* **14**(10), 787–795.

Fink, M. (1997), 'Time reversed acoustics.', *Physics today* **50**(3), 34–40.

Fink, M. and Tanter, M. (2010), 'Multiwave imaging and super resolution', *Phys. Today* **63**(2), 28–33.

Fukahata, Y., Yagi, Y. and Rivera, L. (2014), 'Theoretical relationship between back-projection imaging and classical linear inverse solutions', *Geophysical Journal International* **196**(1), 552–559.

Geiger, M., Clark, D. N. and Mette, W. (2004), 'Reappraisal of the timing of the breakup of gondwana based on sedimentological and seismic evidence from the morondava basin, madagascar', *Journal of African Earth Sciences* **38**(4), 363–381.

Hachim, S. (2004), 'Catastrophes: Mayotte perd sa mémoire', *Catastrophes naturelles et mémoire collectivea Mayotte. Mémoire de DEA de Géographie. Université Paul Valéry, Montpellier III* .

Hartzell, S., Liu, P. and Mendoza, C. (1996), 'The 1994 northridge, california, earthquake: Investigation of rupture velocity, risetime, and high-frequency radiation', *Journal of Geophysical Research: Solid Earth* **101**(B9), 20091–20108.

Ishii, M., Shearer, P. M., Houston, H. and Vidale, J. E. (2005), 'Extent, duration and speed of the 2004 sumatra–andaman earthquake imaged by the hi-net array', *Nature* **435**(7044), 933–936.

Jaiswal, R., Singh, A., Rastogi, B. and Murty, T. (2011), 'Aftershock sequences of two great sumatran earthquakes of 2004 and 2005 and simulation of the minor tsunami generated on september 12, 2007 in the indian ocean and its effect', *Natural Hazards* **57**, 7–26.

Kayal, J. (2008), ‘Northeast india, myanmar, bangladesh and andaman-sumatra region’, *Microearthquake Seismology and Seismotectonics of South Asia* pp. 266–347.

Konca, A. O., Avouac, J.-P., Sladen, A., Meltzner, A. J., Sieh, K., Fang, P., Li, Z., Galetzka, J., Genrich, J., Chlieh, M. et al. (2008), ‘Partial rupture of a locked patch of the sumatra megathrust during the 2007 earthquake sequence’, *Nature* **456**(7222), 631–635.

Lemoine, A., Briole, P., Bertil, D., Roullé, A., Foumelis, M., Thinon, I., Raucoules, D., de Michele, M., Valty, P. and Hoste Colomer, R. (2020), ‘The 2018–2019 seismo-volcanic crisis east of mayotte, comoros islands: seismicity and ground deformation markers of an exceptional submarine eruption’, *Geophysical Journal International* **223**(1), 22–44.

Lokmer, I., Bean, C. J., Saccorotti, G. and Patane, D. (2007), ‘Moment-tensor inversion of lp events recorded on etna in 2004 using constraints obtained from wave simulation tests’, *Geophysical Research Letters* **34**(22).

Mai, P. M., Schorlemmer, D., Page, M., Ampuero, J.-P., Asano, K., Causse, M., Custodio, S., Fan, W., Festa, G., Galis, M. et al. (2016), ‘The earthquake-source inversion validation (siv) project’, *Seismological Research Letters* **87**(3), 690–708.

McCaffrey, R. (2009), ‘The tectonic framework of the sumatran subduction zone’, *Annual Review of Earth and Planetary Sciences* **37**, 345–366.

McMechan, G. A. (1982), ‘Determination of source parameters by wavefield extrapolation’, *Geophysical Journal International* **71**(3), 613–628.

Michon, L. (2016), ‘The volcanism of the comoros archipelago integrated at a regional scale’, *Active Volcanoes of the Southwest Indian Ocean: Piton de la Fournaise and Karthala* pp. 333–344.

Monelli, D. and Mai, P. M. (2008), ‘Bayesian inference of kinematic earthquake rupture parameters through fitting of strong motion data’, *Geophysical Journal International* **173**(1), 220–232.

Natawidjaja, D. H., Sieh, K., Chlieh, M., Galetzka, J., Suwargadi, B. W., Cheng, H., Edwards, R. L., Avouac, J.-P. and Ward, S. N. (2006), 'Source parameters of the great sumatran megathrust earthquakes of 1797 and 1833 inferred from coral microatolls', *Journal of Geophysical Research: Solid Earth* **111**(B6).

Olson, A. H. and Apsel, R. J. (1982), 'Finite faults and inverse theory with applications to the 1979 imperial valley earthquake', *Bulletin of the Seismological Society of America* **72**(6A), 1969–2001.

Parvulescu, A. and Clay, C. (1965), 'Reproducibility of signal transmissions in the ocean', *Radio and Electronic Engineer* **29**(4), 223–228.

Pelleter, A.-A., Caroff, M., Cordier, C., Bachelery, P., Nehlig, P., Debeuf, D. and Arnaud, N. (2014), 'Melilite-bearing lavas in mayotte (france): An insight into the mantle source below the comores', *Lithos* **208**, 281–297.

Reeves, C. (2014), 'The position of madagascar within gondwana and its movements during gondwana dispersal', *Journal of African Earth Sciences* **94**, 45–57.

Sutin, A. M., TenCate, J. A. and Johnson, P. A. (2004), 'Single-channel time reversal in elastic solids', *The Journal of the Acoustical Society of America* **116**(5), 2779–2784.

Zinke, J., Reijmer, J. J., Taviani, M., Dullo, W.-C. and Thomassin, B. (2005), 'Facies and faunal assemblage changes in response to the holocene transgression in the lagoon of mayotte (comoro archipelago, sw indian ocean)', *Facies* **50**, 391–408.

Zinke, J., Reijmer, J., Thomassin, B., Dullo, W.-C., Grootes, P. and Erlenkeuser, H. (2003), 'Postglacial flooding history of mayotte lagoon (comoro archipelago, southwest indian ocean)', *Marine Geology* **194**(3-4), 181–196.

CHAPTER 2

Seismic source mapping by surface wave time reversal: application to the great 2004 Sumatra earthquake

Apsara Sharma Dhakal[1], *Irene Molinari*[2], *Lapo Boschi*[1,2,3]

(Geophys. J. Int. (2023) 233, 1018–1035,
`https://doi.org/10.1093/gji/ggac493)`

[1] [2] [3]

ABSTRACT

Different approaches to map seismic rupture in space and time often lead to incoherent results for the same event. Building on earlier work by our team, we 'time-reverse' and 'backpropagate' seismic surface wave recordings to study the focusing of the time-reversed field at the seismic source. Currently used source-imaging methods relying on seismic recordings neglect the information carried by surface waves, and mostly focus on the P-wave arrival alone. Our new method combines seismic time reversal approach with a surface wave ray-tracing algorithm based on a generalized spherical-harmonic parametrization of surface wave phase velocity, accounting for azimuthal anisotropy. It is applied to surface wave signal filtered within narrow-frequency bands, so that the inherently 3-D problem of simulating surface wave propagation is separated into a suite of 2-D problems, each of relatively limited computational cost. We validate our method through a number of synthetic tests, then apply it to the great 2004 Sumatra-Andaman earthquake, characterized by the extremely large extent of the ruptured fault. Many studies have estimated its rupture characteristics from seismological data (e.g., Lomax, Ni et al., Guilbert et al., Ishii et al., Krüger and Ohrnberger, Jaffe et al.) and geodetic

---

[1] Departimento Di Geoscienze, Università Degli Studi di 35131, Padova, Italy
[2] Istituto Nazionale di Geofisica e Vulcanologia, Sezioni di, 40128, Bologna, Italy
[3] Institut des sciences de la terre paris sorbonne université, Paris, France

data (e.g., Banerjee et al., Catherine et al., Vigny et al., Hashimoto et al.). Applying our technique to recordings from only 89 stations of the Global Seismographic Network (GSN) and bandpass filtering the corresponding surface wave signal around 80- to-120, 50-to-110 and 40-to-90 s, we reproduce the findings of earlier studies, including in particular the northward direction of rupture propagation, its approximate spatial extent and duration, and the locations of the areas where most energy appears to be released.

Keywords: *Earthquake source observations*, *Surface waves and free oscillations*, *Theoretical seismology*, *Wave propagation*

2.1 Introduction

The problem of reconstructing the slip distribution on a seismic fault is notoriously non-unique (Mai et al., 2016). Our study is motivated by the idea that non-uniqueness could be reduced by taking into account a section of the seismogram that is usually not included in source inversions: the surface waves. The benefits of harvesting such information, in the context of seismic source inversion, were illustrated in some detail by Boschi et al. (2018): the fact that surface waves are dispersive emphasizes the focusing of backpropagated time-reversed signal at the source; their broad frequency range should help constraining source structure at different depth and/or of different scale length; the fact that a narrow-band-filtered surface wave can be approximated as a membrane wave (Tanimoto, 1990; Tromp and Dahlen, 1993; Peter et al., 2007, 2009) results in simpler and less computationally intensive software.

We exploit the Rayleigh waves to reconstruct the seismic source by time-reversing and backpropagating (Fink, 1999, 2006; Fink et al., 2003) filtered vertical-component seismograms from a relatively large number of broad-band stations distributed as uniformly as possible around the globe and along all azimuths from the epicenter. In practice, we conduct wave-propagation simulations where receivers act as virtual sources, emitting the real-world signal that they have recorded, but reversed with respect to time. Time-reversed signals are propagated through a reliable earth model and eventually focus on the real-world source (the earthquake).

The method that we describe and validate here is an extension to the global scale of that of Boschi et al. (2018): the flat-earth ray- tracing scheme is replaced with the one of Boschi and Woodhouse (2006) in order to calculate surface wave ray paths on a spherical earth and, importantly, allows to account not only for isotropic phase velocity heterogeneity, but also for laterally varying azimuthal anisotropy of surface waves. Compared to other declinations of so-called time-reversal and/or backpropagation of seismic waves, our source-imaging method is restricted to surface wave data, which

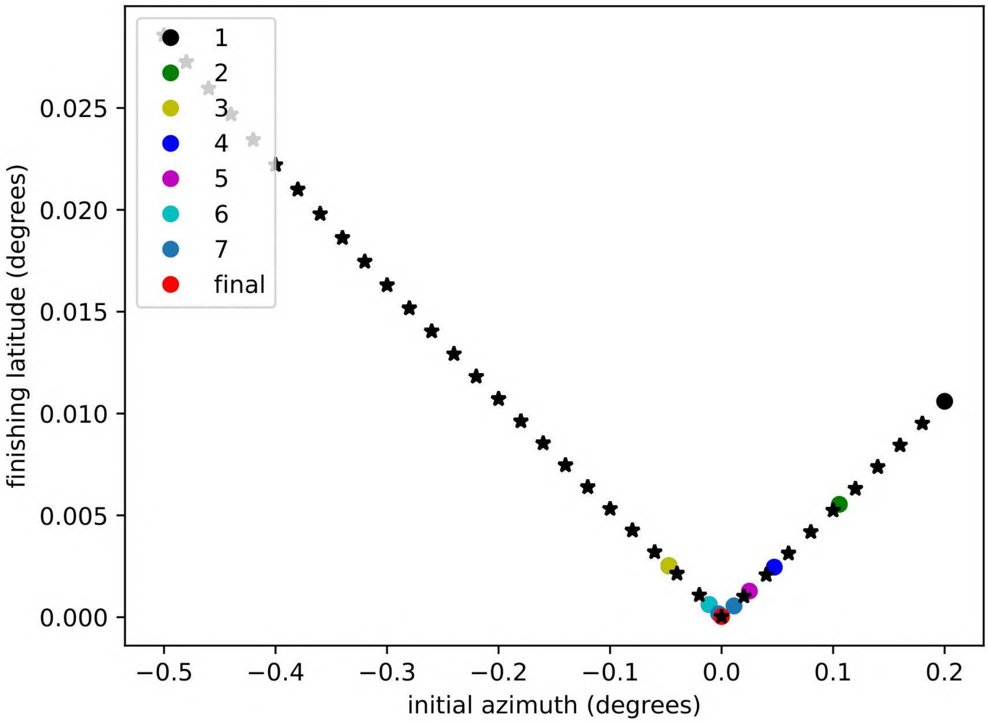

Fig. 2.1 Finishing latitude as a function of the initial azimuth obtained using the golden-section-search method implemented in this study (colored circles) and the brute-force method of Boschi and Woodhouse (2006). Our new approach reduces computation time by about one order of magnitude. Finishing latitude = 0 corresponds to convergence to the correct ray path.

can be approximated as membrane waves and modelled both via ray-tracing or numerical simulations. Conversely, backprojection as described, for example, by Ishii et al. (2005) have systematically been restricted to body wave (typically P-wave) traveltimes, with the sole exception of a surface wave study by Roten et al. (2012); time-reversal seismology as implemented by (Larmat et al., 2006, 2008) relies on the more rigorous, but computationally much more demanding, numerical 3-D modelling of the entire seismic waveform. In the following we describe our method, validate it via application to global-scale synthetic data, and apply it to a set of broad-band recordings of the 2004 December 26, Sumatra-Andaman Earthquake. Sumatra event is one of the most studied earthquakes in history, with a well-documented rupture of long duration and large spatial extent. Our results are compared with those obtained from high-frequency body wave (Lomax, 2005; Ni et al., 2005), tsunami data (Lay et al., 2005), geodetic data

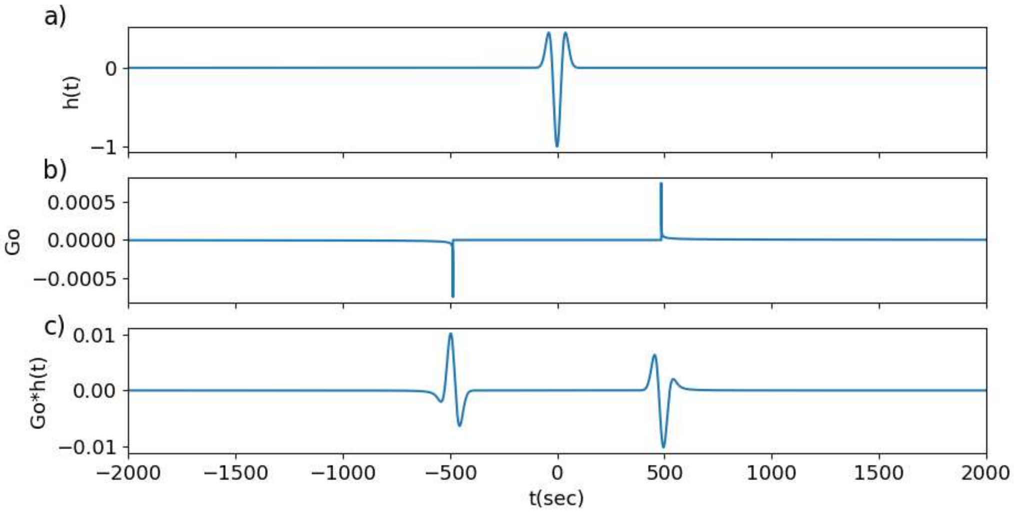

Fig. 2.2 (a) Source time function (100 s ricker-wavelet), (b) Green's function with interstation distance 2000 km and wave speed 4.12 km/s and (c) convolution of (a) and (b).

(Catherine et al., 2005; Vigny et al., 2005; Hashimoto et al., 2006; Jaffe et al., 2006) and array analysis (Guilbert et al., 2005; Ishii et al., 2005; Krüger and Ohrnberger, 2005; Yao et al., 2011). We find that the robust features of the Sumatran rupture, confirmed by most of the mentioned studies, are reproduced by our method as well, and we consider this to be an important confirmation of its validity.

2.2 Theory and Methods

2.2.1 Surface wave modelling via ray tracing

Surface waves propagate along the Earth's outer surface, and they involve the oscillation of the earth's crust and top of the upper mantle. Surface wave are dispersed meaning that different periods are sensitive to Earth structure at different depths (typically maximum at a depth roughly equal to half a wavelength) and their velocity depends on the mechanical properties of the earth at the depth range of interest. A practical consequence of surface wave dispersion is that their propagation can be studied separately for a set of narrow-frequency bands (e.g., Ekström et al., 1997), or surface wave 'modes', each with its own laterally varying phase velocity and, consequently, propagation path

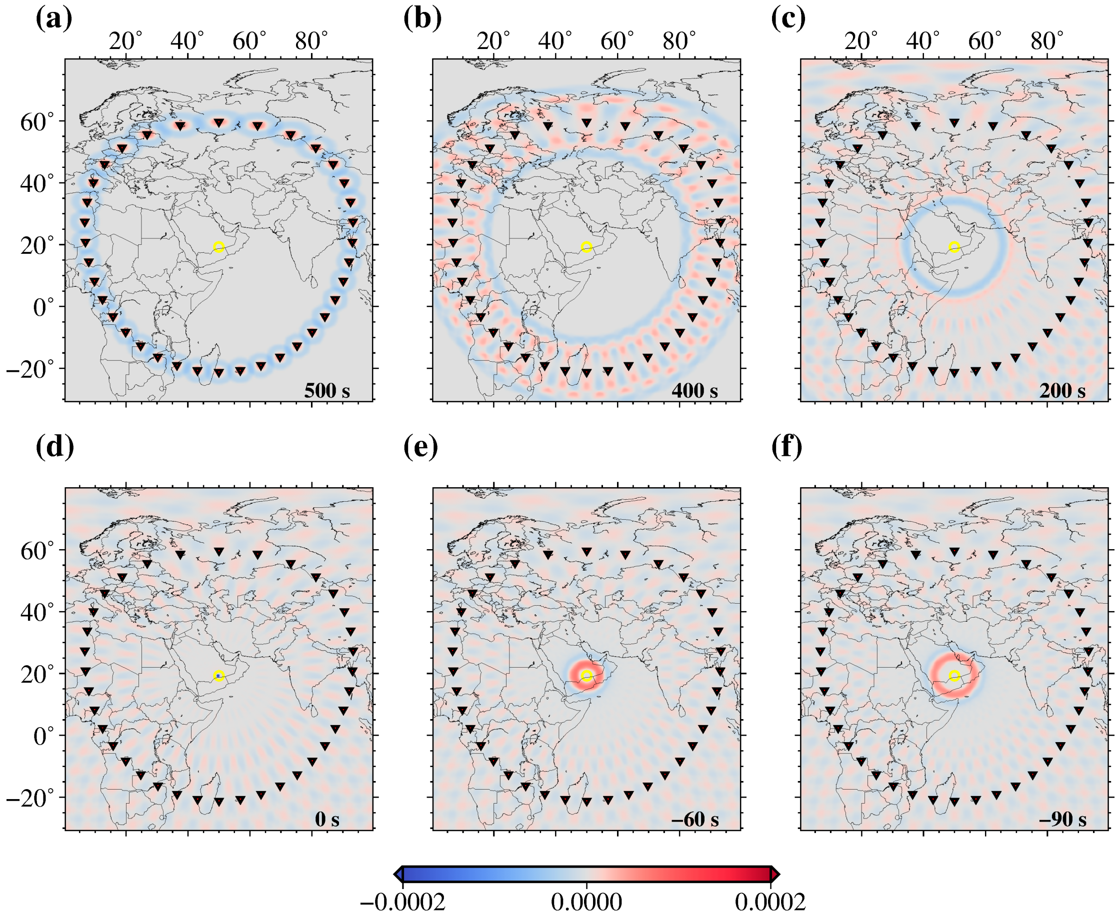

Fig. 2.3 Snapshots of time-reversal simulation where 100 s surface waves are modelled in a heterogeneous, isotropic phase velocity model and backpropagated in the same model. In this synthetic experiment, stations (inverted triangles) are distributed along a 'circle' of radius 4500 km, centered at the source location (yellow circle). Snapshot (d) corresponds to focusing of the time-reversed wavefield onto the location of the source. The time t = 0s corresponds to the origin time; positive *t* corresponds to time before focusing onto the source location.

along the earth surface. Starting with the early study of Tanimoto and Anderson (1985), surface waves have been known to be azimuthally anisotropic, that is, their velocity depends locally on their direction of propagation. Smith and Dahlen (1973; 1975) show that a relative perturbation in phase velocity c, with respect to a reference value c_0, can be written as

$$\frac{\delta c(\theta,\phi,\zeta)}{c_o} = \varepsilon_0(\theta,\phi)+\varepsilon_1(\theta,\phi)\cos(2\zeta)+\varepsilon_2(\theta,\phi)\sin(2\zeta)+\varepsilon_3(\theta,\phi)\cos(4\zeta)+\varepsilon_4(\theta,\phi)\sin(4\zeta), \tag{1}$$

where θ, ϕ denote latitude and longitude, respectively, along the earth's surface, ζ is the azimuth of propagation, and the four functions ε_1, ε_2, etc. are all required to describe propagation in the presence of azimuthal anisotropy ($\varepsilon_0(\theta, \phi)$ coincides with isotropic velocity heterogeneity). At each location θ, ϕ, an independent set of values for ε_0, ε_1, etc. is associated to each surface-wave frequency, i.e., to each surface-wave mode. These azimuthal terms ε_i are functions of frequency because of surface wave dispersion, and depend in a known way on the 21 anisotropic elastic parameters of the medium through which the waves is propagating.

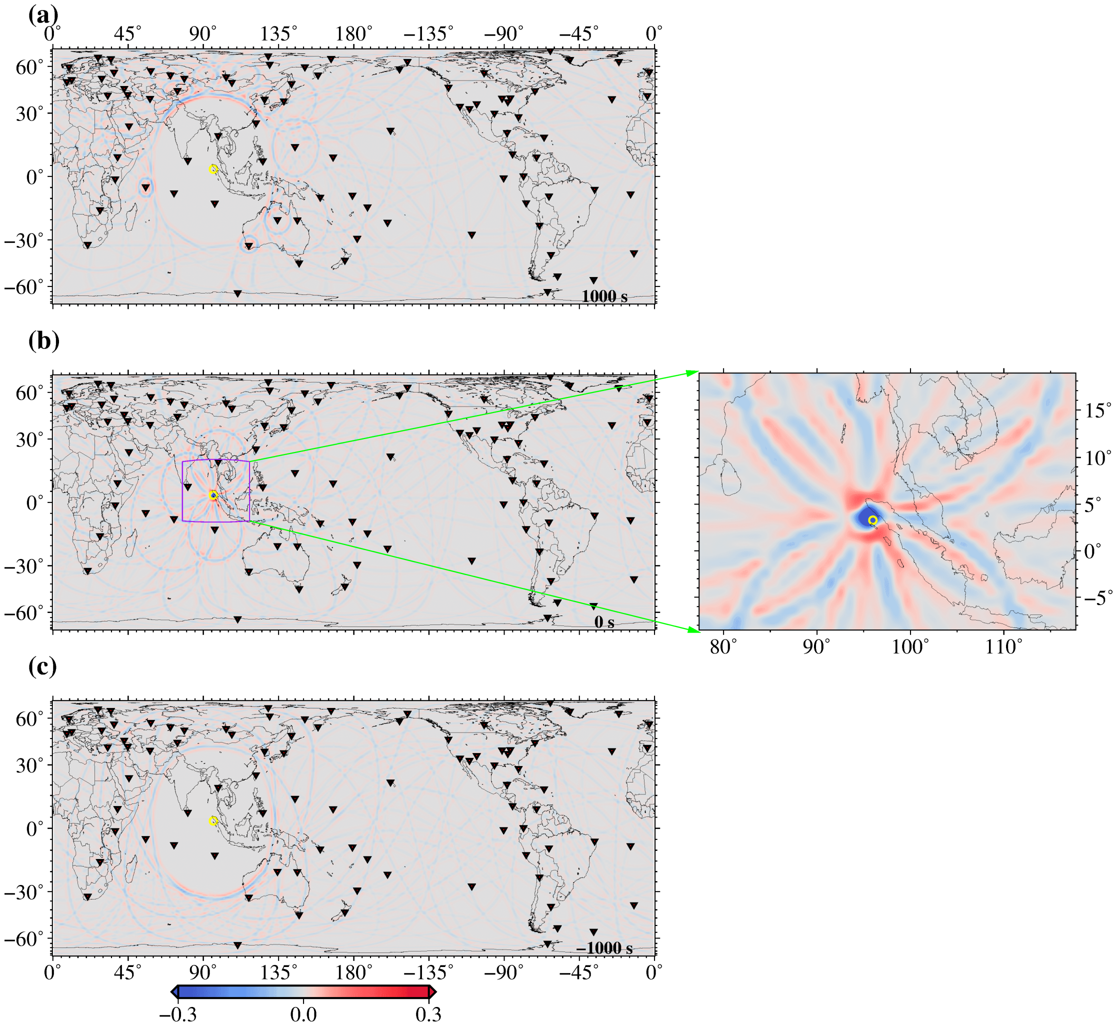

Fig. 2.4 Similar to Fig. 2.3, snapshots of time-reversal simulation where 100 s surface waves are modelled in a heterogeneous, isotropic phase velocity model and backpropagated in the same model. Negative time show non-physical signal that continues to propagate after focusing. Panel on the right shows an enlarged detail of the source region from the map in panel (b), that is, the origin time, as indicated by the green lines.

Our method allows for surface-wave azimuthal anisotropy, which we parameterize according to the generalized-spherical-harmonic scheme described by Trampert and Woodhouse (2003) and Boschi and Woodhouse (2006). Boschi and Woodhouse (2006) discuss the effectiveness of this parameterization for tracing surface-wave ray paths, in particular in the presence of azimuthal anisotropy, which makes simpler isotropic velocity parameterization schemes inadequate. Surface-wave rays are traced according to the ray tracing equations given e.g. by Larson et al. (1998),

$$\frac{d\theta}{d\phi} = -\frac{\sin(\theta)(\tan(\zeta) + \partial_\zeta \ln c)}{1 - \tan(\zeta)\partial_\zeta \ln c}, \tag{2}$$

$$\frac{d\zeta}{d\phi} = \frac{\sin(\theta)\partial_\theta \ln c + \tan(\zeta)\partial_\phi \ln c - \cos(\theta)}{1 - \tan(\zeta)\partial_\zeta \ln c}, \tag{3}$$

The differential eqs. 2 and 3 describe how the latitude and azimuth change as functions of longitude along the ray path, and they are most effectively integrated in a reference frame where source and receiver are located on the equator. We solve them following Boschi and Woodhouse (2006), starting with the values of θ and ϕ that correspond to one of the endpoints of the ray, making a guess for the initial azimuth, and integrating numerically until the other endpoint is reached (in practice, a point along the ray path is found when the distance from the ray endpoint is smaller than a certain threshold), or an unreasonably large distance is covered. In the former case, the ray has been successfully traced, while in the latter, the integration should be repeated, assigning a different value to the initial azimuth. In mathematical terms, this is an example of applying the "shooting method" to solve a two-point boundary value problem (e.g., Press et al., 1992).

Because seismic/acoustic time reversal is more effective the more recordings are back-propagated, our experiment requires many ray paths to be traced; we accordingly optimized the search for the correct initial azimuth, reducing the number of iterations via the "golden-section search method" (e.g., Press et al., 1992, chap 10), allowing very fast convergence to the correct initial azimuth and ray path. We compared the new ray tracing method implemented here against that of Boschi and Woodhouse (2006), using both to trace rays between a large set of randomly located sources and receivers. The gain in both computational speed and accuracy is evident from an example shown in Fig. 2.1, with source and station located at (42.80°N, 16.70°E) and (43.04°N, 12.66°E)

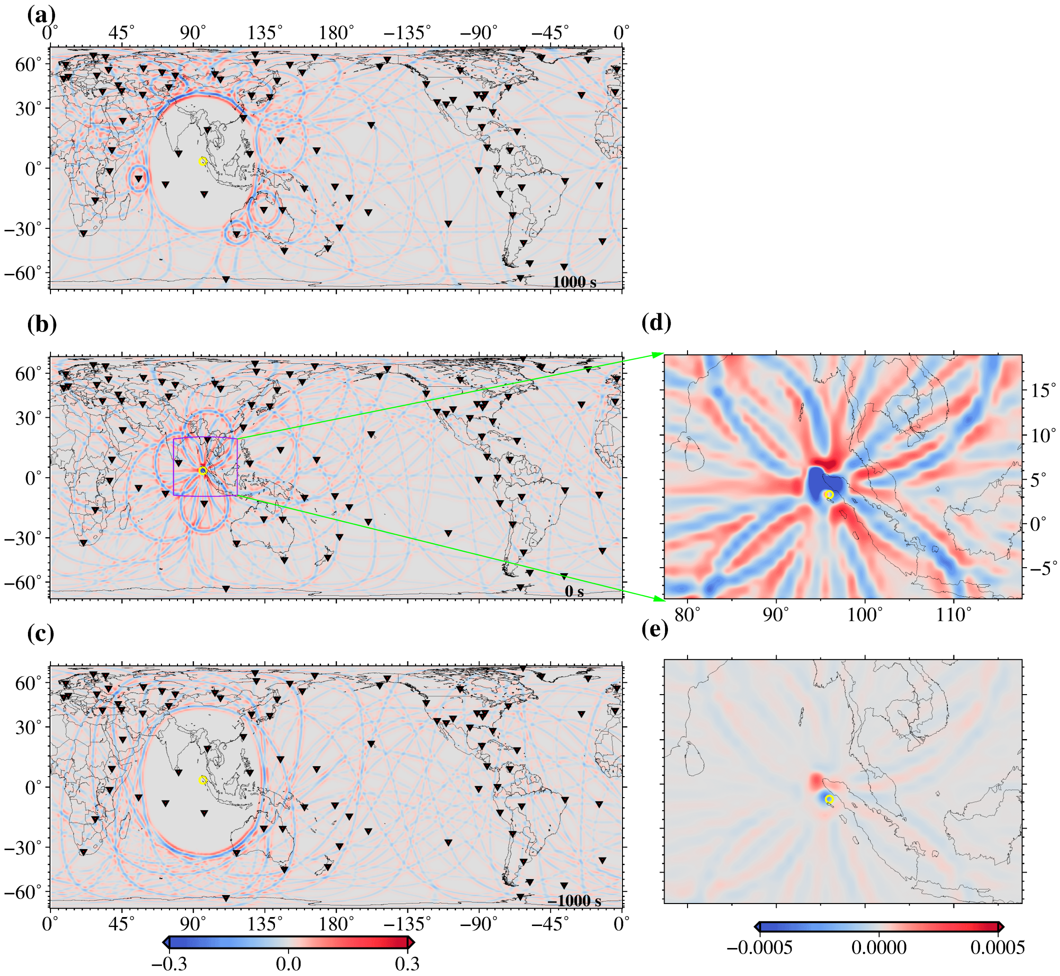

Fig. 2.5 Snapshots of the time-reversal simulation obtained by using synthetic data computed in heterogeneous model and backpropagated through homogeneous model. The times at which the wavefield is shown are same as Fig. 2.4, and, likewise, the image in panel (d) is a detail of that in panel (b). Panel (e) shows the difference between the time-reversed wavefield displayed here, and that of Fig. 2.4(b), that is, the error caused by neglecting heterogeneity in phase velocity. The color scale in panel (e) is different than the one used in all other panels, because the error is very small.

respectively. In this case, the golden-search method achieves convergence after 8 iterations while the "Brute-force approach" of Boschi and Woodhouse (2006) required 36 iterations. A similar improvement is found regardless of source and station locations.

Once the ray path between two points is determined, Rayleigh-wave phase can be calculated as described by Boschi and Woodhouse (2006).

2.2.2 Surface-wave time reversal

Because of the spatial reciprocity and time invariance of the elastic wave equation, a time-reversed wavefield focuses on its original source. In a medium that is slightly heterogeneous like the earth, focusing is achieved, in practice, if the wavefield is recorded at (and backpropagated from) a uniformly distributed set of receivers that cover all azimuths of propagation (e.g., Fink, 1999, 2006; Fink et al., 2003).

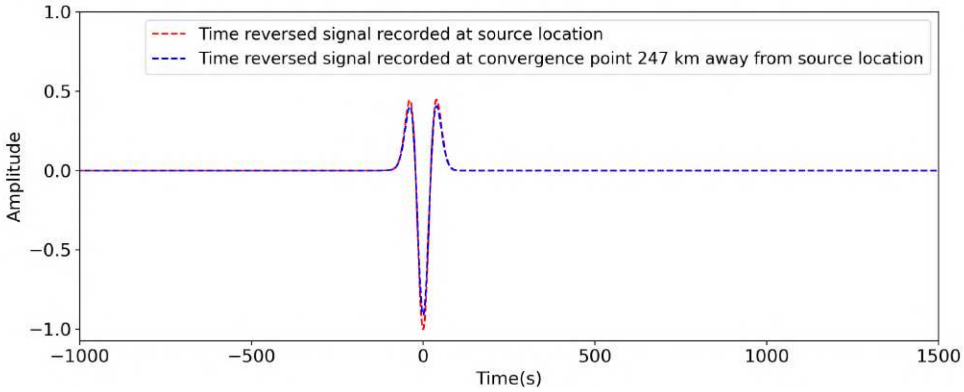

Fig. 2.6 Time-reversed and backpropagated displacement at and near the source location, resulting from the time-reversal simulation of Figs 2.4 and 2.5. The red dashed curve is obtained using synthetic data from heterogeneous model and backpropagated through the same heterogeneous model while the blue dashed curve is obtained using synthetic data from heterogeneous model and backpropagated through homogeneous model. At time t = 0 s, peaks are not equally sharp.

In seismology, the time-reversal concept can help to reconstruct the location, geometry and mechanics of an earthquake. However, seismic data are very sensitive to heterogeneities in earth structure, and the distribution of seismic stations is not always uniform (in fact, it can be very non-uniform depending on the scale of the problem, and/or the geographic area of study). The effectiveness of seismic time-reversal is accordingly limited by station distribution and errors in the velocity models used to simulate wave (back)propagation. Rietbrock and Scherbaum (1994) made a first attempt at seismic time reversal but limited to local scale and to the acoustic approximation (compressional waves only). Larmat et al. (2006; 2008) time reversed the entire seismic waveform, backpropagating it in a global, heterogeneous earth model via 3-D numerical simulation. The computational cost of such endeavor forced them to low-pass filter the data, studying only the longer wavelength portion of the seismic signal.

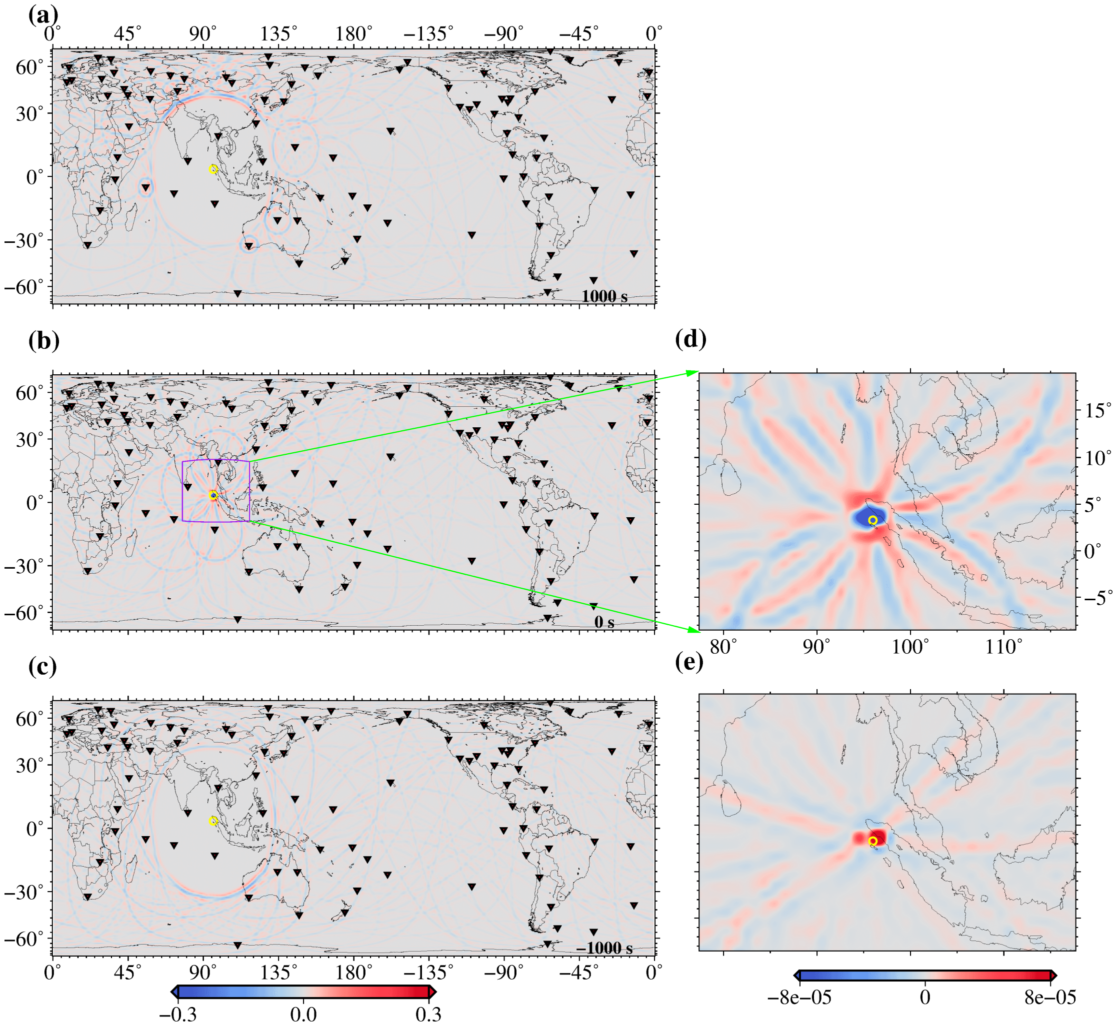

Fig. 2.7 Snapshots of the time-reversal simulation obtained from synthetic data computed in a heterogeneous, anisotropic model and backpropagated through the exact same model. Snapshots were selected at the same times as in Fig. 2.4. Panel (e) is the zoomed-in plot representing the difference between time-reversed wavefield obtained when anisotropy is accounted for and neglected. The color scale in panel (e) is different than the one used in all other panels as the error is very small.

Many other authors (Ishii et al., 2005; Krüger and Ohrnberger, 2005; Lay et al., 2005; Merrifield et al., 2005; Ni et al., 2005; Yao et al., 2011) back-propagated only the arrival time of seismic signal, neglecting waveform information; this is usually referred to as back-propagation rather than time reversal, and is usually limited to body waves. Only Roten et al. (2012) have tried to back-propagate the arrival times of surface-wave modes, but without any advanced modeling of wave propagation, and neglecting the information carried by the waveform (amplitude).

Surface-wave back propagation can be implemented via the membrane-wave approach (Peter et al., 2009; Tanimoto, 1990), reducing the 3-D momentum equation to 2-D by separating the contribution of each mode and modeling each mode separately, which significantly reduces the computational costs. This simple approach is sufficient to correctly model the phase of individual surface-wave modes. Thus, if one considers only the phase, and not the amplitude of surface waves, multiple forms of data analysis (imaging, back-propagation) are possible using the surface-wave potentials and associated 2-D scalar equation.

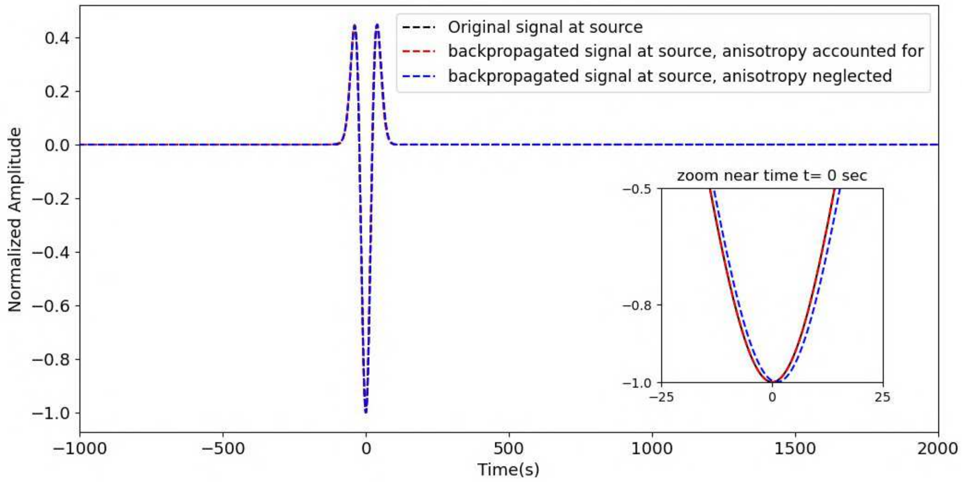

Fig. 2.8 Normalized time-reversed backpropagated displacement at the location of the source, resulting from the time-reversal simulation of Fig. 2.7. Synthetics were computed in a heterogeneous, anisotropic phase-velocity model and backpropagated in the same heterogeneous model without (blue dashed curve) and with anisotropy (red dashed curve). When anisotropy is accounted for, the source signal is reproduced almost perfectly; neglecting anisotropy results in a discrepancy of the order of 1 s.

Here, we reduce the problem to two dimensions, similar to Peter et al. (2009), but, rather than implementing finite-element simulations to model wave propagation, we trace the rays as in Boschi et al. (2018). The equivalence of the two approaches is discussed by Boschi et al. (2018).

The theory of surface-wave time reversal can be summarized by the frequency-domain equation (45) of Boschi et al. (2018), that reads

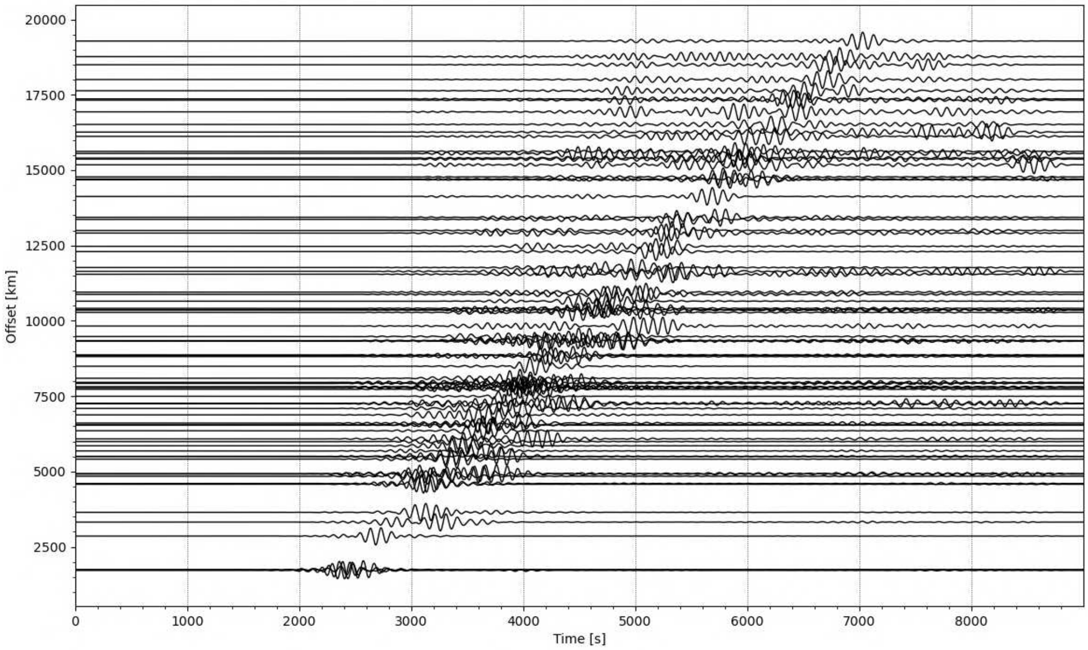

Fig. 2.9 Vertical component recordings of Mw 9.3 Sumatra earthquake from 89 IRIS/USGS GSN, filtered in the period band 80-to-120 s.

$$h^*(\omega)\left[G^*_{2D}(\mathbf{x}_A,\mathbf{x}_B,\omega)-G_{2D}(\mathbf{x}_B,\mathbf{x}_A,\omega)\right]\approx\frac{2i\omega}{c_o}\int_{\partial s}d\mathbf{x}'\left[h^*(\omega)G^*_{2D}(\mathbf{x}',\mathbf{x}_B,\omega)G_{2D}(\mathbf{x}',\mathbf{x}_A,\omega)\right], \tag{4}$$

where $\mathbf{x}_A$ is an arbitrary observation point, $\mathbf{x}_B$ is the location of a source within the area S bounded by ∂S, $h(\omega)$ is the Fourier transform a signal emitted at $\mathbf{x}_B$, and G_{2D} is the 2D acoustic Green's function (e.g., Boschi and Weemstra, 2015), which Boschi et al. (2018) show to be proportional to the vertical-component Rayleigh-wave Green's function. The left-hand side of eq. (4) can be simplified,

$$\left[G^*_{2D}(\mathbf{x}_A,\mathbf{x}_B,\omega)-G_{2D}(\mathbf{x}_A,\mathbf{x}_B,\omega)\right]h^*(\omega)=\left\{-2iIm\left[G_{2D}(\mathbf{x}_A,\mathbf{x}_B,\omega)\right]\right\}h^*(\omega),$$

and it can be shown (e.g. appendix B of Boschi and Weemstra (2015)) that

$$Im(G_{2D}(\mathbf{x}_A,\mathbf{x}_B,\omega))=-iG_o(\mathbf{x}_A,\mathbf{x}_B,\omega),$$

where $G_o(\mathbf{x}_A, \mathbf{x}_B, \omega)$ is a purely imaginary, odd function, whose inverse Fourier transform is:

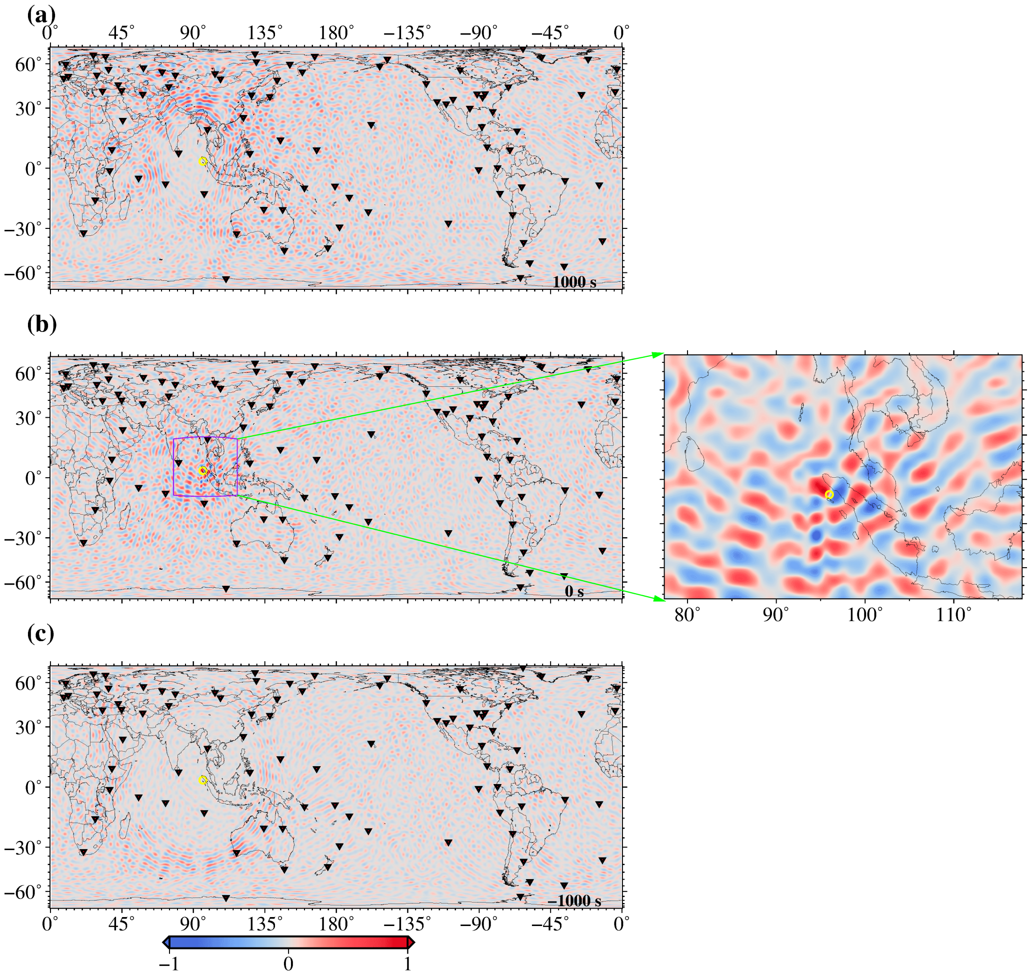

Fig. 2.10 Snapshots of surface wave ray tracing time reversal simulation of real earthquake (Sumatra earthquake, 26 December 2004, Mw 9.3), in the 80 -to- 120 s period band using recordings from 89 stations. We define t=0 as earthquake origin time reported by the USGS. Snapshots (a) is taken at time t=1000 s; (b) at t=0 s, and (c) at t= -1000 s; negative t corresponds to time after focusing in a time-reversal simulation. The results were calculated in meters where as here and in the following, it is normalized so that the maximum of its absolute value for all modeled locations and times, is 1.

$$G_o(\mathbf{x}_A, \mathbf{x}_B, t) = \frac{1}{2}G(\mathbf{x}_A, \mathbf{x}_B, t) - \frac{1}{2}G(\mathbf{x}_A, \mathbf{x}_B, -t).$$

It follows that the left-hand side of (4) can be further rewritten

$$-2iIm\left[G_o(\mathbf{x}_A, \mathbf{x}_B, \omega)\right] h^*(\omega) = +2i^2 G_o(\mathbf{x}_A, \mathbf{x}_B, \omega)h^*(\omega) = -2G_o(\mathbf{x}_A, \mathbf{x}_B, \omega)h^*(\omega).$$

Substituting into eq. (4), we obtain

$$h^*(\omega)\left[G_o(\mathbf{x}_A, \mathbf{x}_B, \omega)\right] \approx \frac{i\omega}{c_o}\int_{\partial s} d\mathbf{x}'[h^*(\omega)G^*_{2D}(\mathbf{x}', \mathbf{x}_B, \omega)G_{2D}(\mathbf{x}', \mathbf{x}_A, \omega)]. \qquad (5)$$

Eq. (4) or (5) can be interpreted, for example, as follows. Look first at the right-hand side: the Rayleigh wave $h(\omega)$ emitted at $\mathbf{x}_B$ is recorded as $h(\omega)G_{2D}(\mathbf{x}', \mathbf{x}_B, \omega)$ at a set of points $\mathbf{x}'$ along a closed curve ∂S on the earth's surface; it is then time-reversed (hence the complex-conjugation of $h(\omega)G_{2D}(\mathbf{x}', \mathbf{x}_B, \omega)$), re-emitted from $\mathbf{x}'$, and recorded at $\mathbf{x}_A$ (hence the convolution – multiplication in the frequency domain – with $G_{2D}(\mathbf{x}', \mathbf{x}_A, \omega)$). Now, integrating over ∂S is equivalent to having all receivers $\mathbf{x}'$ emitting their time-reversed recordings, whose sum is then received at $\mathbf{x}_A$. The result of all this, multiplied by - $\frac{i\omega}{c_o}$, must coincide with the product of $h^*(\omega)$ with $G_o(\mathbf{x}_A, \mathbf{x}_B, \omega)$. $h^*(\omega)$ is the Fourier transform of $h(-t)$, i.e., the time-reversed version of the signal originally emitted at the source. Now, by the properties of Fourier transforms, the inverse Fourier transform of $h^*(\omega)G_o(\mathbf{x}_A, \mathbf{x}_B, \omega)$ coincides with the convolution of $h(-t)$ and $G_o(-t)$, that is,

$$F^{-1}\left[h^*(\omega)[G_o(\mathbf{x}_A,\mathbf{x}_B,\omega]\right.=\int_{-\infty}^{\infty}h(-\tau)G_o(\mathbf{x}_A,\mathbf{x}_B,t+\tau)d\tau. \tag{6}$$

Since the Green's function G_o is singular at zero distance from the source, we infer from eqs. (5) and (6) that the time reversed wave-field calculated according to their right-hand sides becomes singular for $\mathbf{x}_A = \mathbf{x}_B$, where in practice we expect to see a prominent maximum. In real-world applications, station distribution is often far from perfect, and not all azimuths can be covered with uniform density. This limits the accuracy with which the maximum of the time-reversed wavefield is correctly mapped at the source location $\mathbf{x}_B$.

For the sake of illustration, we implement the right-hand side of eq. (6), calculating the time-domain convolution of G_o (obtained by combining eqs. (E15) and (B6) of Boschi and Weemstra (2015) and shown in Fig. 2.2b) with the source time function (100s Ricker wavelet, Fig. 2.2a) used throughout this study. We take receiver $\mathbf{x}_A$ and source $\mathbf{x}_B$ to lay at a distance of 2000 km from one another, and constant wave speed c=4.12 km/s. The resulting trace, shown in Fig. 2.2(c), is the time-reversed signal that would be modeled at $\mathbf{x}_A$, in an ideal time-reversal experiment, were stations re-emit from all azimuths.

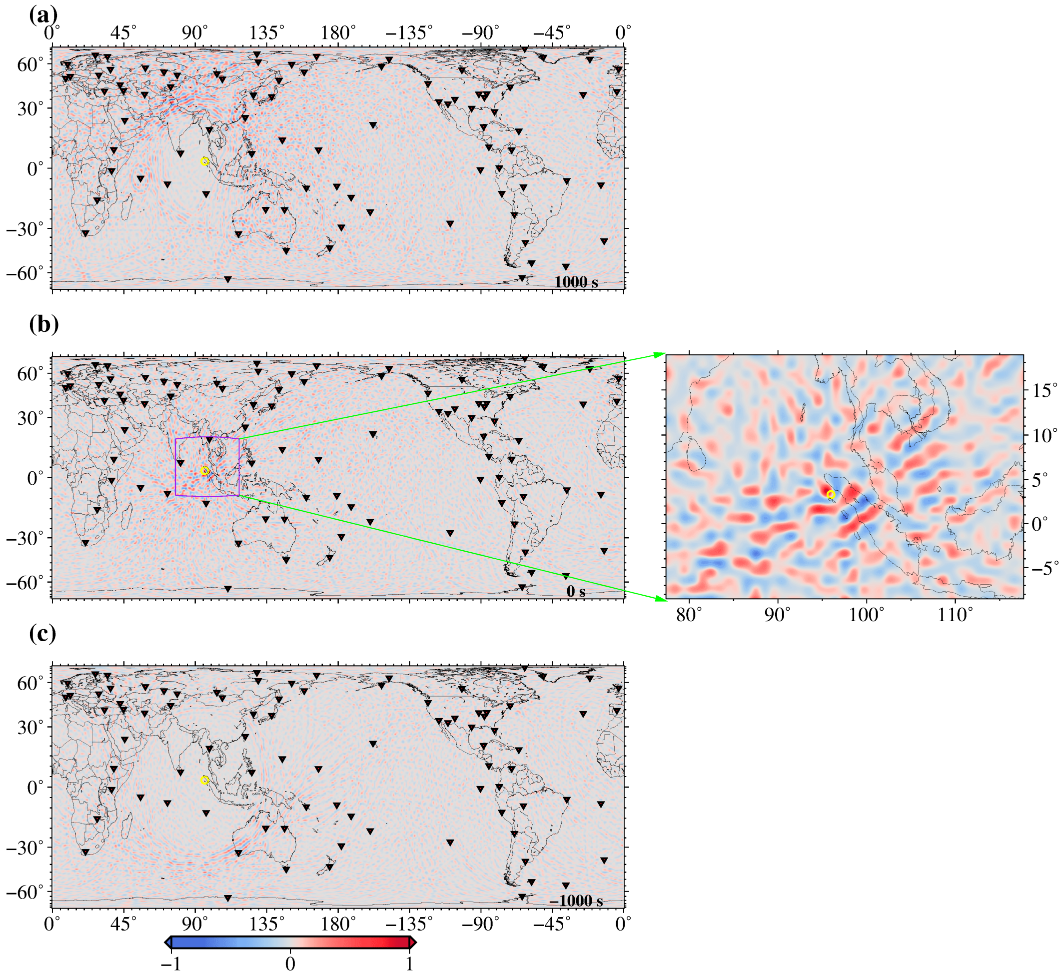

Fig. 2.11 Snapshots of time-reversal simulations using earthquake data recorded by 89 stations, in the 50-to-110s period band. They are selected at the same time as in Fig. 2.10. All symbols are defined as in Fig. 2.10

Fig. 2.2(c) is a simplified illustration of the signal seen in time-reversal experiments: first, the time-reversed wave field that eventually focuses at the source, and then, after focusing has occurred, a spurious arrival that is "emitted" by the time-reversed source, and hits the receiver again. This spurious signal is explained by the fact that the effectiveness of seismic and acoustic time reversal is limited by our inherent lack of knowledge of the source mechanism. Full time reversal of the seismic process would require that, in the reversed-time simulation, the source is replaced by an energy "sink" which absorbs the signal, reversing the rupture process (slip along the fault) itself (Fink, 2006): but such sink cannot be implemented if the slip is unknown.

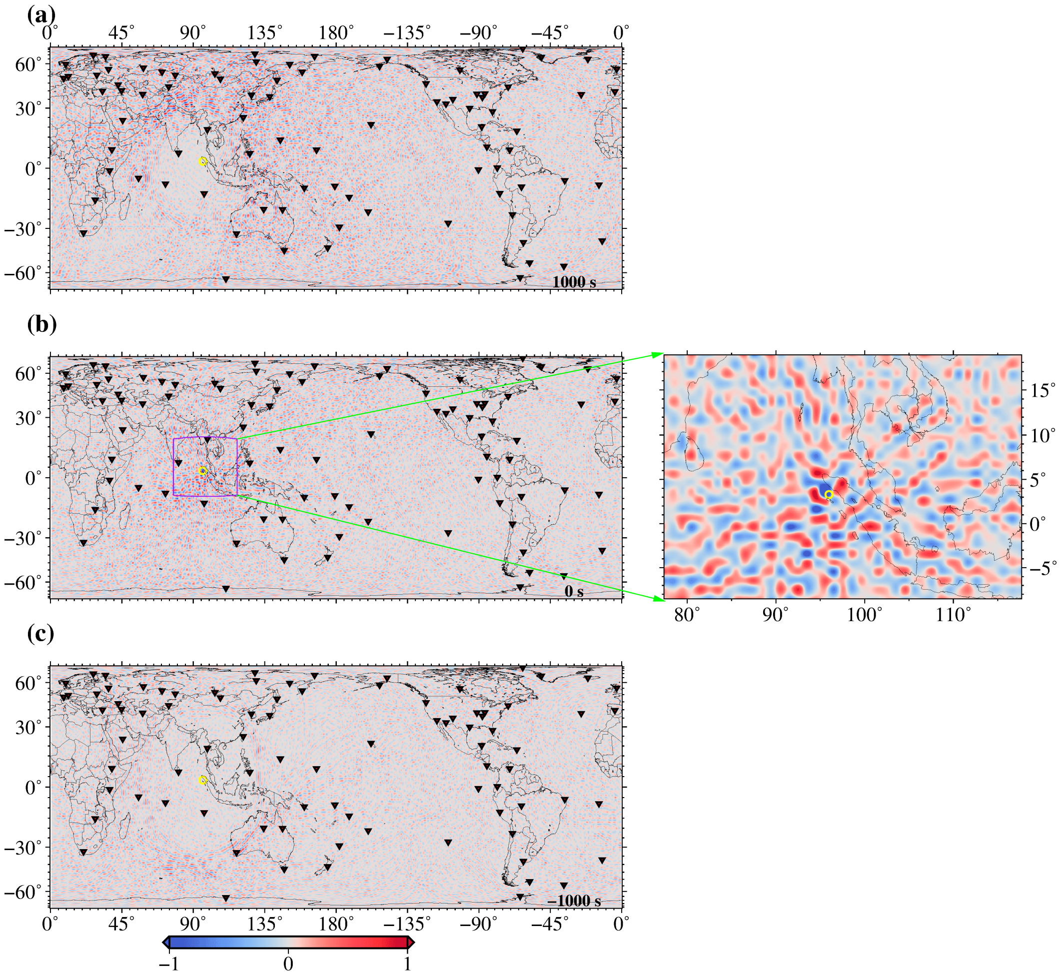

Fig. 2.12 Snapshots of time-reversal simulations using earthquake data recorded by 89 stations, in the 40-to-90 s period band. They are selected at the same time as in Fig. 2.10. All symbols are defined as in Fig. 2.12

2.3 Computational cost

The computational cost of our method is driven by the number of source-receiver pairs and the choice of spatial separation between grid nodes; or, which is the same, the number of grid nodes. Simulations are quite demanding in terms of memory and computational runtime if performed on a single CPU. On the other hand, our scheme is easy to parallelize, as it consists of tracing rays between many source-receiver pairs, and each ray-tracing exercise is naturally independent of all the others.

In order to reduce the computational time, we run our time-reversal simulations on the 1664-CPUs ADA cluster at INGV, Bologna. We perform the entire time reversal simu-

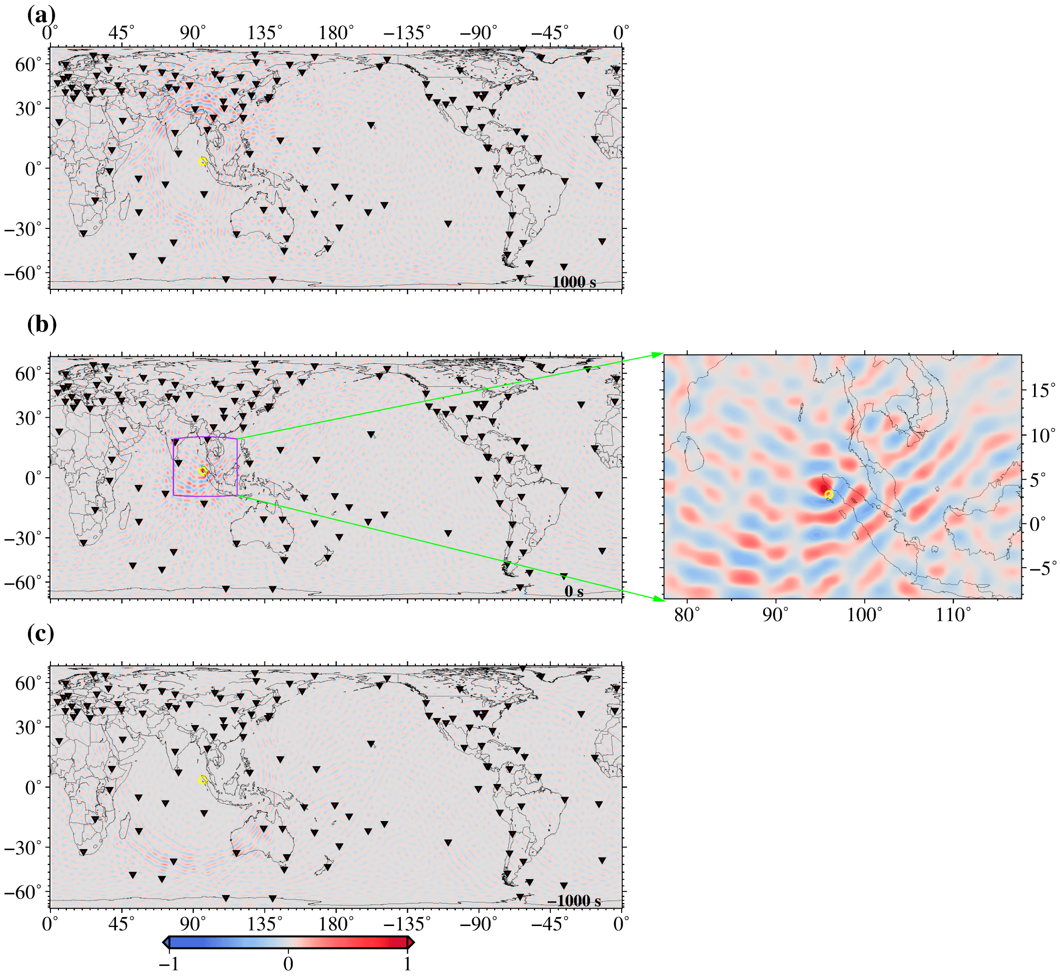

Fig. 2.13 Snapshots of time-reversal simulations using earthquake data, in the 80-to-120s period band using 125 stations. All symbols are defined as in Fig. 2.10.

lation associated with one station on a single CPU and run all one-station time reversals in parallel, so that, for 89 stations we used 89 CPUs. This way, the typical CPU time required to run one simulation, associated with one single frequency band, on the cluster is of the order of 10 hr. This coincides with the time required for full time reversal, as long as we have at least as many available CPUs as time-reversed seismograms (stations).

2.4 Validation of method by synthetic test

We initially applied our method in a synthetic experiment using a 100 s Ricker wavelet (second derivative of a Gaussian wavelet with a source central frequency of 0.01 Hz) as

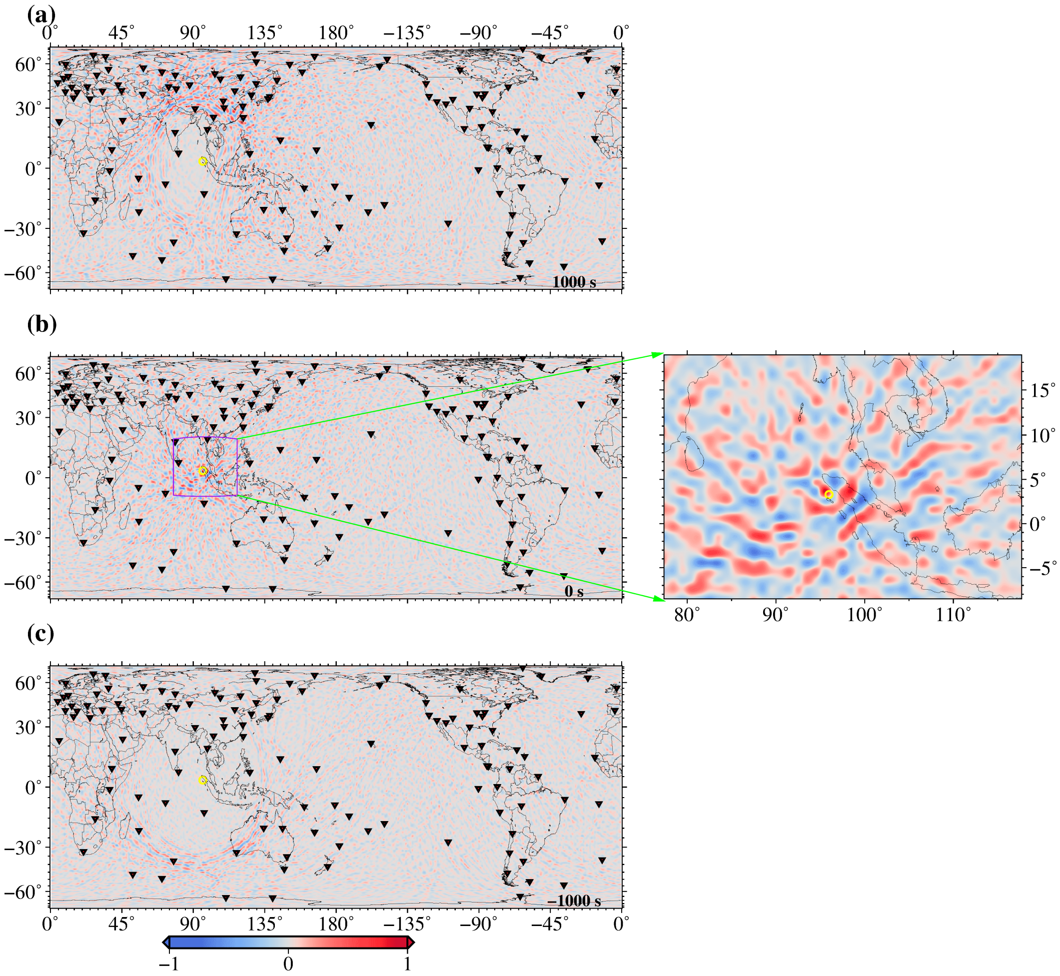

Fig. 2.14 Snapshots of time-reversal simulations using earthquake data, in the 50-to-110 s period band using 125 stations. All symbols are defined as in Fig. 2.10.

source time function. The globe is subdivided into an equal-area grid with $1^\circ \times 1^\circ$ spacing at the equator including 9834 grid nodes. Surface wave ray tracing is implemented as introduced in Section 2.2.1, after performing a least-square fitting via Cholesky factorization (Press et al., 1992) to find the generalized spherical-harmonic coefficients of the phase-velocity map. For any given virtual source (station) and receiver (grid node), we obtain travel-time and distance by tracing the ray between them. Then, we time reverse the recorded signals, and back propagate them with time by implementing eq. (5).

Synthetic data were first computed by propagating waves through the isotropic 100 s Rayleigh-wave phase-velocity map of Trampert and Woodhouse (2003). In the first test, stations were deployed along an equal-epicentral-distance curve (4500 km), equally

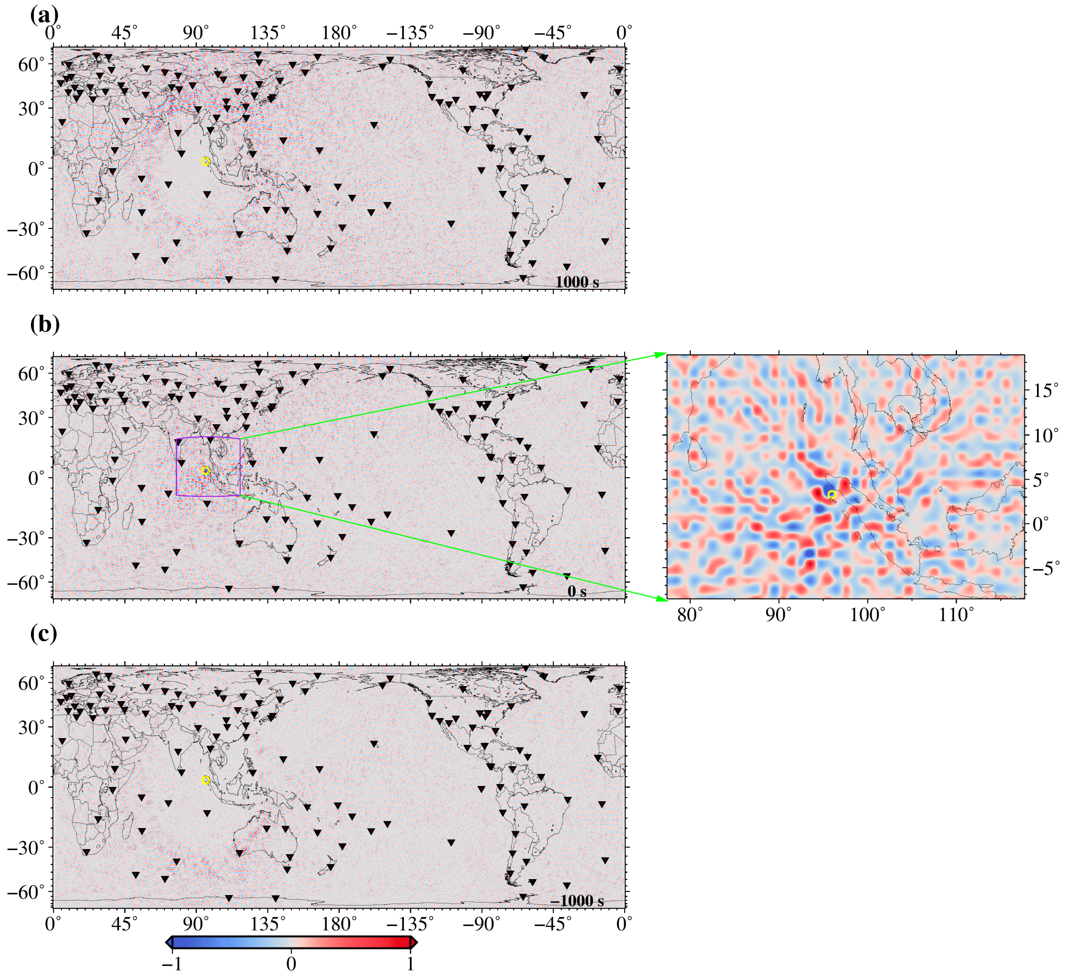

Fig. 2.15 Snapshots of time-reversal simulations using earthquake data, in the 40-to-90 s period band using 125 stations. All symbols are defined as in Fig. 2.10.

spaced from one another. Fig. 2.3(d) shows that the time-reversed wavefield clearly focuses onto the 'input' source location; and, at the moment of focusing, no significant signal is seen away from the source.

In another test, we used synthetics from 89 selected station locations (II and IU networks), distributed as uniformly as possible over the globe. We show in Fig. 2.4 some snapshots of our time-reversal simulations. The reconstructed signal at the location of source is shown in Fig. 2.6 and the time-reversed wavefield focuses correctly at the expected location and origin time of the signal (Fig. 2.4(b)). In this case, however, the non-uniformity in station distribution results in significant non-zero time-reversed energy away (but not very far) from the source. Its pattern is determined by the interference between time-reversed wave fronts emitted by the different stations.

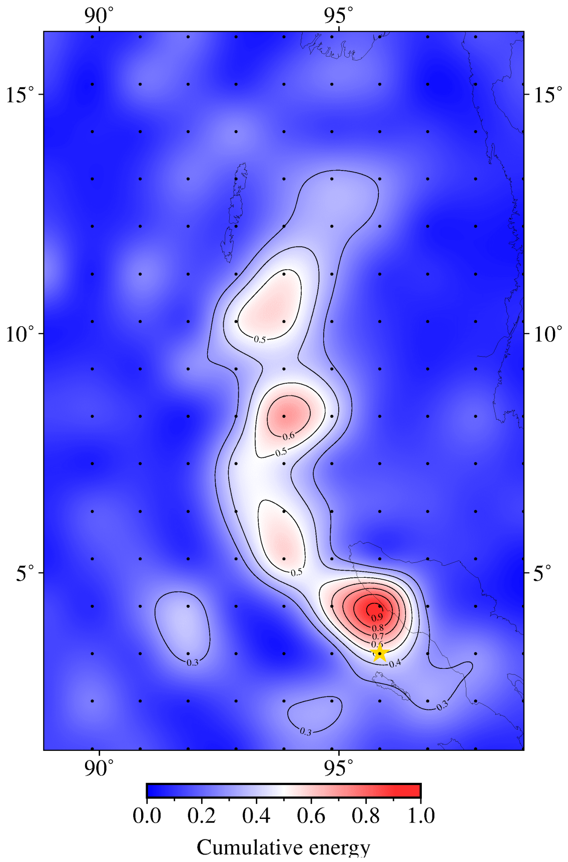

Fig. 2.16 Proxy $E_j(t)$ for seismic energy defined by eq. 7 with t = 600 s, computed from data band-pass filtered between 80 and 120s (as in Fig. 2.10). E_j is normalized to 1 and plotted only in the area where it is large, coinciding with the source region of the Sumatra event. The epicenter is denoted by a yellow star. The black contours are plotted at increments of 0.1.

In order to test how the accuracy of the velocity model is important for the convergence of the method, we performed another test where we time-reversed and backpropagated the same synthetics as above, in a model that involved no lateral heterogeneity, that is, 100 s Rayleigh-wave phase velocity is constant and equal to 4 km/s . The time-reversed wavefield in Fig. 2.5 focuses at the location 247 km away from the correct source location. Fig. 5(e) shows the difference between the two cases: with and without the velocity model, that is, Figs 2.4(b) and 2.5(b). The main peak during the focusing is not as sharp as when a realistic, heterogeneous phase velocity model is used to backpropagate the synthetics as shown in Fig. 2.6.

A set of synthetic data was next computed based on Trampert and Woodhouse (2003)

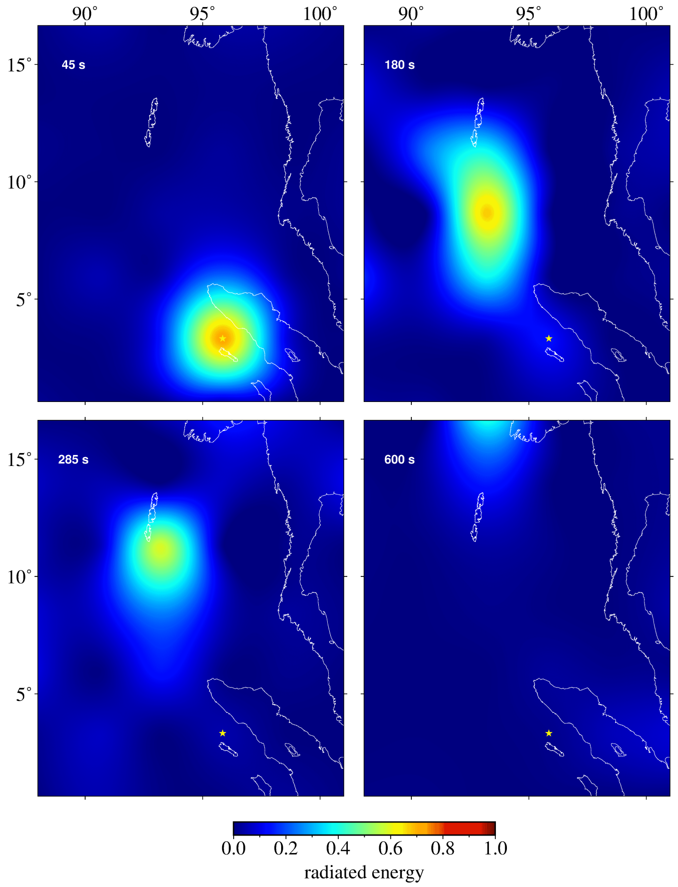

Fig. 2.17 Rupture progression. The distribution of energy radiation at different time intervals. The rupture starts just west of northern Sumatra and advances in a northward direction all the way to Andaman Islands.

azimuthally anisotropic map of 100s Rayleigh-wave velocity, neglecting the 4ζ term in eq. 1, and keeping the 2ζ and isotropic terms only. Fig. 2.7 shows some snapshots of our simulation. This new set of synthetics was then time-reversed and back propagated twice: first in the same, anisotropic model used to compute them, and then in the isotropic model used earlier. The time-reversed wave fields so obtained are very similar, and differences in the mapped source area are minor. "Anisotropic" time reversal of synthetics that contain anisotropy results in an excellent fit of the trace recorded at the source with the source time function while "isotropic" time reversal of the same synthetic results in a 1s error in focusing time (Fig. 2.8), but an essentially equivalent spatial distribution of the time-reversed signal as shown in Fig. 2.7. Thus, in the following, for the sake of simplicity, we only account for isotropic velocity heterogeneity in all our simulations.

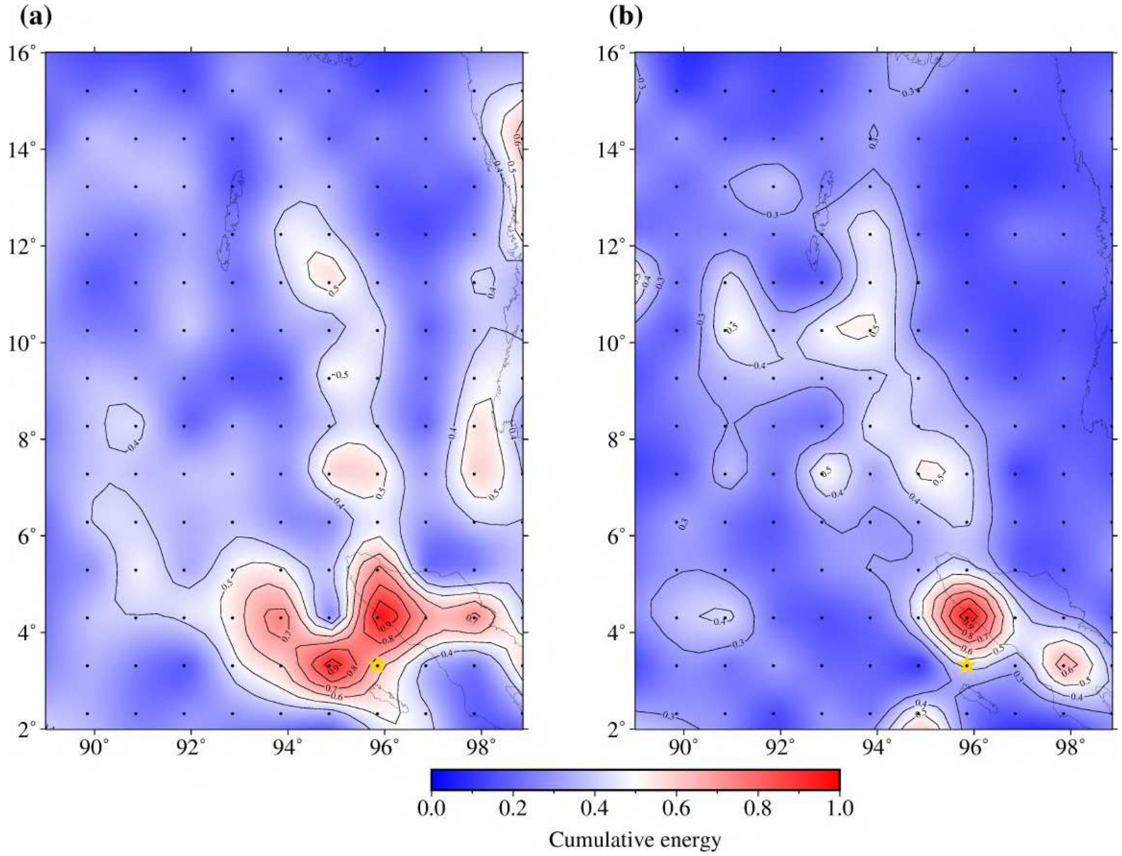

Fig. 2.18 Integrated energy over 600 s after initiation of the earthquake obtained time-reversing seismograms bandpass filtered between (a) 40-to-90 s and (b) 50-to-110 s.

2.5 Application to Earthquake data

We apply our surface wave ray-tracing and time-reversal algorithm to recordings of the 2004 December 26, Sumatra-Andaman Earthquake, Mw = 9.3, 00:58:53. Being one of the largest and most studied earthquakes of all times, we use it as an ideal test case for our method because of its large energy release and to compare our results with those obtained by using other techniques.

First, 89 seismograms were downloaded from the IRIS/USGS Global Seismographic Network (GSN, Fig. 2.10, black triangle) (USGS, 1988; Scripps Institution of Oceanography, 1986), which we selected because of the relative spatial uniformity in station distribution. Next, we further increased the number of stations from 89 to 125, including data from IC (Albuquerque Seismological Laboratory (ASL)/USGS, 1992), MN (MedNet Project Partner Institutions, 1990) and G (GEOSCOPE, 1982) networks (Fig.

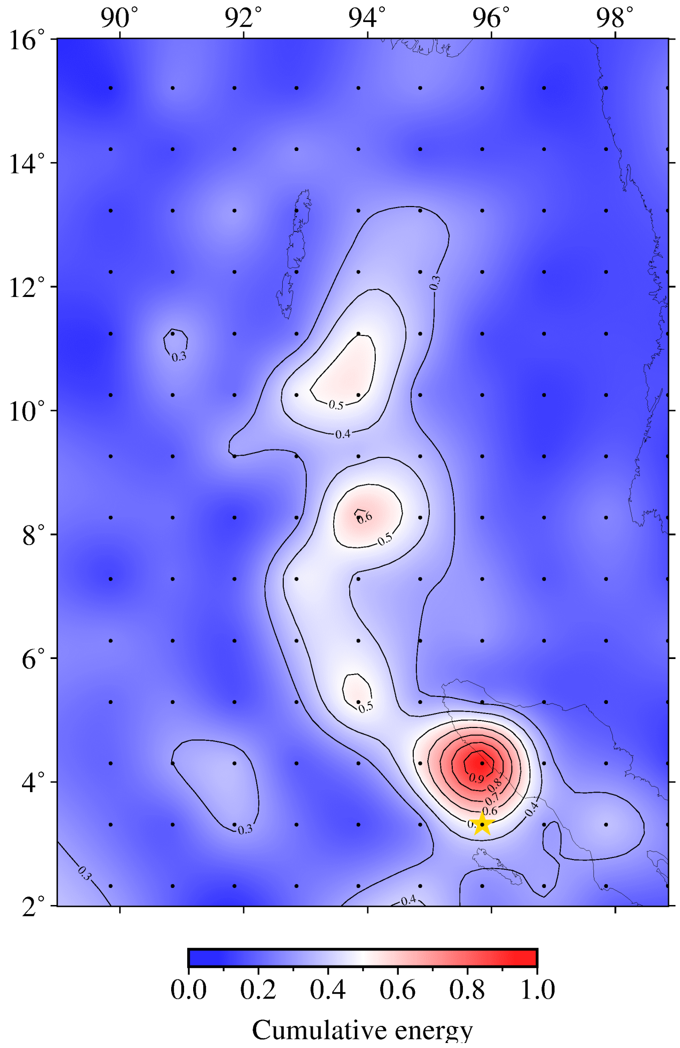

Fig. 2.19 Cumulative energy radiation obtained by averaging results from time reversal in all three passbands.

2.13). This way we verified whether our result varies with station coverage.

We removed the instrumental response for each trace, and apply a 80-to-120 s band-pass filter. Filtered data are shown in Fig. 2.9. We next apply the procedure described in Section 4. The heterogeneous phase velocity model for Rayleigh waves at 100 s is taken from Trampert and Woodhouse (2003). We find that the backward propagating wavefield focuses on the expected source location. We show in Fig. 2.10 snapshots of time-reversed wavefield. Fig. 2.10(b) shows the maximum focusing at 3.31°N and 95.85°E that corresponds to the USGS estimate of 3.316°N and 95.854°E. We repeat surface wave ray-tracing and time reversal simulation in the 40-to-90 and 50-to-110 s bands and show the results in Figs 2.11 and 2.12. Again, phase velocity maps at 60 and 80 s are taken from Trampert and Woodhouse (2003). The accuracy of source localization appears to be slightly decreased with a significant reduction in the width of the passband. Further, we increase the number of stations to 125 and then perform the time-reversal simulation for all those three bands. The results are consistent with those of the 89-station simulations as shown in Figs 2.13, 2.14 and 2.15 for 80-to-120, 40-to-90 and 50-to-110 s respectively, with sharpest focusing at the epicenter achieved in the respective band.

We next squared the time-reversed trace (80-to-120 s), then integrate it over time to obtain a proxy for the energy propagating through grid point j at time t,

$$E_j(t) = \frac{1}{t}\int_0^t a_j^2(t)dt \tag{7}$$

where $a_j(t)$ is the amplitude of the time-reversed signal at grid node j and time t.

Because the signal a_j is a displacement, it is understood that E_j is not strictly energy. Still, its distribution in time and space should be very closely related to that of energy, at least at the scale length that is of interest here. We therefore integrate ${a_j}^2(t)$ over 600 s after the initiation of the earthquake (Fig. 2.16) to obtain a rough estimate of the relative strength of total energy released as a function of location. We show in Fig. 2.17 how $E_j(t)$ varies with t over the grid and observe the migration of rupture from south towards the north with rupture lasting nearly 600 s after initiation of the earthquake. The plotted area is limited to the only part of the globe where an important amount of energy accumulates. Time in Fig. 2.17 is measured after initiation of the earthquake. We found the strongest energy radiation in the southern portion, to the west of the northern Sumatra, followed by a second important radiation to the north of the Nicobar Island, as depicted in Fig. 2.17.

Finally, we apply the same procedure of time-reversal in the 40-to-90 s, 50-to-110 s passbands. The results are shown in Fig. 2.18. We average the energy radiation estimates obtained from the time reversal simulation at 40-to-90 s, 50-to-110 s and 80-to-120 s passbands, and show it in Fig. 2.19. This confirms our earlier result, with large energy emission in two regions. In summary, our results are in good agreement with the conclusion drawn by Ishii et al. (2005, fig. 4), Krüger and Ohrnberger (2005, fig. 3) and Larmat et al. (2006) about the slip distribution and the migration of rupture in an unilateral direction from south towards the north.

2.6 Summary and Conclusions

We treat narrow-frequency band surface wave signals as membrane waves, which we model via ray tracing on the sphere similar to Boschi and Woodhouse (2006), thus reducing the computational weight of numerical simulations. Our surface wave ray-tracing algorithm is based on the generalized spherical harmonic parametrization, and the time reversal method is used to reconstruct the surface wavefield in the immediate vicinity of the source region. As an example, the spatial distribution of energy radiation from the 2004 Sumatra earthquake is estimated via our method. By comparison with independent studies based on different data and techniques, we infer that our method is successful in mapping the source of the earthquake in both space and time, tracing its direction of rupture propagation and locating areas where most energy is released. Specifically, our results are in good agreement with existing finite-source models of the events (Ammon et al., 2005; Banerjee et al., 2005; Ni et al., 2005; Bletery et al., 2016). In all those models, most energy release occurs to the northwest of the Sumatra Island and near the Nicobar Island.

This study encourages further application of our method, in particular to the 3-D mapping of seismic faults, both in space and time. This will require the calculation of time reversal at a dense suite of surface wave modes, and their combination, with account of respective depth sensitivities. It will be the topic of future work. As discussed in many other studies (e.g., Fink, 2006; Boschi et al., 2018), the time-reversed wavefield includes a non-physical contribution, that is, a signal that propagates away from the source after focusing, cannot be easily removed. For this non-physical effect to disappear, the source process itself should be modelled, introducing a time reversed forcing term referred to as ‘sink’. This issue will be addressed in future work.

References

Albuquerque Seismological Laboratory (ASL)/USGS (1992), ‘New china digital seismograph network’.
URL: *https://www.fdsn.org/networks/detail/IC/*

Ammon, C. J., Ji, C., Thio, H.-K., Robinson, D., Ni, S., Hjorleifsdottir, V., Kanamori, H., Lay, T., Das, S., Helmberger, D. et al. (2005), ‘Rupture process of the 2004 sumatra-andaman earthquake’, *science* **308**(5725), 1133–1139.

Banerjee, P., Pollitz, F. F. and Burgmann, R. (2005), ‘The size and duration of the sumatra-andaman earthquake from far-field static offsets’, *Science* **308**(5729), 1769–1772.

Bletery, Q., Sladen, A., Jiang, J. and Simons, M. (2016), ‘A bayesian source model for the 2004 great sumatra-andaman earthquake’, *Journal of Geophysical Research: Solid Earth* **121**(7), 5116–5135.

Boschi, L., Molinari, I. and Reinwald, M. (2018), ‘A simple method for earthquake location by surface-wave time reversal’, *Geophysical Journal International* **215**(1), 1–21.

Boschi, L. and Weemstra, C. (2015), ‘Stationary-phase integrals in the cross correlation of ambient noise’, *Reviews of Geophysics* **53**(2), 411–451.

Boschi, L. and Woodhouse, J. H. (2006), ‘Surface wave ray tracing and azimuthal anisotropy: a generalized spherical harmonic approach’, *Geophysical Journal International* **164**(3), 569–578.

Catherine, J. K., Gahalaut, V. K. and Sahu, V. K. (2005), ‘Constraints on rupture of the december 26, 2004, sumatra earthquake from far-field gps observations’, *Earth and Planetary Science Letters* **237**(3-4), 673–679.

Ekström, G., Tromp, J. and Larson, E. W. (1997), ‘Measurements and global models of surface wave propagation', *Journal of Geophysical Research: Solid Earth* **102**(B4), 8137–8157.

Fink, M. (1999), 'Time-reversed acoustics', *Scientific American* **281**(5), 91–97.

Fink, M. (2006), 'Time-reversal acoustics in complex environments', *geophysics* **71**(4), SI151–SI164.

Fink, M., Montaldo, G. and Tanter, M. (2003), 'Time-reversal acoustics in biomedical engineering', *Annual review of biomedical engineering* **5**(1), 465–497.

GEOSCOPE (1982), 'Geoscope, french global network of broad band seismic stations'. **URL:** *http://geoscope.ipgp.fr/networks/detail/G/*

Guilbert, J., Vergoz, J., Schisselé, E., Roueff, A. and Cansi, Y. (2005), 'Use of hydroacoustic and seismic arrays to observe rupture propagation and source extent of the mw= 9.0 sumatra earthquake', *Geophysical research letters* **32**(15).

Hashimoto, M., Choosakul, N., Hashizume, M., Takemoto, S., Takiguchi, H., Fukuda, Y. and Fujimori, K. (2006), 'Crustal deformations associated with the great sumatra-andaman earthquake deduced from continuous gps observation', *Earth, planets and space* **58**(2), 127–139.

Ishii, M., Shearer, P. M., Houston, H. and Vidale, J. E. (2005), 'Extent, duration and speed of the 2004 sumatra–andaman earthquake imaged by the hi-net array', *Nature* **435**(7044), 933–936.

Jaffe, B. E., Borrero, J. C., Prasetya, G. S., Peters, R., McAdoo, B., Gelfenbaum, G., Morton, R., Ruggiero, P., Higman, B., Dengler, L. et al. (2006), 'Northwest sumatra and offshore islands field survey after the december 2004 indian ocean tsunami', *Earthquake Spectra* **22**(3_suppl), 105–135.

Krüger, F. and Ohrnberger, M. (2005), 'Tracking the rupture of the mw= 9.3 sumatra earthquake over 1,150 km at teleseismic distance', *Nature* **435**(7044), 937–939.

Larmat, C., Montagner, J.-P., Fink, M., Capdeville, Y., Tourin, A. and Clévédé, E. (2006), 'Time-reversal imaging of seismic sources and application to the great sumatra earthquake', *Geophysical Research Letters* **33**(19).

Larmat, C., Tromp, J., Liu, Q. and Montagner, J.-P. (2008), 'Time reversal location of glacial earthquakes', *Journal of Geophysical Research: Solid Earth* **113**(B9).

Larson, E. W., Tromp, J. and Ekström, G. (1998), 'Effects of slight anisotropy on surface waves', *Geophysical Journal International* **132**(3), 654–666.

Lay, T., Kanamori, H., Ammon, C. J., Nettles, M., Ward, S. N., Aster, R. C., Beck, S. L., Bilek, S. L., Brudzinski, M. R., Butler, R. et al. (2005), 'The great sumatra-andaman earthquake of 26 december 2004', *Science* **308**(5725), 1127–1133.

Lomax, A. (2005), 'Rapid estimation of rupture extent for large earthquakes: Application to the 2004, m9 sumatra-andaman mega-thrust', *Geophysical research letters* **32**(10).

Mai, P. M., Schorlemmer, D., Page, M., Ampuero, J.-P., Asano, K., Causse, M., Custodio, S., Fan, W., Festa, G., Galis, M. et al. (2016), 'The earthquake-source inversion validation (siv) project', *Seismological Research Letters* **87**(3), 690–708.

MedNet Project Partner Institutions (1990), 'Mediterranean very broadband seismographic network (mednet)', *Istituto Nazionale di Geofisica e Vulcanologia (INGV)* .

Merrifield, M., Firing, Y., Aarup, T., Agricole, W., Brundrit, G., Chang-Seng, D., Farre, R., Kilonsky, B., Knight, W., Kong, L. et al. (2005), 'Tide gauge observations of the indian ocean tsunami, december 26, 2004', *Geophysical Research Letters* **32**(9).

Ni, S., Kanamori, H. and Helmberger, D. (2005), 'Energy radiation from the sumatra earthquake', *Nature* **434**(7033), 582–582.

Peter, D., Boschi, L. and Woodhouse, J. (2009), 'Tomographic resolution of ray and finite-frequency methods: a membrane-wave investigation', *Geophysical Journal International* **177**(2), 624–638.

Peter, D., Tape, C., Boschi, L. and Woodhouse, J. H. (2007), ‘Surface wave tomography: global membrane waves and adjoint methods’, *Geophysical Journal International* **171**(3), 1098–1117.

Press, W. H., Vetterling, W. T., Teukolsky, S. A. and Flannery, B. P. (1992), *Numerical Recipes Example Book (FORTRAN)*, Cambridge University Press Cambridge.

Rietbrock, A. and Scherbaum, F. (1994), ‘Acoustic imaging of earthquake sources from the chalfant valley, 1986, aftershock series’, *Geophysical Journal International* **119**(1), 260–268.

Roten, D., Miyake, H. and Koketsu, K. (2012), ‘A rayleigh wave back-projection method applied to the 2011 tohoku earthquake’, *Geophysical Research Letters* **39**(2).

Scripps Institution of Oceanography (1986), ‘Iris/ida seismic network’, *International Federation of Digital Seismograph Networks* .

Smith, M. L. and Dahlen, F. (1973), ‘The azimuthal dependence of love and rayleigh wave propagation in a slightly anisotropic medium’, *Journal of Geophysical Research* **78**(17), 3321–3333.

Smith, M. L. and Dahlen, F. (1975), ‘Correction [to “‘the azimuthal dependence of love and rayleigh wave propagation in a slightly anisotropic medium’by martin l. smith and fa dahlen”]’, *Journal of Geophysical Research* **80**(14), 1923–1923.

Tanimoto, T. (1990), ‘Modelling curved surface wave paths: membrane surface wave synthetics’, *Geophysical Journal International* **102**(1), 89–100.

Tanimoto, T. and Anderson, D. L. (1985), ‘Lateral heterogeneity and azimuthal anisotropy of the upper mantle: Love and rayleigh waves 100–250 s’, *Journal of Geophysical Research: Solid Earth* **90**(B2), 1842–1858.

Trampert, J. and Woodhouse, J. H. (2003), ‘Global anisotropic phase velocity maps for fundamental mode surface waves between 40 and 150 s’, *Geophysical Journal International* **154**(1), 154–165.

Tromp, J. and Dahlen, F. (1993), ‘Variational principles for surface wave propagation on a laterally heterogeneous earth—iii. potential representation’, *Geophysical Journal International* **112**(2), 195–209.

USGS, A. (1988), ‘Global seismograph network (gsn-iris/usgs): International federation of digital seismograph networks’.

Vigny, C., Simons, W., Abu, S., Bamphenyu, R., Satirapod, C., Choosakul, N., Subarya, C., Socquet, A., Omar, K., Abidin, H. et al. (2005), ‘Insight into the 2004 sumatra–andaman earthquake from gps measurements in southeast asia’, *Nature* **436**(7048), 201–206.

Yao, H., Gerstoft, P., Shearer, P. M. and Mecklenbräuker, C. (2011), ‘Compressive sensing of the tohoku-oki mw 9.0 earthquake: Frequency-dependent rupture modes’, *Geophysical Research Letters* **38**(20).

CHAPTER 3

Imaging of seismic sources by surface-wave time-reversal: very long-period earthquakes

Apsara Sharma Dhakal[1], *Lapo Boschi*[1,2,3], *Simone Cesca*[4]

(submitted to Geophys. J. Int.)

1 2 3 4

ABSTRACT

The study of very long-period events in volcanic settings is of fundamental importance to better understand the physics of volcanic plumbing systems. We locate long-duration, very long period events in Mayotte, Comoro Islands, using a source-imaging method developed recently, and previously validated by application to large earthquakes. Our approach combines seismic time-reversal with a surface-wave ray tracing algorithm based on generalized spherical-harmonic parameterization of surface-wave phase velocity, and accounting for azimuthal anisotropy. This new application focuses on different, very low-frequency signals recorded at regional to teleseismic distances, which have been attributed to the drainage and resonance of a deep magma reservoir. We first conduct synthetic tests to quantify the resolving power of our method, given the available data coverage for the events of interest. We then use low-frequency Rayleigh-wave signals recorded by different stations, reverse them in time and back propagate them through a surface-wave phase-velocity model. The time-reversed wave field has a prominent maximum at the spatial location(s) and time(s) where and when the recorded signal had been generated. From the time- and space-distribution of such maximum,

---

[1] Departimento Di Geoscienze, Università Degli Studi di 35131, Padova, Italy

[2] Istituto Nazionale di Geofisica e Vulcanologia, Sezioni di, 40128, Bologna, Italy

[3] Institut des sciences de la terre paris sorbonne université, CNRS-ISU, ISTeP UMR 7193, F-75005, Paris, France

[4] GFZ German Research Centre for Geosciences, 14473 Potsdam, Germany

we can make inferences on the nature of the source. Our results are in good agreement with centroid locations by moment tensor inversion. We show that our methodology is applicable to volcanic settings, possibly providing new insights into the nature of very long-period seismic sources related to volcanic activity. A precise location of such events helps constraining the depth, size and geometry of the seismogenic volume.

Keywords: *Very long-period signal*, *Mayotte Island*, *Seismic Time-reversal*, *surface-wave ray tracing*

3.1 Introduction

Volcano seismicity produces volcanic signals at frequencies ranging from zero to several tens of Hz, which includes volcanic tremors, long period (LP), very long period (VLP) and volcano-tectonic or high-frequency earthquakes (Chouet, 1996; McNutt, 2005; Wassermann, 2012; Bean et al., 2014; Montesinos et al., 2021). LP events and volcanic tremors share the same spectral components, they differ in duration. The former events are short (seconds) whereas the latter can last from few minutes to hours, days, or even months. The study of VLP events can provide information on the temporal variation of the physical properties of magma, as well as the geometry of a plumbing system.

It is a challenging task to locate such events in a volcanic setup, because volcanoes are very heterogeneous structures, due to their magmatic dynamics and to the accumulation of different materials from successive eruptions. Furthermore, these seismic signals may be the result of low-cohesion volcaniclastic sediments (Rowley et al., 2021) or long-lasting resonance or multiple excitations along spatially extended structures. From the point of view of seismology, this might translate into a lack of recognizable direct P and/or S phases, unclear onsets, and ringing.

As computational power continues to grow, different approaches have been introduced to address this issue, including the combination of cross correlation between recording stations and triangulation (Obara, 2002), relocation (Shelly et al., 2006), full-waveform inversion (Ohminato et al., 1998; Legrand et al., 2000; Lokmer et al., 2007), amplitude decay (Battaglia et al., 2003; Battaglia and Aki, 2003; Kumagai et al., 2011; Morioka et al., 2017; Gaete et al., 2019), polarization-based methods (Del Pezzo and Patané, 1992; Saccorotti et al., 2007; Cesca et al., 2008; Gaete et al., 2019), coherence-analysis of the characteristic function (Kao and Shan, 2004; Grigoli et al., 2013, 2014; Gaete et al., 2019), cross-correlation (De Barros et al., 2009; Matoza et al., 2013, 2014) and particle motion analysis (Metaxian et al., 2002; Almendros et al., 2002). Despite all this progress, it seems that more work is still needed to identify a robust, consensual approach to source inversion in the volcano-seismology context.

So-called acoustic time reversal (Fink, 1999, 2006; Fink et al., 2003), which was originally applied, e.g., in the contexts of medical imaging, communication and non-destructive testing, has also been employed to localize sources of mechanical waves (earthquakes), in laboratory experiments and based on real-world seismology data (Larmat et al., 2006, 2008; Anderson et al., 2008; Griffa et al., 2008; Sharma Dhakal et al., 2023). Some authors were also successful in using this approach to locate volcanic and non-volcanic tremors (Lokmer et al., 2009; Larmat et al., 2009).

The method used in this study has been described and validated in Sharma Dhakal et al. (2023); it includes the calculation of surface wave ray paths on a spherical earth accounting for laterally varying azimuthal anisotropy. Our method is restricted to surface-wave data which are approximated as membrane waves and modeled via ray tracing.

The present study focuses on the volcano-tectonic crisis in the Comoro Islands, which started in 2018 offshore the island of Mayotte (Cesca et al., 2020; Lemoine et al., 2020). The volcano-tectonic seismic sequence, driven by a large magma intrusion, was accompanied by long duration VLP signals, recorded up to thousand kilometers distance (Cesca et al., 2020). It is difficult to locate such VLP events due to the lack of clear signal onsets, and/or seismic phases. We thus investigate the potential of our method to infer their source location and radiation pattern.

3.2 Study Area

Mayotte is a “territorial collectivity” of France, situated 300 km northwest of Madagascar and 450 km off the east African coast. It is a volcanic island, with a land area of 374 km^2, and home to 299,348 (2022) population. Volcanic activity is supposed to have started around 10-20 Ma (Pelleter et al., 2014; Michon, 2016); recently reported volcanic events occurred within a few thousand years in the eastern part of Mayotte (Zinke et al., 2003). Around 265 km of its coastline consists of cliffs that separate variably embayed tiny beaches of sand and sandy mud. The area has been affected by a number of tectonic events, including a NE-SW-trending rifting episode that occurred during the Permo-Triassic (Scrutton et al., 1981). About 407 VLP signals and 7,000 VT earthquakes were recorded in between January 2018 and May 2019 (Cesca et al., 2020). The largest event ever recorded in this region (5.9 M_w) occurred during this sequence, on May 15, 2018, (Lemoine et al., 2020; Cesca et al., 2020).

3.3 Synthetic experiment

We conducted a synthetic test to quantify the resolving power of our method. The test reproduces the real-world data coverage for the events of interest, and relies on the available, real surface-wave phase-velocity models. We first subdivided the globe into an equal-area grid, with spacing of 0.5° X 0.5°. Overall, 259,920 grid nodes were used. A Ricker wavelet with 35 s dominant period was used as a source time function. Accordingly, Rayleigh wave propagation was modeled based on the isotropic 35 s Rayleigh-wave phase-velocity map of Ekström (2011). Synthetic seismograms were computed at 44 hypothetical station locations, uniformly distributed over the globe.

First, we trace Rayleigh-wave rays, and calculate Rayleigh-wave phase as described in Boschi and Woodhouse (2006), for each virtual source (station) and receiver (grid node) (Sharma Dhakal et al., 2023). Next, we time-reverse the computed synthetics and back-propagate them through the same phase-velocity map used to model them. Snapshots of the reversed wavefield at few, selected times are shown in Fig. 3.1. Fig. 3.2 shows the reconstructed signal, as a function of time, at the known location of the source. We find that the amplitude of the time-reversed, back-propagated field is highest at the known time and location of the initial source (Fig. 3.1(b)). We also find that, at that location, the recorded signal approximately coincides with the known theoretical signal emitted by the source (Fig. 3.2). All this confirms the reliability of our method, even though only a relatively small number of non-uniformly distributed stations were employed.

The fact that non-physical signal continues to exist in the time-reversed, back-propagated wave field (Fig. 3.1c) reflects a known limit of acoustic and seismic time-reversal that has been discussed previously (e.g., Boschi et al., 2018), i.e., the absence of an energy "sink" in the time-reversed simulation. This will be addressed in future work.

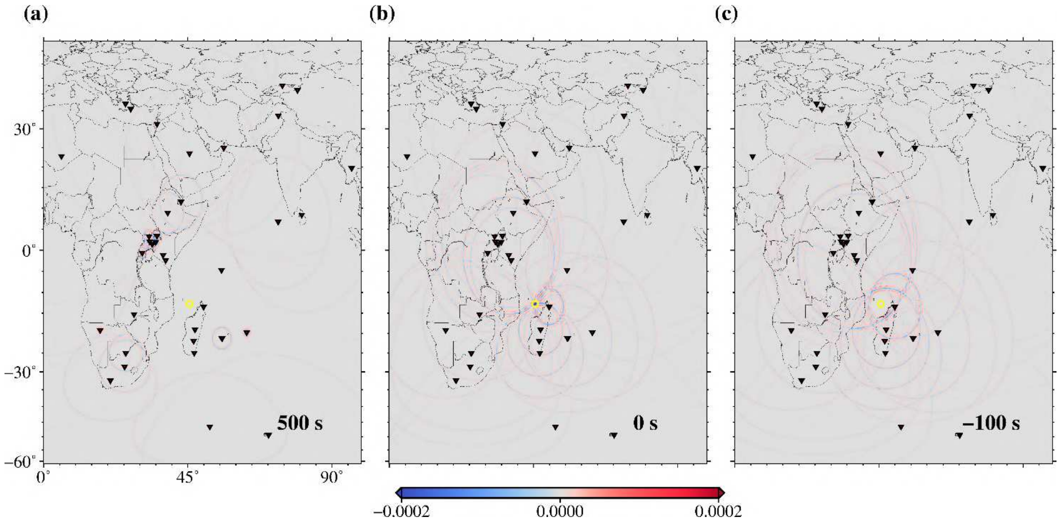

Fig. 3.1 Snapshots of the time-reversed simulation at (left to right) 500, 0 and -100s. Positive and negative time correspond to the time before and after focusing of wave field in the source location. Respectively (i.e., the time-reversed simulations start at positive time and ends at negative time). Time t=0 s represents the origin time of the "input" source – a 35 s Ricker wavelet. Black triangles and the yellow circle represent station and source locations, respectively.

3.4 The large VLP event of November 11, 2018

A sequence of earthquakes was recorded over a period of one year followed by larger event of 5.9 magnitude on 15 May 2018 near Mayotte island. Further, a long-lasting VLP event was detected in November 2018 with dominant period of ∼16 s, and other VLPs were detected over a period of few months (Cesca et al., 2020; Lemoine et al., 2020). In this study, we apply our method to the 44 vertical component recordings ex-

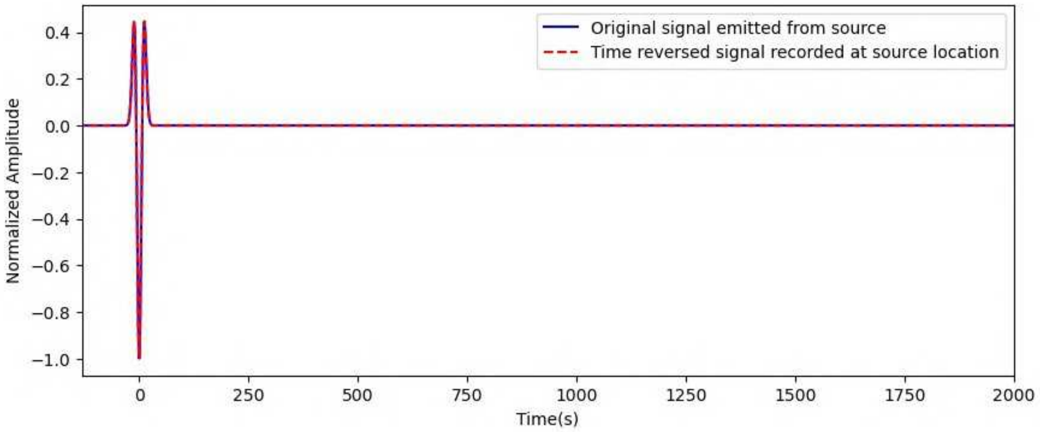

Fig. 3.2 Normalized, time-reversed, back propagated displacement (red dashed curve) modeled at the source location. This signal overlaps very well with the originally emitted signal (blue solid curve).

tracted from 2018 June to 2018 November, in order to locate the VLP events.

First, we took the vertical component of the displacement of seismograms (Fig. 3.3) from one of the largest VLP events (the one recorded on November 11, 2018, with an estimated-surface wave magnitude of M_s 5.1, and which has been linked with the deflation of the main magmatic reservoir reservoir (Cesca et al., 2020; Lemoine et al., 2020)) and pre-process the data as follows. After removing the instrumental response, we eliminate any existing gaps in the traces by zero-padding; we, taper the beginning and end of seismograms to reduce the effect of noise; we resample each trace to match the time step used in the back-propagation method. Then, each trace is band-pass filtered in the 20-40s, 20-60s, 20-100s and 20-140s period bands. We trace Rayleigh-wave ray paths on a heterogeneous phase velocity model from Ekström (2011), specifically the 35s, 40s, 60s and 80s, approximately corresponding to the four period bands of interest. Traces are reversed in time and backpropagated through the same maps. Fig. 3.4(b) show that the amplitude of the time-reversed, back-propagated wavefield is maximum at 45.5°E, 12.7°S, which coincides with the location of the VLP event as reported by Cesca et al.(2020) (i.e., precisely at 45.50°E, 12.75°S).

Fig. 3.4 confirms our expectations, based on earlier applications by Boschi et al. (2018) and Sharma Dhakal et al. (2023). It shows, first of all, that the time-reversed

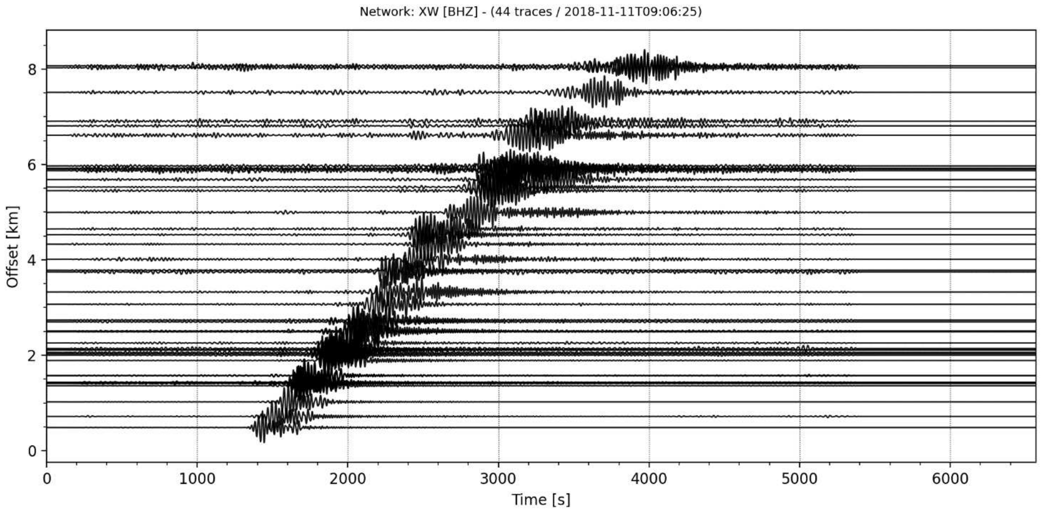

Fig. 3.3 Normalized vertical-component seismograms of 2018 November 11 VLP event, filtered in the period bands 20-40s.

back-propagated converges to a prominent maximum at the expected original source location. Also, non-physical signal appears after focusing, as anticipated above and shown in Fig. 3.1. Fig. 3.5 shows our estimate of the signal as it is emitted by the source. It has a duration of 1000s, and this is very close to the duration estimated independently by Cesca et al. (2020) ($\sim$20 min).

We repeat our time reversal simulation in the 20-60 s period band, so as to reconstruct the seismic source. Its location is found to be approximately same as in the previous (20-40s) simulation, confirming that our results are not strongly dependent on the frequency band. Moreover, the time-reversed, backpropagated signals calculated at the source location is also similar with the ones obtained in the 20-40s period band (Fig. 3.5). We determine a rough estimate of the spatial distribution of released energy by squaring, at each location, the time-reversed, back-propagated traces for each band and integrating them over time after initiation of the event to 20s. The results of this exercise are illustrated in Fig. 3.6, which shows that most energy is released in the vicinity, and slightly to the east-northeast, of the previously estimated location. We explain the (non-physical) ringing that characterizes Fig. 3.6 in terms of constructive interference of time-reversed wave-field, which is almost monochromatic: this is a limitation of our method, that can be mitigated by combining signals at different periods. This VLP event has been found to be linked with the deflation of the main magmatic reservoir

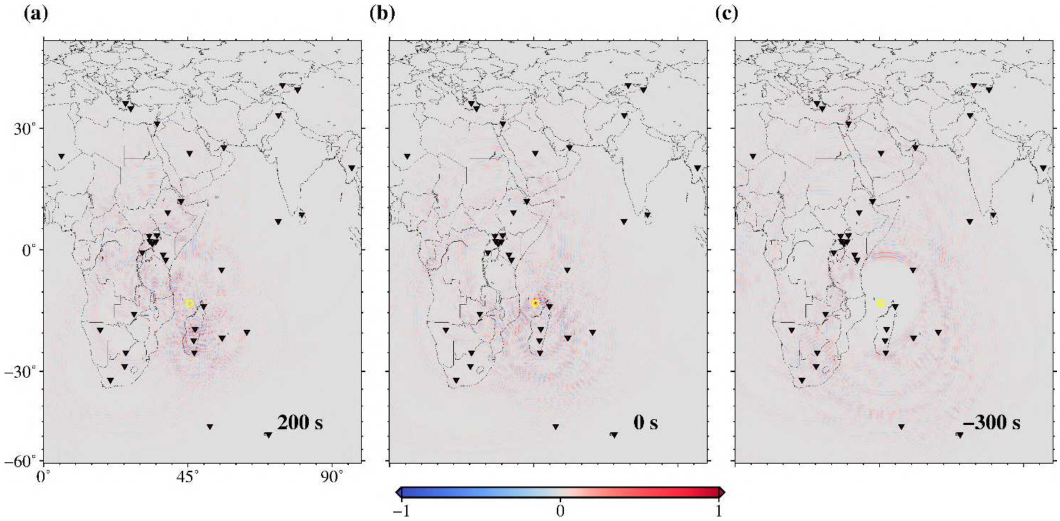

Fig. 3.4 Results of surface wave ray tracing time reversal simulation using real data (11 November 2018, M_s 5.1), in the 20-40s period band using recordings from 44 stations. Here time t = 0 s is VLP initiation time (catalog reported by Cesca et al. (2020)).

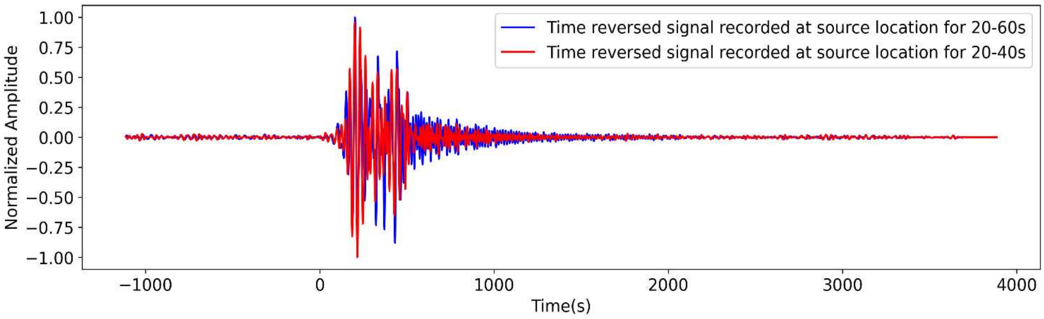

Fig. 3.5 Time-reversed signal recorded at the epicenter of the VLP event (11 November 2018) as reconstructed by time-reversal simulation in 20-40s (red curve) and 20-60s (blue curve) period bands. Again, time t=0 is defined as the origin time of the event.

(Cesca et al., 2020; Lemoine et al., 2020).

3.5 Smaller VLP events

We apply our method to several other VLP events. To limit the effect of non homogeneity in the azimuthal distribution of seismic stations, which could deteriorate the focusing of the time-reversed wave field, we are forced to discard recordings from more densely instrumented area: after making such a selection, we are left with 30 seismic stations only, from several different networks. Using the associated recordings, we locate four VLP events with estimated surface-wave magnitudes M_s 4.7, 5.0, 4.6, 5.0, that oc-

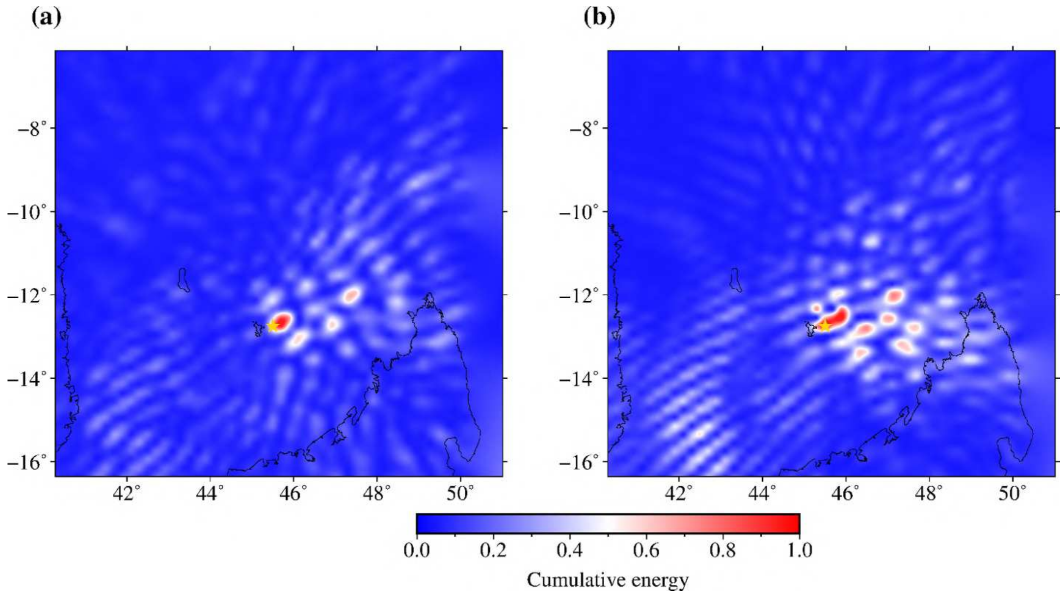

Fig. 3.6 Integrated energy over 20s after the initiation of November 11, 2018, VLP event obtained by time-reversal and back-propagation of Rayleigh waves after band-pass filtering between (a) 20-40s and (b) 20-60s. The yellow star shows the source location estimated by Cesca et al. (2020) via centroid-moment-tensor inversion.

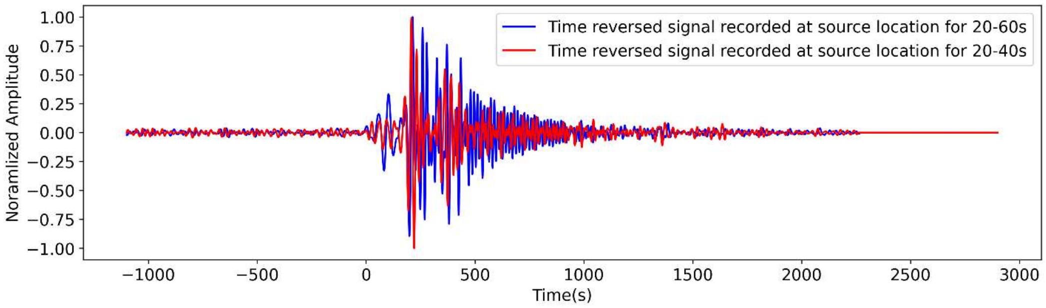

Fig. 3.7 Time-reversed signal recorded at epicenter of 16 July 2018 VLP event of M_s 5.02 as reconstructed by time-reversal simulation in 20-40s (red curve) and 20-60s (blue curve) period bands.

curred on 21 September, 31 July, 15 June, and 16 July 2018, respectively. It has been suggested that all these VLP events were triggered by the failure of the roof of a deep magma reservoir (Cesca et al., 2020). Our findings are generally in good agreement with the catalog provided by Cesca et al.(2020). Fig. 3.7 represents the time-reversed signal obtained at source location for 16 July 2018 VLP event, showing a source duration of less than 1,000s. Fig. 3.8 shows the energy distribution map for all the events of interest, with maxima always very close to independently estimated source locations. It has been suggested that all these VLP events were triggered by the failure of the roof of a deep magma reservoir (Cesca et al., 2020).

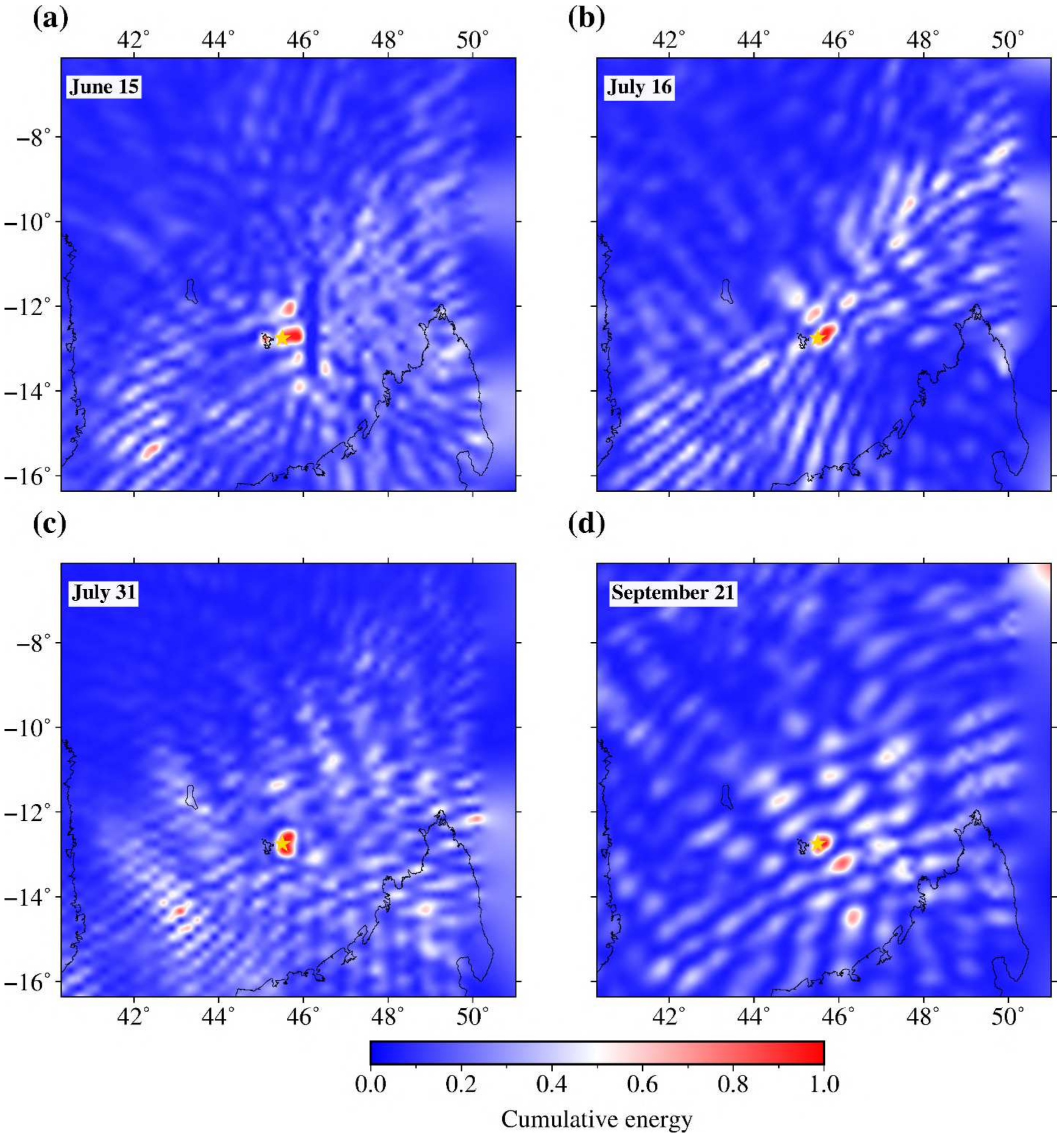

Fig. 3.8 Integrated energy over 20s after the initiation of a) June 15, b) July 16, c) July 31 and d) September 21, 2018, VLP events obtained from 20-40s period band simulation. Yellow stars as in Fig. 3.6.

Finally, we extend our analysis to the VLP event significantly smaller than the ones discussed above, that occurred on 7 February 2019, with an estimated surface wave magnitude of M_s of 3.4. We are able to use only 16 recordings from this event and thus perform the time-reversal simulation in the 20-40s band. Figures 3.9 and 3.10 show that there is no focusing of the time-reversed wave field, and/or the associated energy release, at the original location of the source. Therefore, the effectiveness of our method for lower magnitude events seems to be limited by the number of station and their distribution.

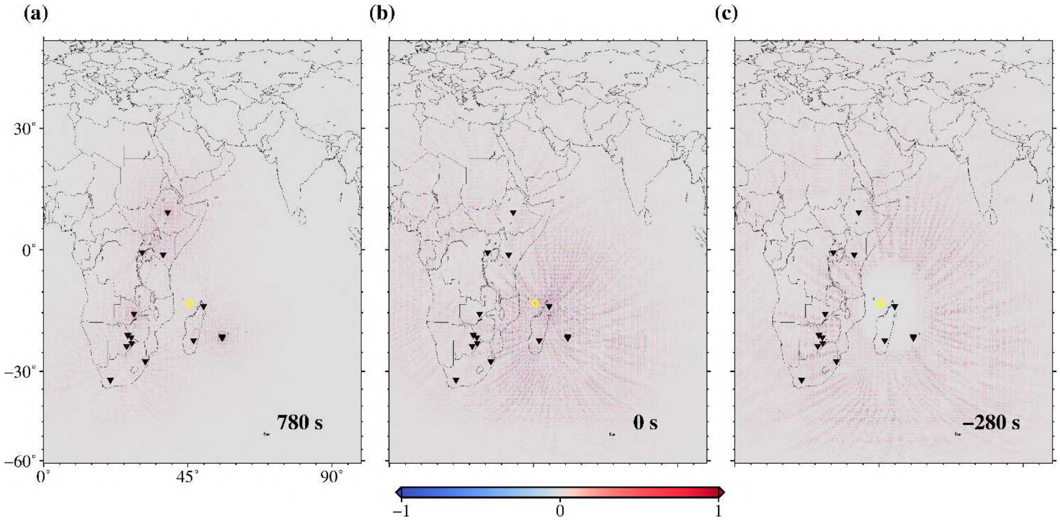

Fig. 3.9 Results of time-reversal simulation in 20-40s period band using 16 seismic recordings of 7 February 2019 VLP event (M_s 3.4). Here, in panel (b) no convergence is seen at source location and time that corresponds to origin position and time of the event.

3.6 Discussion and Conclusions

We time-reversed and back-propagated Rayleigh-wave seismograms, and identified the time(s) and place(s) of convergence of the time-reversed wave field to constrain the location, spatial extension, origin time and duration of VLP events within a volcanic active region near Mayotte Island. We analyzed five VLP events that occurred between June and November 2018 with a dominant period of ~16 sec and compared our location estimates with those obtained by centroid moment tensor inversion (Cesca et al., 2020): we find only small discrepancies (about 20 km on average, a fraction of the wave length of time-reversed data).

We found that the location uncertainty can be strongly influenced by the network geometry. For example, locally dense deployments (e.g., from network PF) can bias the location result. For this reason, in our study, we selected stations distributed homogeneously with different azimuths and distances, removing e.g., some redundant recordings from network PF. However, the sharpness of focusing of time-reversed wavefield increases with an increasing number of stations and better azimuthal coverage. For example, we

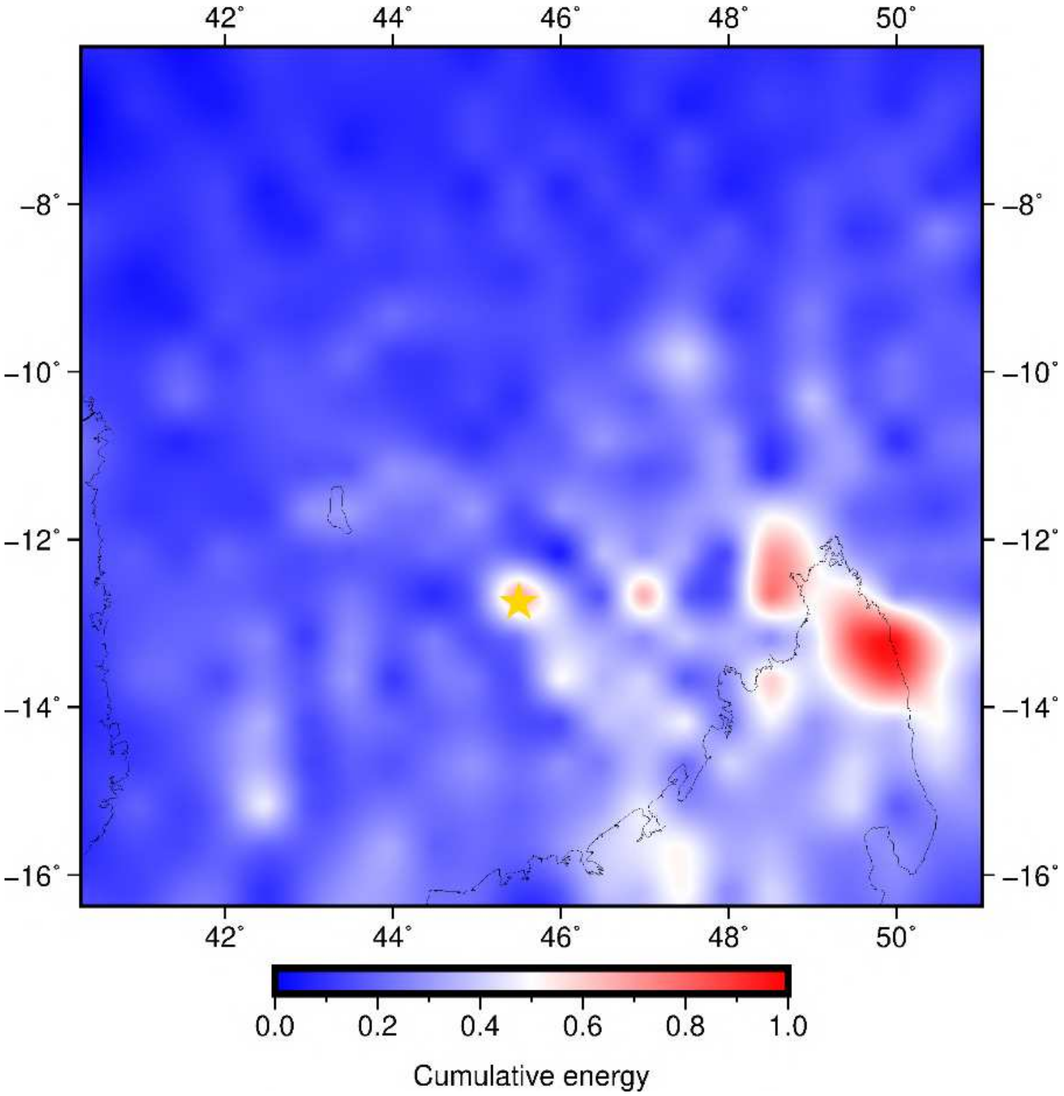

Fig. 3.10 Integrated energy for a smaller VLP event of M_s 3.4.

found that the wave field for the 16 July VLP event remains more diffuse, compared to the one occurred on 11 November VLP, which was recorded by more stations. Overall, our results indicated that relying on a limited, realistic number of seismic stations, our method gives a satisfactory time-reversal source location for such events.

An advantage of separating surface-wave frequencies and studying the corresponding wave fields individually is that, besides location, this also allows the characterization of the spatial characteristic of a source process with time. Also, the combination of different imaging fields provides a deeper understanding of the source process and the volume in which the re-broadcast is propagating. In an attempt to facilitate the visual identification of the proxy for energy propagation, we analyze the cumulative squared time-reversed displacement at each grid point from the time of initiation of the event to 20 s. Figs 3.6(a) and 3.8(b) show estimated energy distribution in both space and time, based on the 20-40 s band-passed time reversal simulations of the VLP events that occurred on 11 November and 16 July, respectively. Most of the time-reversed energy is mapped at the source location estimated by Cesca et al. (2020) via centroid moment tensor inversion (Fig. 3.8).

In the future, we plan to further improve the accuracy of our method, working on several limitations whose effects are apparent from this study. For instance, the signal of VLP events is typically dominated by 16 s period, and our simulation could only be carried out up to 25 s, due to the current unavailability of global phase-velocity models below 25 s. Further our method can be extended to map seismic faults in three dimensions. For this, we need to time-reverse and back-propagated a very dense suite of surface wave modes, and then combine them, with account of respective depth sensitivities. Finally, as explained by Fink (2006) and Boschi et al. (2018), a modelled time-reversed wave field does not simply disappear after focusing on the location of the original source but continues to propagate backward in time. For this non-physical signal to disappear, the source process itself needs to be modelled (backwards in time), introducing a term referred to as ‘sink’ that should absorb energy radiated during the later stages of the rupture process. This issue will be addressed in future works. Achieving these goals will contribute to our understanding on the geometry of magma plumbing systems beneath volcanoes, and to our ability of successfully forecasting eruptive activity, an important issue in the assessment of volcanic hazards.

References

Almendros, J., Chouet, B., Dawson, P. and Huber, C. (2002), ‘Mapping the sources of the seismic wave field at kilauea volcano, hawaii, using data recorded on multiple seismic antennas’, *Bulletin of the seismological society of America* **92**(6), 2333–2351.

Anderson, B. E., Griffa, M., Johnson, P. A., Larmat, C. and Ulrich, T. J. (2008), ‘Time reversal’.

Battaglia, J. and Aki, K. (2003), ‘Location of seismic events and eruptive fissures on the piton de la fournaise volcano using seismic amplitudes’, *Journal of Geophysical Research: Solid Earth* **108**(B8).

Battaglia, J., Got, J.-L. and Okubo, P. (2003), ‘Location of long-period events below kilauea volcano using seismic amplitudes and accurate relative relocation’, *Journal of Geophysical Research: Solid Earth* **108**(B12).

Bean, C. J., De Barros, L., Lokmer, I., Métaxian, J.-P., O’Brien, G. and Murphy, S. (2014), ‘Long-period seismicity in the shallow volcanic edifice formed from slow-rupture earthquakes’, *Nature geoscience* **7**(1), 71–75.

Boschi, L., Molinari, I. and Reinwald, M. (2018), ‘A simple method for earthquake location by surface-wave time reversal’, *Geophysical Journal International* **215**(1), 1–21.

Boschi, L. and Woodhouse, J. H. (2006), ‘Surface wave ray tracing and azimuthal anisotropy: a generalized spherical harmonic approach’, *Geophysical Journal International* **164**(3), 569–578.

Cesca, S., Battaglia, J., Dahm, T., Tessmer, E., Heimann, S. and Okubo, P. (2008), ‘Effects of topography and crustal heterogeneities on the source estimation of lp event at kilauea volcano’, *Geophysical Journal International* **172**(3), 1219–1236.

Cesca, S., Letort, J., Razafindrakoto, H. N., Heimann, S., Rivalta, E., Isken, M. P., Nikkhoo, M., Passarelli, L., Petersen, G. M., Cotton, F. et al. (2020), ‘Drainage of a deep magma reservoir near mayotte inferred from seismicity and deformation', *Nature geoscience* **13**(1), 87–93.

Chouet, B. A. (1996), 'Long-period volcano seismicity: its source and use in eruption forecasting', *Nature* **380**(6572), 309–316.

De Barros, L., Bean, C. J., Lokmer, I., Saccorotti, G., Zuccarello, L., O'Brien, G. S., Métaxian, J.-P. and Patane, D. (2009), 'Source geometry from exceptionally high resolution long period event observations at mt etna during the 2008 eruption', *Geophysical Research Letters* **36**(24).

Del Pezzo, E. and Patané, D. (1992), 'Volcanic seismology. iavcei proceedings in volcanology'.

Ekström, G. (2011), 'A global model of love and rayleigh surface wave dispersion and anisotropy, 25-250 s', *Geophysical Journal International* **187**(3), 1668–1686.

Fink, M. (1999), 'Time-reversed acoustics', *Scientific American* **281**(5), 91–97.

Fink, M. (2006), 'Time-reversal acoustics in complex environments', *geophysics* **71**(4), SI151–SI164.

Fink, M., Montaldo, G. and Tanter, M. (2003), 'Time-reversal acoustics in biomedical engineering', *Annual review of biomedical engineering* **5**(1), 465–497.

Gaete, A., Cesca, S., Franco, L., San Martin, J., Cartes, C. and Walter, T. R. (2019), 'Seismic activity during the 2013–2015 intereruptive phase at lascar volcano, chile', *Geophysical Journal International* **219**(1), 449–463.

Griffa, M., Anderson, B., Guyer, R., Ulrich, T. and Johnson, P. (2008), 'Investigation of the robustness of time reversal acoustics in solid media through the reconstruction of temporally symmetric sources', *Journal of physics D: Applied physics* **41**(8), 085415.

Grigoli, F., Cesca, S., Amoroso, O., Emolo, A., Zollo, A. and Dahm, T. (2014), 'Automated seismic event location by waveform coherence analysis', *Geophysical Journal International* **196**(3), 1742–1753.

Grigoli, F., Cesca, S., Vassallo, M. and Dahm, T. (2013), 'Automated seismic event location by travel-time stacking: An application to mining induced seismicity', *Seismological Research Letters* **84**(4), 666–677.

Kao, H. and Shan, S.-J. (2004), 'The source-scanning algorithm: Mapping the distribution of seismic sources in time and space', *Geophysical Journal International* **157**(2), 589–594.

Kumagai, H., Placios, P., Ruiz, M., Yepes, H. and Kozono, T. (2011), 'Ascending seismic source during an explosive eruption at tungurahua volcano, ecuador', *Geophysical Research Letters* **38**(1).

Larmat, C., Guyer, R. and Johnson, P. (2009), 'Tremor source location using time reversal: Selecting the appropriate imaging field', *Geophysical Research Letters* **36**(22).

Larmat, C., Montagner, J.-P., Fink, M., Capdeville, Y., Tourin, A. and Clévédé, E. (2006), 'Time-reversal imaging of seismic sources and application to the great sumatra earthquake', *Geophysical Research Letters* **33**(19).

Larmat, C., Tromp, J., Liu, Q. and Montagner, J.-P. (2008), 'Time reversal location of glacial earthquakes', *Journal of Geophysical Research: Solid Earth* **113**(B9).

Legrand, D., Kaneshima, S. and Kawakatsu, H. (2000), 'Moment tensor analysis of near-field broadband waveforms observed at aso volcano, japan', *Journal of volcanology and geothermal research* **101**(1-2), 155–169.

Lemoine, A., Briole, P., Bertil, D., Roullé, A., Foumelis, M., Thinon, I., Raucoules, D., de Michele, M., Valty, P. and Hoste Colomer, R. (2020), 'The 2018–2019 seismo-volcanic crisis east of mayotte, comoros islands: seismicity and ground deformation markers of an exceptional submarine eruption', *Geophysical Journal International* **223**(1), 22–44.

Lokmer, I., Bean, C. J., Saccorotti, G. and Patane, D. (2007), 'Moment-tensor inversion of lp events recorded on etna in 2004 using constraints obtained from wave simulation tests', *Geophysical Research Letters* **34**(22).

Lokmer, I., O’Brien, G. S., Stich, D. and Bean, C. J. (2009), ‘Time reversal imaging of synthetic volcanic tremor sources’, *Geophysical Research Letters* **36**(12).

Matoza, R. S., Shearer, P. M., Lin, G., Wolfe, C. J. and Okubo, P. G. (2013), ‘Systematic relocation of seismicity on hawaii island from 1992 to 2009 using waveform cross correlation and cluster analysis’, *Journal of Geophysical Research: Solid Earth* **118**(5), 2275–2288.

Matoza, R. S., Shearer, P. M. and Okubo, P. G. (2014), ‘High-precision relocation of long-period events beneath the summit region of kılauea volcano, hawai ‘i, from 1986 to 2009’, *Geophysical Research Letters* **41**(10), 3413–3421.

McNutt, S. R. (2005), ‘Volcanic seismology’, *Annu. Rev. Earth Planet. Sci.* **32**, 461–491.

Metaxian, J.-P., Lesage, P. and Valette, B. (2002), ‘Chemistry and physics of minerals and rocks/volcanology-ecv 10-locating sources of volcanic tremor and emergent events by seismic triangulation: Application to arenal volcano, costa rica (doi’, *Journal of Geophysical Research-Part B-Solid Earth* **107**(10).

Michon, L. (2016), ‘The volcanism of the comoros archipelago integrated at a regional scale’, *Active Volcanoes of the Southwest Indian Ocean: Piton de la Fournaise and Karthala* pp. 333–344.

Montesinos, B. M., Bean, C. J. and Lokmer, I. (2021), ‘Quantifying strong seismic propagation effects in the upper volcanic edifice using sensitivity kernels’, *Earth and Planetary Science Letters* **554**, 116683.

Morioka, H., Kumagai, H. and Maeda, T. (2017), ‘Theoretical basis of the amplitude source location method for volcano-seismic signals’, *Journal of Geophysical Research: Solid Earth* **122**(8), 6538–6551.

Obara, K. (2002), ‘Nonvolcanic deep tremor associated with subduction in southwest japan’, *Science* **296**(5573), 1679–1681.

Ohminato, T., Chouet, B. A., Dawson, P. and Kedar, S. (1998), ‘Waveform inversion of very long period impulsive signals associated with magmatic injection beneath kilauea volcano, hawaii’, *Journal of Geophysical Research: Solid Earth* **103**(B10), 23839–23862.

Pelleter, A.-A., Caroff, M., Cordier, C., Bachelery, P., Nehlig, P., Debeuf, D. and Arnaud, N. (2014), ‘Melilite-bearing lavas in mayotte (france): An insight into the mantle source below the comores’, *Lithos* **208**, 281–297.

Rowley, P., Benson, P. M. and Bean, C. J. (2021), ‘Deformation-controlled long-period seismicity in low-cohesion volcanic sediments’, *Nature Geoscience* **14**(12), 942–948.

Saccorotti, G., Lokmer, I., Bean, C. J., Di Grazia, G. and Patanè, D. (2007), ‘Analysis of sustained long-period activity at etna volcano, italy’, *Journal of volcanology and geothermal research* **160**(3-4), 340–354.

Scrutton, R., Heptonstall, W. and Peacock, J. (1981), ‘Constraints on the motion of madagascar with respect to africa’, *Marine Geology* **43**(1-2), 1–20.

Sharma Dhakal, A., Molinari, I. and Boschi, L. (2023), ‘Seismic source mapping by surface wave time reversal: application to the great 2004 sumatra earthquake’, *Geophysical Journal International* **233**(2), 1018–1035.

Shelly, D. R., Beroza, G. C., Ide, S. and Nakamula, S. (2006), ‘Low-frequency earthquakes in shikoku, japan, and their relationship to episodic tremor and slip’, *Nature* **442**(7099), 188–191.

Wassermann, J. (2012), Volcano seismology, *in* ‘New manual of seismological observatory practice 2 (NMSOP-2)’, Deutsches GeoForschungsZentrum GFZ, pp. 1–77.

Zinke, J., Reijmer, J., Thomassin, B., Dullo, W.-C., Grootes, P. and Erlenkeuser, H. (2003), ‘Postglacial flooding history of mayotte lagoon (comoro archipelago, southwest indian ocean)’, *Marine Geology* **194**(3-4), 181–196.

CHAPTER 4

Preliminary application to 2023 M_w 7.8 Turkey earthquake

ABSTRACT

The magnitude M_w 7.8 event, associated with the East Anatolian Fault system, that occurred on 6 February 2023, is one of the most devastating earthquakes in Turkey after the 1939 M_w 7.9 Erzincan earthquake. We apply surface wave time-reversal to the vertical-component of seismograms for this event, using recordings from 86 stations of the Global Seismographic Network (GSN), CH and IV network. In the following, we show our resulting estimates for the direction of rupture propagation, its spatial extent and duration.

Keywords: *Rupture*, *Turkey earthquake*, *Time-reversal*, *Ray tracing*

4.1 Introduction

4.1.1 Study area

The tectonic characteristics of central southern Turkey and northwestern Syria are controlled by convergence of three major plates: the African Plate, the Arabian Plate and the Anatolian Plate (McKenzie, 1972; Dewey et al., 1973). The Dead Sea Transform (DST), a major zone of sinistral strike-slip, accommodates differential motion between the African and Arabian plates. The northern end of the DST terminates at the East Anatolian Fault (EAF), which is another major active tectonic structure of the Eastern Mediterranean region. This fault is mainly characterized by left-lateral strike-slip and accommodates the overall westward movement of the Anatolian Plate and northward movement of the Arabian Plate (Dewey et al., 1986; Barka et al., 1997). It is a complex system that runs from Karliova triple junction in the northeast, terminating at the North Anatolian Fault zone, and can be sub-divided into 16 different segments based on the fault step overs, separation or change in the fault strike (Emre et al., 2018). The slip rate varies along the system, decreasing south-westwards, with a maximum value of 10 millimeters per year near Karliova segment, down to 2.5 millimeters per year on the Cardak segment (Güvercin et al., 2022).

Several large, damaging earthquake have occurred in the past few hundred years on the various segments of EAF, including 1893 (M_s 7.1, Erkenek), 1971 (M_s 606, Karliova) and 2020 (M_w 6.8, Pütürge) events (Güvercin et al., 2022; Milkereit et al., 2004). The recent earthquake of magnitude M_w 7.8 that occurred on February 6, 2023 is also associated with the EAF system, and caused massive damage to buildings and infrastructures and, more than 57,000 casualties in Turkey and Syria. The earthquake was located at 37.23°N and 37.019°E, with hypocentral depth of 13.1 km. A strong aftershock of M_w 6.8 occurred, just ten minutes after the mainshock. Approximately nine hours later, an earthquake of magnitude M_w 7.5 occurred near the city of Ekinözül, Turkey. This earthquake is associated with the northern strand of the EAF. Over two weeks following the mainshock, around 7451 aftershocks were recorded, 433 of which

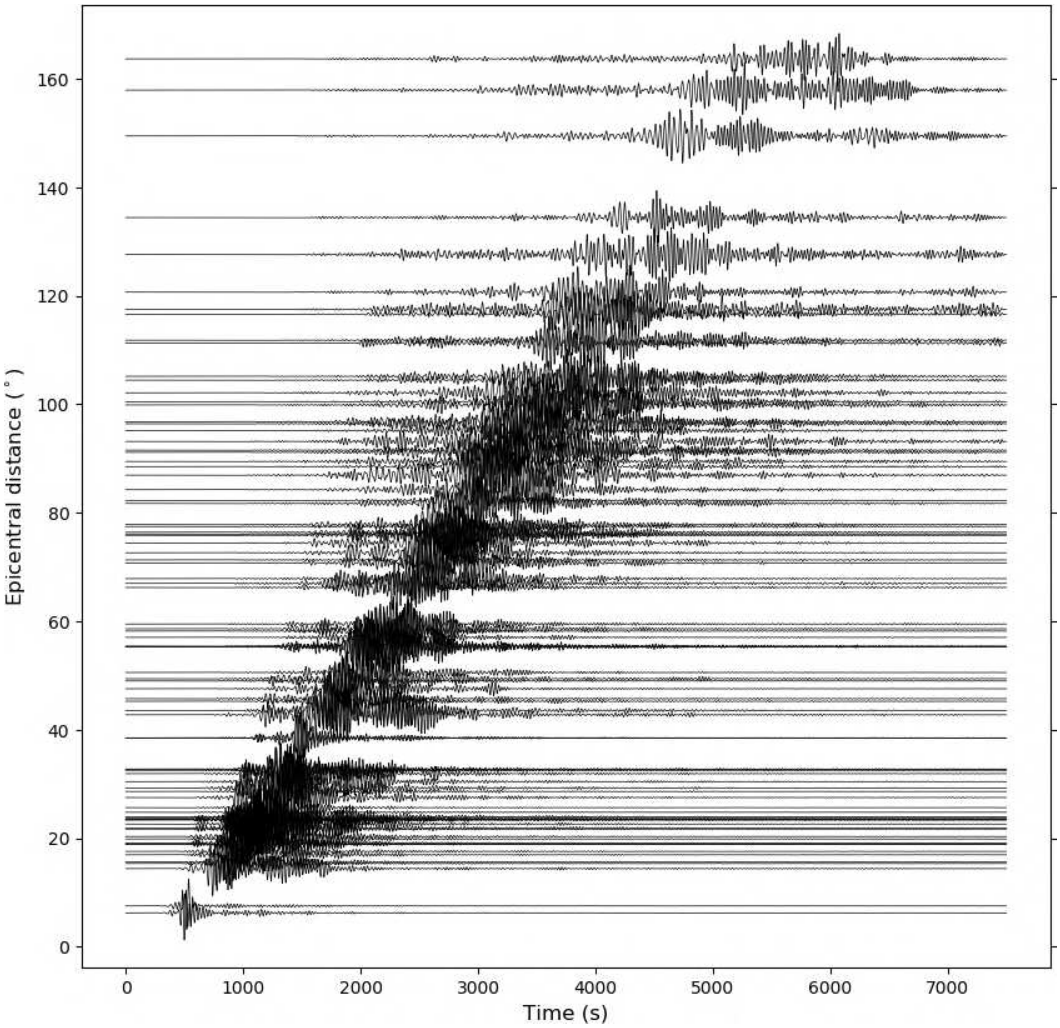

Fig. 4.1 Vertical component recordings of 2023 February 6, M_w 7.8 Turkey earthquake from 86 stations, filtered in the period band 20-to-55 s.

have magnitude exceeding M_w 5.0 (Cetin et al., 2023).

4.2 February 6, 2023 Mw 7.8 Turkey earthquake

We apply our surface wave ray-tracing and time-reversal method to the vertical-component of recordings of the 2023 February 6, Turkey earthquake, M_w = 7.8, 01:17:35. We took 86 recordings from IRIS/USGS Global Seismographic Network (GSN) (Scripps Institution of Oceanography, 1986; Albuquerque Seismological Laboratory/USGS, 2014), IV (Istituto Nazionale di Geofisica e Vulcanologia (INGV), 2005) and CH (Swiss Seismological Service (SED) At ETH Zurich, 1983) networks that are distributed as uniformly as possible over the globe.

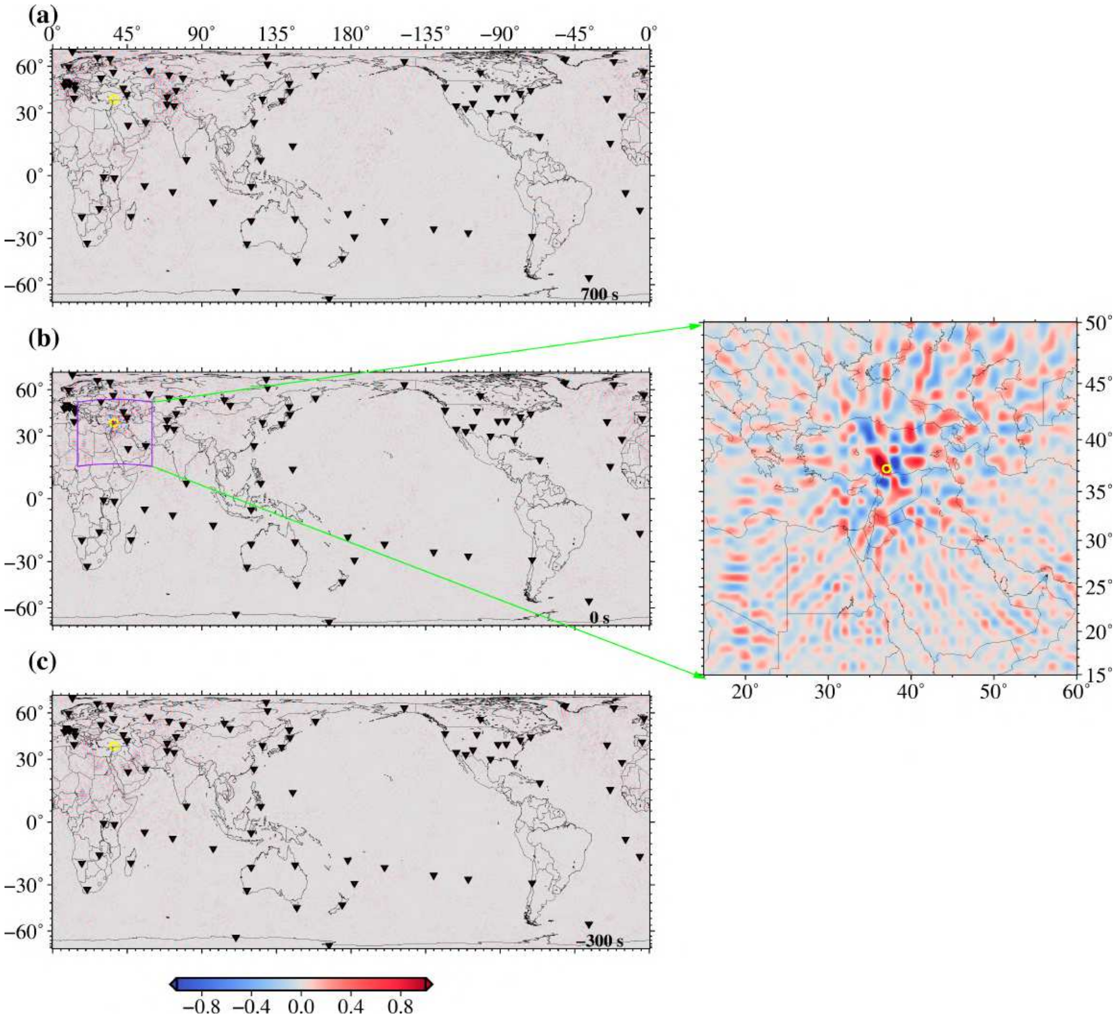

Fig. 4.2 Snapshots of the vertical component of the time-reversed wave field at different times, for 2023 February 26, M_w 7.8 Turkey earthquake in the 20-to-55 s period band using recordings from 86 stations (shown as black triangles). We have chosen t=0 s to correspond to the earthquake origin time as reported by the USGS. Snapshots (a) is taken at time t=700s; (b) at t = 0 s and (c) at t = -300 s.

We remove the instrumental response for each trace, resample them to match the time step used in the back-propagation and apply a band-pass filter in the 20-to-55 s period band (Fig. 4.1). Further, we trace Rayleigh-wave ray paths in a heterogeneous phase velocity map from Ekström (2011), specifically at 35 sec. It is found that the back-propagated wavefield focuses on the expected source location. Fig. 4.2 shows global snapshots of the time-reversed wavefield; only the region of interest is ahown in Fig. 4.2(b), at the moment of maximum focusing of the time-reversed wave field. The main peak occurs at 37.23°N and 37.03°E, which approximately coincides with the epicenter of USGS estimate.

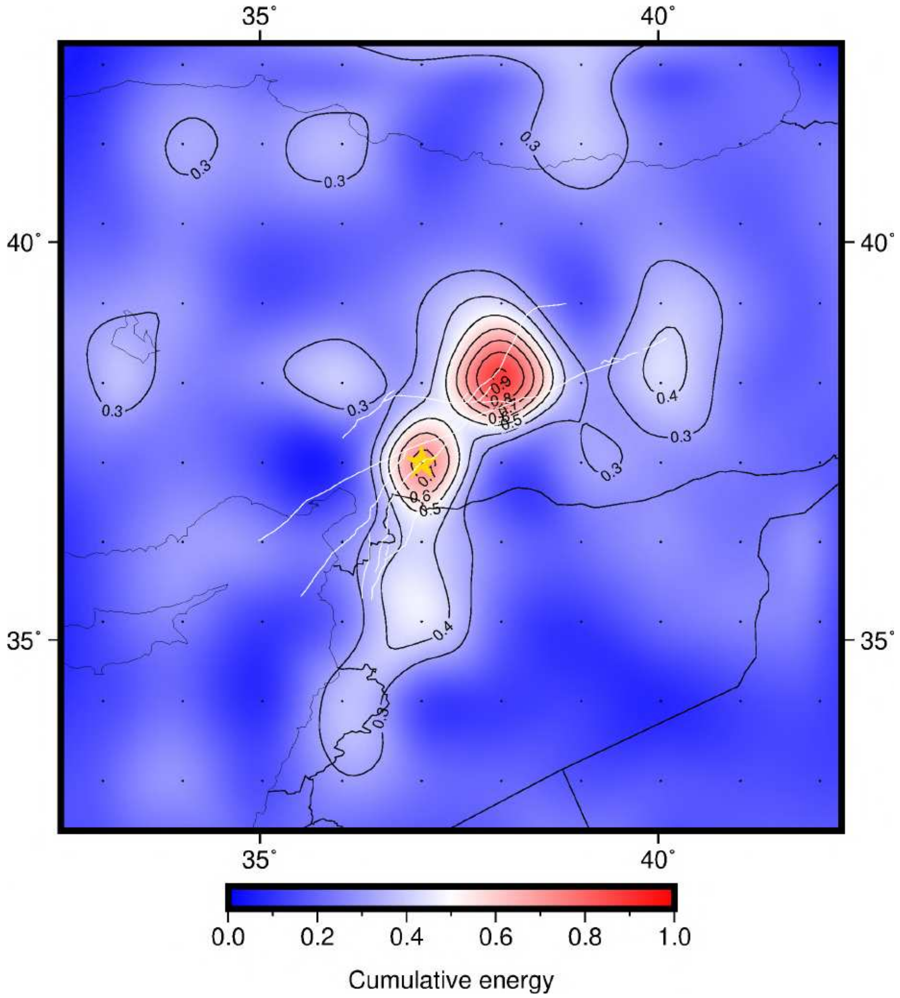

Fig. 4.3 Approximate estimate of seismic energy computed from data bandpass filtered between 20 and 55 s. Energy is normalized to 1 and plotted only in the area where it is large. A yellow star denotes the USGS epicenter location.

We next squared the time-reversed trace (20-to-55 s), integrate them over time from the initiation of earthquake to 140 s, and obtain a rough estimate of relative strength of total energy released as a function of location (Fig. 4.3). Fig. 4.4 shows energy variation with time over the grid. We observe unilateral propagation of rupture to the northeast of the East Anatolian Fault and then continues bilaterally to the northeast and southwest along the East Anatolian Fault. Our result somehow resembles with the conclusion drawn recently by Melgar et al. (2023) and Petersen et al. (2023).

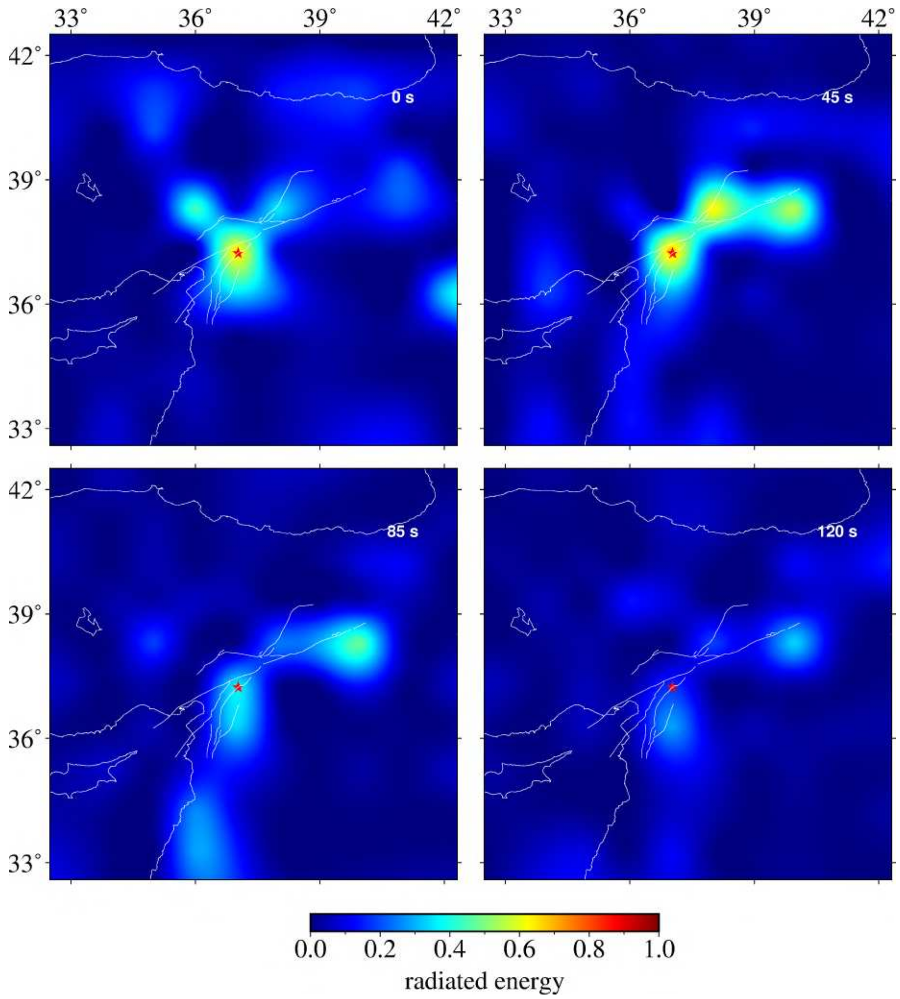

Fig. 4.4 Rupture progression for 2023 February 26 Turkey earthquake. The distribution of energy radiation at different times interval. The rupture migrates unilaterally towards the northeast and further propagates bilaterally to northeast and southwest along the EAF segment. A red star denotes the USGS epicenter location; white lines represent the surface expressions of the fault (and the coastlines).

References

Albuquerque Seismological Laboratory/USGS (2014), 'Global seismograph network (gsn - iris/usgs)'.

URL: *https://www.fdsn.org/networks/detail/IU/*

Barka, A., Reilinger, R. et al. (1997), 'Active tectonics of the eastern mediterranean region: deduced from gps, neotectonic and seismicity data'.

Cetin, K. Ö., Ilgaç, M., Can, G. and Çakır, E. (2023), 'Preliminary reconnaissance report on february 6, 2023, pazarcık mw=7.7 and elbistan mw=7.6, kahramanmaraş-türkiye earthquakes', *Middle East Technical University. Retrieved 1 March 2023.* .

Dewey, J. F., III, W. C. P., Ryan, W. B. F. and Bonnin, J. (1973), 'Plate tectonics and the evolution of the alpine system', *Geological society of America bulletin* **84**, 3137–3180.

Dewey, J., Hempton, M., Kidd, W., Saroglu, F. and Şengör, A. (1986), 'Shortening of continental lithosphere: the neotectonics of eastern anatolia — a young collision zone', *Geological Society, London, Special Publications* **19**, 1–36.

Ekström, G. (2011), 'A global model of love and rayleigh surface wave dispersion and anisotropy, 25-250 s', *Geophysical Journal International* **187**(3), 1668–1686.

Emre, Ö., Duman, T. Y., Özalp, S., Şaroğlu, F., Olgun, Ş., Elmacı, H. and Çan, T. (2018), 'Active fault database of turkey', *Bulletin of Earthquake Engineering* **16**(8), 3229–3275.

Güvercin, S. E., Karabulut, H., Özgün Konca, A., Doğan, U. and Ergintav, S. (2022), 'Active seismotectonics of the east anatolian fault', *Geophysical Journal International* **230**, 50–69.

Istituto Nazionale di Geofisica e Vulcanologia (INGV) (2005), 'Rete sismica nazionale (rsn)'.
URL: *http://terremoti.ingv.it/instruments/network/IV*

McKenzie, D. (1972), 'Active tectonics of the mediterranean region', *Geophysical Journal International* **30**, 109–185.

Melgar, D., Taymaz, T., Ganas, A., Crowell, B., Öcalan, T., Kahraman, M., Tsironi, V., Yolsal-Çevikbil, S., Valkaniotis, S., Irmak, T. S., Eken, T., Erman, C., Özkan, B., Dogan, A. H. and Altuntaş, C. (2023), 'Sub- and super-shear ruptures during the 2023 mw 7.8 and mw 7.6 earthquake doublet in se türkiye', *Seismica* **2**.

Milkereit, C., Grosser, H., Wang, R., Wetzel, H.-U., Woith, H., Karakisa, S., Zunbul, S. and Zschau, J. (2004), 'Implications of the 2003 bingol earthquake for the interaction between the north and east anatolian faults', *Bulletin of the Seismological Society of America* **94**, 2400–2406.

Petersen, G., Büyükakpinar, P., Vera, F., Metz, M., Saul, J., Cesca, S., Dahm, T. and Tilmann, F. (2023), 'Rupture processes of the 2023 türkiye earthquake sequence: Main- and aftershocks'.

Scripps Institution of Oceanography (1986), 'Global seismograph network - iris/ida'.
URL: *https://www.fdsn.org/networks/detail/II/*

Swiss Seismological Service (SED) At ETH Zurich (1983), 'National seismic networks of switzerland'.
URL: *http://networks.seismo.ethz.ch/networks/ch/*

CHAPTER 5

CONCLUSIONS

5.1 Summary of this thesis' contribution

The main contribution of this thesis is the application of surface-wave time reversal to three problems in earthquake localization and source reconstruction: the great Sumatra earthquake, the 6 February 6 2023 M_w 7.8 Turkey earthquake and a sequence of anomalous events associated with volcanism at Mayotte Island. We model surface-waves propagation (whether forward or backward in time) via the membrane-wave approach (Tanimoto, 1990; Peter et al., 2009). This rests on the fundamental result that the scalar, two-dimensional wave equation can be used to model surface wave propagation in a laterally smooth, lossless half-space, thus reducing the computational costs. We implement Rayleigh-wave propagation via ray tracing on a spherical earth using Boschi and Woodhouse's (2006) algorithm, which, importantly, allows to account not only for isotropic phase velocity heterogeneity, but also for laterally varying azimuthal anisotropy of surface-wave phase velocity. The algorithm used here is an improvement with respect to Boschi and Woodhouse (2006), in that a numerical optimization technique, the golden section search method, was introduced in the software module that traces rays. The golden section search is an effective way to more rapidly narrow down the search range to a smaller interval, until optimiziation is achieved. Convergence to the correct initial azimuth and ray path is much faster, reducing significantly the computational time.

The main motivation of our work was to incorporate, in order to reconstruct seismic sources more accurately than currently possible, a segment of seismogram that is typically not included in source inversions: the surface waves. This would supplement the current slip inversion techniques, which primarily rely on seismic observations of high frequency ($\sim$ 1HZ) such as body waves or geodetic observations of almost zero-frequency, such as GPS and INSAR. However, these methods are unable to take advantage of the extensive information contained in surface-wave frequencies.

The benefit of seismic time reversal over other methods is that it does not require any prior interpretation of time-series data and gradually trace the time-reversal wave-field to reconstruct the refocusing region. Thus, a solution exists where the set of waves that diverge from a source (which may include reflected, refracted, or scattered) and precisely retrace all of the complex paths and converge at the original source location, as if time was moving backwards.

The computational expense of our method highly depends on the number of source-station pairs, as well as the spatial separation between grid nodes. Our method is straightforward to be parallelized since ray tracing for each station is independent. One simulation for one station is carried out in one CPU, i.e., for 89 stations, 89 CPUs are used. The computation time to run whole simulation is $\sim$ 10 hours when a grid spacing of 1° X 1° is used (Sumatra earthquake) and $\sim$ 26 hours for 0.5° X 0.5° (very long period events).

We begin with a series of synthetic experiments to test the effectiveness of our time-reversal method with the station distribution and error in velocity model. When we refer to synthetic numerical tests, it means that both the forward and backward propagation are carried out numerically, i.e., with theoretical seismograms rather than real-world data, are time-reversed and back-propagated.

a) The first test verifies that almost perfect focusing can be achieved at the correct source location and at the appropriate origin time, if stations are densely distributed at uniform azimuthal coverage around the source. This is a confirmation that our theory is correct and our software error-free. Of course, reducing the density and uniformity of the stations reduces the accuracy of our method, but we find that our results are satisfactory, and the method can be useful, when applied to “realistic” station distributions.

b) The second test quantifies the importance of the accuracy of the velocity model for the convergence of our time-reversed wave field. Synthetics computed in a heterogeneous model are backpropagated through a homogeneous model. It is found that the computed time-reversed wave field converges about 250 kilometers away from the actual source position as depicted in Fig. 2.5(e) (Chapter 2). Also, the main peak at the time of focusing is not as precise, compared to when the correct phase velocity model is used for backpropagation. We conclude that results from the time-reversal simulation are significantly affected by the accuracy of the velocity model used for modeling backpropagation.

c) A third test is conducted to determine whether taking into account azimuthal anisotropy should impact our results. The test shows that time-reversed wave fields obtained with and without anisotropy are very similar: the error in the reconstructed origin time is on the order of a few seconds.

In summary, the reliability of our method mostly depends on the density and uniformity of station coverage, and on the reliability of phase velocity models.

After validating our method by synthetic tests, we applied it to 89 recordings (IRIS/USGS Global Seismographic Network) from the magnitude of M_w 9.3 December 26, 2004, Sumatra-Andaman earthquake. This is an important, further test, since Sumatra is one of the largest and mostly studied earthquakes of all times, and there exist a large literature against which we compared our results. We performed time-reversal simulations in the 40-to-90, 50-to-120 and 80-to-120 s bands and found that the time-reversal and backward propagation of the vertical-component seismograms resulted in focusing the signal at the location and time of the source i.e., epicenter and origin time of the earthquake, as estimated by other authors.

We next mapped the energy distribution in space and time associated with the earthquake. We obtained a proxy for the energy propagation and found rupture propagation to be unidirectional, i.e., from south to north, with the rupture lasting nearly 600 s after the initiation of the earthquake. Also, we found two areas where most of the energy appears to be released. The strongest energy radiation occurred to the southwest of northern Sumatra, followed by a second important radiation to the north of the Nicobar Island. These estimates are in good agreement with other studies (Ammon et al., 2005; Ishii et al., 2005; Krüger and Ohrnberger, 2005; Lay et al., 2005). Also we relocate the 6 February 2023 Turkey earthquake and map the migration of its rupture that is found to be bilateral along the EAF segment.

Finally, we applied our method to a very different class of events: very low-frequency signals recorded at regional and teleseismic distances on Mayotte Island, a volcanic island. Again, we conducted synthetic tests to determine the effectiveness of our approach at this scale and for events of this magnitude, considering the extent of data coverage available for the VLP events of interest. Locating and characterizing the source of VLP events is challenging due to the lack of a distinct arrival of P- and S-waves, and because the onsets of seismic arrival are systematically unclear. For the largest VLP event on 11 November 2019, with an estimated surface-wave magnitude M_s of 5.1, we used 44 recordings and conducted time-reversal simulations in four different frequency bands: 20-to-40, 20-to-60, 20-100 and 20-140 s. By identifying the maximum convergence of time-reversed wave field, we located the position and time of the event and compared our results with those obtained through centroid moment tensor inversion (Cesca et al., 2020). The location is very consistent for all the simulations, indicating that our results are not strongly dependent on the frequency band. The average location error is found to be in order of 20 km. Additionally, we estimated the waveform of the signal emitted by the source, which had a duration of 1000 seconds. We found the time-reversed energy of the event to be concentrated very near the source coordinates, as estimated by centroid moment tensor inversion.

As previously discussed, the location accuracy of our method is dependent on the distribution and geometry of recording instruments. Due to the scarcity of recordings for lower-magnitude VLP events at Mayotte, the focusing of the associated time-reversed wave field is significantly less sharp than for larger VLP events. However, we have successfully reconstructed the location for four different VLP events with estimated surface-wave magnitude M_s of 4.7, 5.0, 4.6 and 5.0 using only 30 seismic stations. Again, the locations we have identified are consistent with those in the catalog provided by Cesca et al. (2020) within the same margin of error. It has been suggested that all these VLP events were triggered by the failure of the roof of a deep magma reservoir (Cesca et al., 2020). Events with lower magnitudes are more difficult to observe, and our method accordingly appears to be less effective. We applied it to a smaller VLP event. with surface wave magnitude only 3.4, for which only 16 recordings were available. The result revealed no focusing of the wave-field at the original location of the source.

5.2 Future contributions

The conclusions of the previous section suggests that better results could be obtained with small-magnitude event, if one could increase the number of time-reversed/back-propagated recordings. In the exercise described in chapter 3, recognizable arrivals were “picked” before time-reversal. But, the focusing of the time-reversed field is a consequence of constructive interference, and we speculate that, in the time-reversed field, very noisy seismograms could still contribute to sharpen the focusing. This deserves to be explored in future work.

One important limitation of our study is that it is entirely two-dimensional. It should be seen, though, as the first step towards the reconstruction of three-dimensional maps of seismic slip, both in space and time. This will require conducting time-reversal simulation at a dense range of surface wave modes, accounting for their respective depth sensitivities. Since surface waves of different frequencies have different penetration depths, i.e., they are sensitive to different depths of subsurfaces; multiple, two-dimensional time-reversal simulations of surface waves will be conducted at different frequencies. Then, the results obtained from these multiple time-reversal simulation would be combined to create a three-dimensional map of seismic slips. This way we could explore the resolving power of our method in vertical direction (i.e., in depth).

Additionally, according to Fink (2006) and Boschi et al. (2018), the time-reversed wave field does not simply disappear after focusing on the location of the original source, but continues to travel backward in time. To eliminate this non-physical signal, the source process itself needs to be modeled backward in time, introducing a term referred to as a ‘sink’ that absorbs energy radiated during the later stage of the rupture process. This issue needs to be addressed in future studies. Hence, the implementation of a sink (time-reversed source) is required to absorb the time-reversed wave precisely at the original source location and at the exact refocusing time, and without it, the time-reversed wave field cannot be made zero for times before the initial seismic source was activated. The idea of using a sink to remove outgoing wave, so that the total field is equal to the incoming one, has recently been extended to microwaves and acoustic waves (de Rosny and Fink, 2002; Pu et al., 2012). It requires a prior knowledge of the incoming signal. This issue needs to be addressed in future studies. One possible approach would be to divide the source mapping process into two steps. The first step would involve emitting the original signal at the exact time of merging (i.e., interruption in time reversal prior to the focusing) that would suppress the diverging wave thus allowing the reconstruction of the surface-wave field in the immediate vicinity of the source. Second step would involve the reconstructed near-field displacement to be treated as data in a classic linear inverse problem (as demonstrated in Ide (2007)), with slip on the fault as the unknown variables.

Finally, once the above issues are addressed, it will be important to implement a way to evaluate the uncertainties associated with maps of the seismic source provided by our method. This could be achieved, for example, via a boot-strapping technique (Efron, 1981), conducting separate time-reversal simulations with different subsets of the available station array, and measuring the discrepancy between the corresponding results: the smaller the discrepancy, the lower the uncertainty in the results. This has not been implemented in our current version of the code, which is still in ”beta phase”, but will be worked out in our future efforts.

References

Ammon, C. J., Ji, C., Thio, H.-K., Robinson, D., Ni, S., Hjorleifsdottir, V., Kanamori, H., Lay, T., Das, S., Helmberger, D. et al. (2005), ‘Rupture process of the 2004 sumatra-andaman earthquake’, *science* **308**(5725), 1133–1139.

Boschi, L., Molinari, I. and Reinwald, M. (2018), ‘A simple method for earthquake location by surface-wave time reversal’, *Geophysical Journal International* **215**(1), 1–21.

Boschi, L. and Woodhouse, J. H. (2006), ‘Surface wave ray tracing and azimuthal anisotropy: a generalized spherical harmonic approach’, *Geophysical Journal International* **164**(3), 569–578.

Cesca, S., Letort, J., Razafindrakoto, H. N., Heimann, S., Rivalta, E., Isken, M. P., Nikkhoo, M., Passarelli, L., Petersen, G. M., Cotton, F. et al. (2020), ‘Drainage of a deep magma reservoir near mayotte inferred from seismicity and deformation’, *Nature geoscience* **13**(1), 87–93.

de Rosny, J. and Fink, M. (2002), ‘Overcoming the diffraction limit in wave physics using a time-reversal mirror and a novel acoustic sink’, *Physical review letters* **89**(12), 124301.

Efron, B. (1981), ‘Nonparametric estimates of standard error: the jackknife, the bootstrap and other methods’, *Biometrika* **68**(3), 589–599.

Fink, M. (2006), ‘Time-reversal acoustics in complex environments’, *geophysics* **71**(4), SI151–SI164.

Ide, S. (2007), ‘Slip inversion’, *Earthquake seismology* **4**, 193–223.

Ishii, M., Shearer, P. M., Houston, H. and Vidale, J. E. (2005), ‘Extent, duration and speed of the 2004 sumatra–andaman earthquake imaged by the hi-net array’, *Nature* **435**(7044), 933–936.

Krüger, F. and Ohrnberger, M. (2005), 'Spatio-temporal source characteristics of the 26 december 2004 sumatra earthquake as imaged by teleseismic broadband arrays', *Geophysical research letters* **32**(24).

Lay, T., Kanamori, H., Ammon, C. J., Nettles, M., Ward, S. N., Aster, R. C., Beck, S. L., Bilek, S. L., Brudzinski, M. R., Butler, R. et al. (2005), 'The great sumatra-andaman earthquake of 26 december 2004', *science* **308**(5725), 1127–1133.

Peter, D., Boschi, L. and Woodhouse, J. (2009), 'Tomographic resolution of ray and finite-frequency methods: a membrane-wave investigation', *Geophysical Journal International* **177**(2), 624–638.

Pu, M., Feng, Q., Wang, M., Hu, C., Huang, C., Ma, X., Zhao, Z., Wang, C. and Luo, X. (2012), 'Ultrathin broadband nearly perfect absorber with symmetrical coherent illumination', *Optics express* **20**(3), 2246–2254.

Tanimoto, T. (1990), 'Modelling curved surface wave paths: membrane surface wave synthetics', *Geophysical Journal International* **102**(1), 89–100.

CHAPTER 6

APPENDIX: Conference Papers

6.1 GNGTS 2023: Convegno Nazionale del Gruppo Nazionale di Geofisica della Terra Solida

Imaging of seismic sources by surface-wave time-reversal: long-period earthquakes

Apsara Sharma Dhakal[1](apsara.sharmadhakal@phd.unipd.it),
Lapo Boschi[1,2], Simone Cesca[3]
[1] *Dipartimento di Geoscienze, Universitá degli Studi di, Padova, Italy*
[2] *Institut des Sciences de la Terre Paris, Sorbonne Université, Paris, France*
[3] *GFZ German Research Centre for Geosciences, Potsdam, Germany*

1. Abstract

The study of long-period events in volcanic settings is of fundamental importance to better understand the physics of volcanic plumbing systems. We locate long-duration, long-period events at Mayotte, Comoro Islands, using a source-imaging method recently developed and previously validated by application to large earthquakes. Our approach combines seismic time-reversal with a surface-wave ray tracing algorithm based on generalized spherical-harmonic parameterization of surface-wave phase velocity, and accounting for azimuthal anisotropy. This new application focuses on different, low-frequency signals recorded at regional to teleseismic distances, which have been attributed to the drainage and resonance of a deep magma reservoir.

We first conduct synthetic tests to quantify the resolving power of our method, given the available data coverage for the events of interest. We then use low-frequency Rayleigh-wave signals recorded by different stations, reverse them in time and back propagate them through a surface-wave phase-velocity model. The time-reversed wave field has a prominent maximum at the spatial location(s) and time(s) where and when the recorded signal had been generated. From the time- and space-distribution of such maximum, we can make inferences on the nature of the source. Our results are in good agreement with centroid locations by moment tensor inversion. We show that our methodology is applicable to volcanic settings, possibly providing new insights into the nature of long-period seismic sources related to volcanic activity. A precise location of such events helps constraining the depth, size and geometry of the seismogenic volume.

2. Introduction

Volcano seismicity produces a wide range of volcanic signals that includes volcanic tremor, long period and very long period as well as volcano tectonic or high-frequency earthquakes. LP events are short where as volcanic tremor can last to few minutes, hours or even days. Locating such events using travel time inversion is difficult due to lack of clear seismic onsets. Different methods have been introduced to relocate such events that includes relocation method (Shelly et al. 2006), Source Scanning Algorithm (SSA)(Kao et al. 2005), full-waveform inversion (Legrand et al. 2000), polarization and amplitude decay method (Gaete et al. 2019) have been implemented to relocate such events but are limited to only a part of signal i.e., the direct arrival. In this study, to locate such events, we use a different approach that is restricted to the surface wave data, which can be approximated as membrane waves and modelled via ray-tracing.

3. Study Area

Our study focuses on one of the volcanic Comoros archipelago (Mayotte Island) located in the northern part of the Mozambique channel, between Northwestern Madagascar and Northeastern Mozambique. It is home to a population of 299,348 (2022) population. This region is affected by multiple tectonic processes that includes episode of NE-SW trend rift. Volcanism at Mayotte is supposed to have started at about 10-20 Ma and subsequently migrated to produce other islands. The latest volcanic eruption documented was at about 4kyr ago.

At the present time, there is a diffuse and moderate seismicity in the archipelago and few historically felt events. A peak M_w 5.9 earthquake occured on 15 May 2018, the largest ever recorded in the region. Over a period of one year starting from 10 May 2018, around 32 (VT) earthquakes of magnitude greater than 5 was recorded.

4. Method

The method includes combination of seismic time reversal approach with the surface wave ray-tracing algorithm based on a generalized spherical-harmonic parameterization of a surface wave phase velocity, accounting for azimuthal anistotropy. It is applied to surface wave signals that are filtered within a narrow-frequency band and model its propagation via membrane wave approach which lowers the computational costs as well as eases the visualization of the propagating wave fields. The method is breifly described in Dhakal et al. (2022) which is an extension to the global sacle of that of Boschi et al. (2018) where the flat-earth ray-tracing scheme is replaced with the one of Boschi & Woodhouse (2006).

5. Workflow

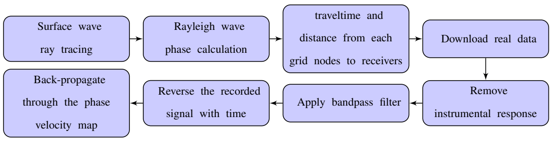
Surface wave ray tracing
Rayleigh wave phase calculation
traveltime and distance from each grid nodes to receivers
Download real data
Remove instrumental response
Apply bandpass filter
Reverse the recorded signal with time
Back-propagate through the phase velocity map

6. Results: Synthetic Test

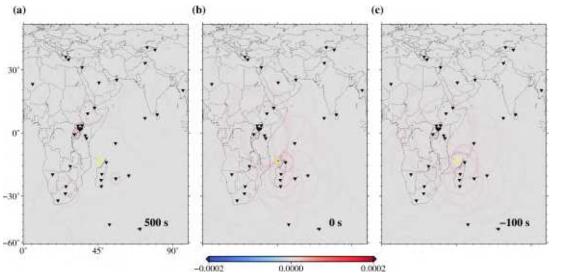

Snapshots of synthetic-data time-reversal simulation using 35 s Ricker wavelet as source time function and modelled through a Rayleigh-wave phase-velocity map and backpropagated in the same model. Negative time show non-physical sihnal that continues to propagate after focusing. The time t=0 s corresponds to the origin time.

7. Results: Synthetic Test

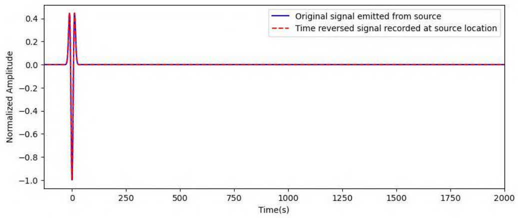

Normalized time-reversed back propagated displacement (red dashed curve) obtained at the source location. This signal overlaps very well with the originally emitted signal.

8. Results: Real Data (VLP event)

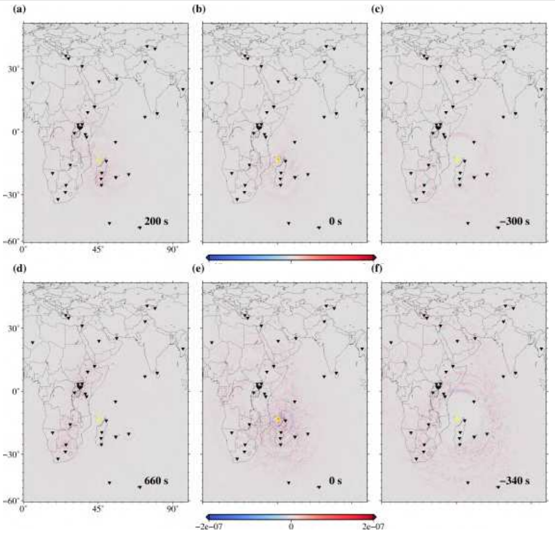

Snapshots of surface wave ray-tracing time reversal simulation using real data (VLP event, 11 November 2018, Mw 5.1), in the 20-to-40 s period band (a-c) and 20-to-60 s period band (d-f) using recordings from 44 stations. Here time t = 0 s is VLPs initiation time (catalog reported by Cesca et al. (2019)). The results are measured in meters.

9. Results: Real Data (VLP event)

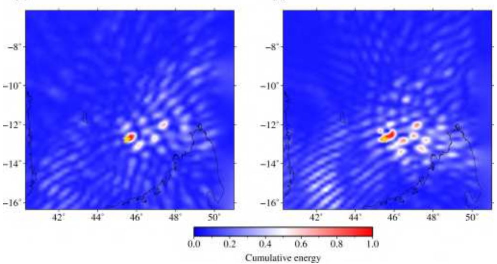

Integrated energy over 20 s after the initiation of VLP event obtained using time-reversing traces for (a) 20-to-40 s and (b) 20-to-60 s band-pass respectively for the same VLP event.

10. Conclusions

We implemented the concept of surface wave ray tracing and time reversal method to five seismic VLP signals provided with a good velocity model. Tracing the spatial time-reversed wave field, we reconstructed the focusing area where maximum amplitude correspond to the right time and location of 11 November, 2018 VLP event. Similarly, we were able to locate four more such events that occured in 15 June, 16 July, 31 July and 21 September 2018. Our results are in good agreement with the centroid location obtained by using moment tensor inversion.Further using the time-reversed displacement value, we traced the distribution of energy for such events with time and found to be unidirectional propagating northeast.

11. References

- Boschi, L., Molinari, I. & Reinwald, M. (2018) A simple method for earthquake location by surface-wave time reversal. *Geophys J Int*, 215, 1-21.
- Boschi, L. & Woodhouse, J.H. (2006) Surface wave ray tracing and azimuthal anisotropy: a generalized spherical harmonic approach. *Geophys J Int*, 164, 569-578.
- Cesca, S., Letort, J., Razafindrakoto, H.N.T., Heimann, S., Rivalta, E., Isken, M.P., Nikkhoo, M., et al. (2020) Drainage of a deep magma reservoir near Mayotte inferred from seismicity and deformation. *Nat Geosci*, 13, 87-93.
- Dhakal, A.S., Molinari, I. & Boschi, L. (2022) Seismic source mapping by surface wave time reversal: application to the great 2004 Sumatra earthquake. *Geophys J Int.*, 233, 1018-1035.
- Gaete, A., Cesca, S., Franco, L., San Martin, J., Cartes, C., & Walter, T. R. (2019). Seismic activity during the 2013-2015 intereruptive phase at Lascar volcano, Chile. *Geophysical Journal International*, 219(1), 449-463.
- Legrand, D., Kaneshima, S. & Kawakatsu, H. (2000) Moment tensor analysis of near-field broadband waveforms observed at Aso Volcano, Japan. *Journal of Volcanology and Geothermal Research*, 101, 155-169.

6.2 EGU 2023: European Geosciences Union

EGU23-5787, updated on 22 Feb 2023
https://doi.org/10.5194/egusphere-egu23-5787
EGU General Assembly 2023

Imaging of seismic sources by surface-wave time-reversal: long-period earthquakes

Apsara Sharma Dhakal[1], Lapo Boschi[2], and Simone Cesca[3]
[1]Dipartimento di Geoscienze, Università degli Studi di, 35131 Padova, Italy (apsara.sharmadhakal@studenti.unipd.it)
[2]Dipartimento di Geoscienze, Università degli Studi di, 35131 Padova, Italy (lapo.boschi@unipd.it)
[3]GFZ German Research Centre for Geosciences, Potsdam, Germany(cesca@gfz-potsdam.de)

The study of long-period events in a volcanic setting is of fundamental importance to better understand the physics of volcanic plumbing systems. We locate such events using a source-imaging method developed by our team, and successfully applied, e.g., to the great Sumatra earthquake (Dhakal et al. 2022). Our approach combines seismic time reversal with a surface-wave ray tracing algorithm based on generalized spherical-harmonic parameterization of surface-wave phase velocity, and accounting for azimuthal anisotropy. We present a new application, to recordings of a suite of Mayotte events that Cesca et al. (2020) have already studied and interpreted in terms of the drainage of a magma reservoir.

We first conduct synthetic tests to quantify the resolving power of our method, given the available data coverage for the events of interest. We then use low-frequency Rayleigh wave signals recorded by different stations, reverse them in time and back propagate them through a surface-wave phase-velocity model. The time-reversed wave field has a prominent maximum at the spatial location(s) and time(s) where and when the recorded signal had been generated. From the time- and space-distribution of such maximum, we can make inferences on the nature of the source. Results so obtained are compared with those determined by Cesca et al. (2020) via moment tensor inversion and found to be in good agreement. We infer that our methodology is applicable to volcanic settings, possibly providing new insights into the nature of long-period seismic sources related to volcanic activity. The precise location of such events can provide better constraints on the depth interpretations and the extent of the seismic source.

How to cite: Sharma Dhakal, A., Boschi, L., and Cesca, S.: Imaging of seismic sources by surface-wave time-reversal: long-period earthquakes, EGU General Assembly 2023, Vienna, Austria, 24–28 Apr 2023, EGU23-5787, https://doi.org/10.5194/egusphere-egu23-5787, 2023.